

UNIVERSITÀ
DI PAVIA

Dipartimento di Fisica

Corso di Laurea Magistrale in Scienze Fisiche

Study of the Impact of Short Circuits on CMS Triple-GEM Detector Performance

Studio dell'impatto dei cortocircuiti sulle prestazioni dei rivelatori a tripla-GEM di CMS

Tesi per la Laurea di:

Andrea Civardi

Supervisori:

Prof. Ilaria Vai

Prof. Paolo Vitulo

Correlatore:

Dott. Simone Calzaferri

A.A. 2025-2026

Abstract

Electrical discharges in triple-Gas Electron Multiplier (GEM) detectors can lead to permanent short circuits, altering the high-voltage distribution and potentially compromising detector performance. This issue also affects the GEM detectors installed in the muon system of the Compact Muon Solenoid (CMS) experiment at the Large Hadron Collider (LHC). This thesis investigates the impact of such defects on detection efficiency through laboratory measurements performed with a small-scale triple-GEM detector, in which the electrical effects of short circuits are reproduced by controlled variations of the applied voltages. The effects of voltage variations across individual GEM foils and gas gaps, as well as configurations involving multiple affected foils, are systematically characterized, revealing a different sensitivity of the detector efficiency to the voltage applied across each foil. These results provide an experimental basis for understanding the consequences of short circuits on triple-GEM detector performance and their implications for the operation of GEM detectors in CMS.

Sommario

Le scariche elettriche nei rivelatori a tripla Gas Electron Multiplier (GEM) possono portare a cortocircuiti permanenti, alterando la distribuzione dell'alta tensione e compromettendo potenzialmente le prestazioni dei rivelatori. Questo problema interessa anche i rivelatori GEM installati nel sistema a muoni dell'esperimento Compact Muon Solenoid (CMS) al Large Hadron Collider (LHC). Questa tesi studia l'impatto di tali difetti sull'efficienza di rivelazione tramite misure di laboratorio effettuate con un rivelatore a tripla-GEM di piccole dimensioni, in cui gli effetti elettrici dei cortocircuiti sono riprodotti mediante variazioni controllate delle tensioni applicate. Gli effetti delle variazioni di tensione sui singoli fogli GEM e sulle gas gap, così come le configurazioni con più fogli coinvolti, sono caratterizzati in modo sistematico, evidenziando una diversa sensibilità dell'efficienza del rivelatore alla tensione applicata a ciascun foglio GEM. Questi risultati forniscono una base sperimentale per comprendere le conseguenze dei cortocircuiti sulle prestazioni dei rivelatori a tripla-GEM e le loro implicazioni per il funzionamento dei rivelatori GEM in CMS.

Contents

Abstract **iii**

Sommario **v**

Introduction **1**

1 CMS GEM detectors and the short circuits problem **3**
1.1 CERN and LHC . . . 3
1.1.1 High Luminosity LHC . . . 4
1.2 Compact Muon Solenoid . . . 6
1.2.1 The CMS muon system . . . 8
Muon momentum measurement and trigger principles . . . 10
1.3 Gas Electron Multiplier technology . . . 11
1.3.1 Operating principle . . . 12
1.3.2 Triple-GEM detector . . . 16
1.3.3 Performance and characteristics . . . 17
Effective gain . . . 17
Spatial and time resolution . . . 18
1.4 GEM detectors in CMS . . . 19
1.4.1 GE1/1 . . . 20
1.4.2 Discharges and short circuits in GE1/1 . . . 21
Discharges . . . 22
High-voltage system . . . 23
Short circuit formation . . . 24
Electrical consequences of a short circuit . . . 25
Operational experience during Run 3 . . . 27

2 Experimental setup and detector characterization **31**
2.1 10×10 triple-GEM . . . 31

2.2 Gas supply . . . 33
2.3 High Voltage supply . . . 34
2.3.1 HV supply system . . . 34
2.3.2 HV supply management . . . 36
GEM voltage configuration and equivalent current . . . 37
GECO software . . . 37
HV setting automation . . . 39
2.4 Data acquisition chain . . . 41
2.4.1 DAQ automation . . . 41
2.4.2 Remote monitoring via Grafana . . . 43
2.5 GEM characterization . . . 44
2.5.1 Gain measurement . . . 45
Experimental setup . . . 46
Rate measurement . . . 46
Current measurement . . . 52
Gain curves . . . 55
Gain with the multichannel analyzer . . . 57
GEM sensitivity . . . 59
2.5.2 Gain uniformity . . . 63
2.5.3 Efficiency . . . 65

3 Study of short circuits in triple-GEM detectors 73
3.1 Why detection efficiency: a key performance parameter . . . 73
3.2 HV correction for pressure and temperature . . . 74
3.3 Mocking of short circuits . . . 78
3.4 Voltage reductions across a single foil . . . 84
3.4.1 G1Top . . . 85
Large voltage reductions . . . 87
3.4.2 G2Top and G3Top . . . 91
3.4.3 Foil comparison . . . 93
3.5 Voltage increase across gas gaps . . . 96
3.6 Double voltage reductions across foils . . . 101
3.6.1 Comparison of voltage reductions . . . 107
3.7 HV compensation . . . 110
3.8 From the laboratory study to GE1/1 operation . . . 114

Conclusions and outlook **117**

A Alternative representations of the efficiency curves **121**

A.1 Efficiency as a function of equivalent current 121

A.2 Efficiency as a function of top-channel voltage sum 122

Bibliography **127**

Introduction

The High-Luminosity upgrade of the Large Hadron Collider (HL-LHC) will impose increasingly demanding operating conditions on the detectors of the Compact Muon Solenoid (CMS) experiment. In this context, Gas Electron Multiplier (GEM) detectors, already installed and operating in the CMS muon system, play an important role in ensuring high detection efficiency and precise spatial and time measurements in regions characterized by high particle fluxes.

However, the operation of GEM detectors presents several challenges, including the occurrence of electrical discharges that can lead to the formation of permanent short circuits between the two electrodes of a GEM foil. Such defects modify the effective voltage distribution within the detector, potentially affecting its performance and reducing its detection efficiency. This issue has been observed in the first GEM station installed in CMS, known as GE1/1, and represents an important challenge for its long-term operation.

The aim of this thesis is to investigate the impact of short circuits on the performance of triple-GEM detectors, with particular emphasis on detection efficiency. For this purpose, an experimental study was carried out using a small-scale triple-GEM detector operated in the laboratory. By reproducing the voltage variations associated with short circuits under controlled conditions, the effects of different fault configurations were systematically investigated. The results of this study contribute to a better understanding of the impact of short circuits on GEM detector performance and provide useful information for the evaluation of high-voltage compensation strategies in the CMS GE1/1 system.

The thesis is organized into three chapters, whose contents are outlined below.

Chapter 1 introduces the scientific and technological background of the study. After presenting the LHC accelerator at CERN, including the operating conditions expected after the High-Luminosity upgrade, the chapter describes the CMS experiment and its muon detection system. The operating principle of GEM detectors is then presented, with particular emphasis on the triple-GEM configuration and its main performance characteristics. The discussion subsequently focuses on the

integration of GEM detectors into the CMS muon system, especially the GE1/1 chambers. Finally, the chapter examines the formation of permanent short circuits following electrical discharges, explaining their effects on the high-voltage distribution and the resulting changes in the electric fields within the detector. The electrical consequences of these defects and the operational experience gained during Run 3, the third data-taking period of the LHC (2022–2026), are discussed to establish the motivation for the experimental investigation.

Chapter 2 describes the experimental setup developed for the laboratory study and the characterization of the detector used in the measurements. The main components of the apparatus are presented, including the $10\times10\,\mathrm{cm}^2$ triple-GEM detector, the gas supply system, the high-voltage supply and distribution system, and the data acquisition chain. Particular attention is devoted to the automation of voltage settings and data acquisition, as well as to the remote monitoring of the detector operating conditions. The chapter then presents the characterization measurements performed under nominal operating conditions, covering the effective gain, its spatial uniformity, and the detection efficiency. These measurements provide a reference for the detector response in the absence of mocked faults and establish the baseline conditions required for the subsequent study.

Chapter 3 presents the experimental investigation of the effects of short circuits on triple-GEM detector performance, using detection efficiency as the main observable. After discussing the correction for pressure and temperature variations and the procedure adopted to reproduce short-circuit effects through controlled modifications of the applied voltages, the chapter examines the response of the detector to voltage reductions across individual GEM foils. The effects on the three foils are compared, and the study is extended to configurations involving simultaneous voltage reductions across two foils. The corresponding voltage increases across the gas gaps are also investigated to assess their contribution to the observed efficiency variations. Finally, the HV compensation procedure adopted for the GE1/1 chambers is described and related to the individual voltage effects characterized in the laboratory. The comparison of these results with the data collected on GE1/1 chambers operating in CMS, both healthy and affected by short circuits, is presented as a natural extension of this work.

Chapter 1

CMS GEM detectors and the short circuits problem

This chapter introduces the physical and technological background necessary to understand the objectives of this thesis. After presenting the CERN accelerator complex, the Large Hadron Collider (LHC), and the High-Luminosity LHC (HL-LHC) upgrade, the Compact Muon Solenoid (CMS) experiment and its muon detection system are described, highlighting the challenges posed by the HL-LHC operating conditions. The chapter then introduces the Gas Electron Multiplier (GEM) technology and discusses its adoption in the CMS forward muon system. Particular attention is devoted to the GE1/1 detector system, focusing on the occurrence of electrical discharges and the formation of permanent short circuits in GEM foils, which represent one of the main operational issues affecting these detectors. These phenomena provide the motivation for the experimental work presented in the following chapters.

1.1 CERN and LHC

The European Organization for Nuclear Research (Conseil Européen pour la Recherche Nucléaire, CERN) was founded in 1954. Located on the Franco-Swiss border near Geneva, it is today the world's largest laboratory for particle physics [1]. Over the decades, CERN's accelerator complex has steadily grown in size, energy, and scientific capabilities allowing for fundamental discoveries in particle physics. Among CERN's most significant scientific achievements are the discovery of weak neutral currents in 1973 [2, 3], the observation of the W and Z bosons in 1983 [4, 5, 6, 7], and the discovery of the Higgs boson in 2012 [8, 9].

CERN's largest and most powerful accelerator is the Large Hadron Collider (LHC). The LHC, inaugurated in 2008, is located in a 27-kilometre tunnel 100 m underground and consists of a circular ring equipped with superconducting magnets and radio-frequency accelerating cavities. Inside the accelerator, two proton[1] beams circulate in opposite directions in two separate beam pipes and collide at a centre-of-mass energy of up to 13.6 TeV. The collisions take place at four interaction points, where four large experiments record the particles produced in the interactions. The four experiments are A Toroidal LHC ApparatuS (ATLAS), Compact Muon Solenoid (CMS), A Large Ion Collider Experiment (ALICE) and Large Hadron Collider beauty (LHCb). Each detector consists of several sub-detectors designed to reconstruct particle trajectories, identify particles, and measure physical quantities such as their momentum and energy.
The discovery of the Higgs boson at the LHC completed the experimental confirmation of the Standard Model (SM) by revealing its last predicted fundamental particle. In the coming years, the LHC will continue to play a central role in particle physics through increasingly precise measurements of the Higgs boson's properties. Nevertheless, the SM cannot account for several observed phenomena, including the nature of dark matter and the matter-antimatter asymmetry of the Universe. The High-Luminosity LHC [10] (HL-LHC) (Section 1.1.1) will significantly extend the physics reach of the LHC, enabling precision measurements of the Higgs boson while increasing the sensitivity to physics beyond the Standard Model (BSM), including supersymmetric (SUSY) particles, high-mass resonances, and dark matter candidates [11].

1.1.1 High Luminosity LHC

The HL-LHC project is the upgrade programme of the LHC aimed at extending its physics reach beyond the original design performance. The objective is to maximise the performance of the LHC by increasing its integrated luminosity[2] by a factor of 10 compared to its original design value, in order to collect a larger data sample and thereby improve the statistical precision of physics measurements. This goal

[1] In addition to protons, the LHC can also accelerate heavy ions such as lead, argon, and xenon nuclei.

[2] The integrated luminosity is obtained by integrating the instantaneous luminosity over time. The instantaneous luminosity is related to the interaction rate R through $R = L\sigma$, where σ is the process cross section.

can be achieved by increasing the instantaneous luminosity, resulting in a larger number of collisions per bunch crossing.
The instantaneous luminosity is determined by the accelerator and beam parameters. Consequently, the LHC will undergo a major upgrade involving new superconducting magnets, improved beam collimation systems and radiofrequency crab cavities.
As shown in Fig. 1.1, the LHC has delivered more than $500\,\mathrm{fb}^{-1}$ of total integrated luminosity over Runs 1–3 [12], with approximately $350\,\mathrm{fb}^{-1}$ delivered during Run 3 alone [13]. The HL-LHC aims to increase the total integrated luminosity to about $3000\,\mathrm{fb}^{-1}$ over approximately 12 years of operation. This will be achieved by increasing the peak instantaneous luminosity from the original LHC design value of $1 \times 10^{34}\,\mathrm{cm}^{-2}\mathrm{s}^{-1}$ to a value of $5 \times 10^{34}\,\mathrm{cm}^{-2}\mathrm{s}^{-1}$, with the possibility of reaching up to $7.5 \times 10^{34}\,\mathrm{cm}^{-2}\mathrm{s}^{-1}$ [14, 15].

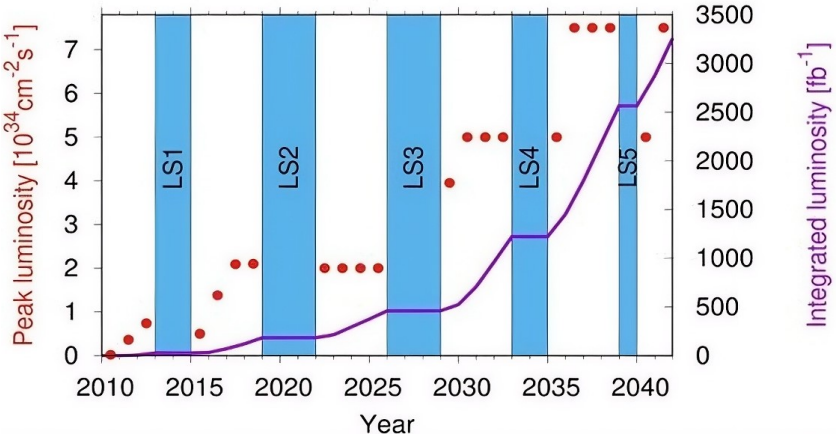


FIGURE 1.1: Evolution of the LHC instantaneous and integrated luminosity throughout the LHC and HL-LHC programme [16].

The increase in instantaneous luminosity will result in higher particle fluxes, larger detector occupancies, increased radiation levels and significantly larger pile-up, i.e. a larger number of simultaneous proton-proton interactions occurring within the same bunch crossing. These effects pose unprecedented challenges for detector operation and event reconstruction. Consequently, all LHC experiments require substantial detector upgrades to maintain their performance under the HL-LHC operating conditions [17].

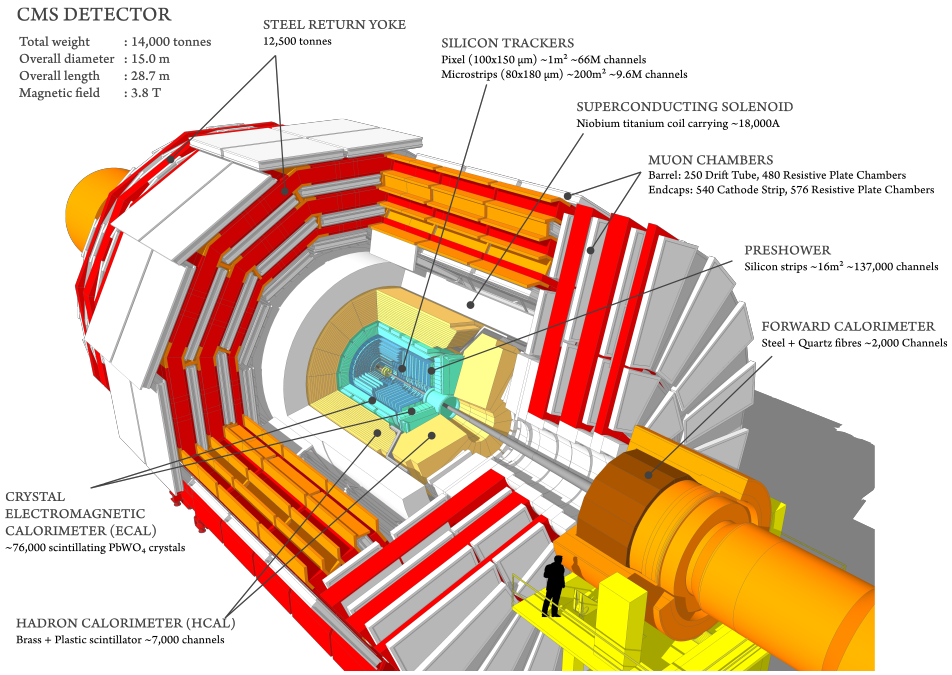


FIGURE 1.2: Schematic cutaway view of the CMS detector highlighting its cylindrical geometry and the main subdetector components [18].

1.2 Compact Muon Solenoid

Among the four major LHC experiments, the Compact Muon Solenoid (CMS) is a general-purpose detector designed to investigate a wide range of physics processes arising from proton-proton collisions.

As Fig. 1.2 shows, CMS has a cylindrical shape with a length of 21.6 m, a diameter of 14.6 m and a weight of about 12500 tonnes. The detector is built around the LHC beam pipe, which defines its cylindrical axis. Its subdetectors are arranged in concentric layers surrounding the interaction point, giving CMS its characteristic onion-like structure.

The CMS coordinate system, shown in Fig. 1.3, has its origin at the nominal interaction point. The y-axis points vertically upward, the x-axis points toward the center of the LHC ring, and the z-axis is aligned with the anticlockwise beam direction. The azimuthal angle ϕ is defined in the x-y plane and measured from the x-axis, while the polar angle θ is defined with respect to the z-axis.

Instead of the polar angle θ, it is customary to use the pseudorapidity η, defined as

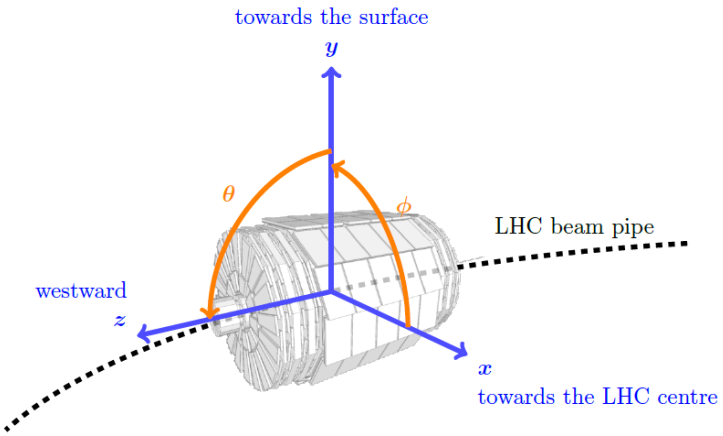


FIGURE 1.3: CMS reference frame [19].

$$\eta = -\ln\left[\tan\left(\frac{\theta}{2}\right)\right], \tag{1.1}$$

because it is approximately invariant under Lorentz boosts along the beam (z) axis. CMS is divided into two main regions: the barrel, which forms the central cylindrical part of the detector, and the two endcaps, which close the cylinder at its extremities. At the heart of the barrel region lies the 13-m-long, 5.9 m inner diameter, 3.8 T superconducting solenoid. This strong magnetic field is essential to achieve high transverse momentum resolution within the compact detector geometry [20].
Starting from the beam pipe and moving radially outwards, the CMS subdetectors are:

- **Tracker.** The tracking volume consists of a 5.8 m-long, 2.6 m-diameter cylindrical region. The tracker is composed of three inner layers of silicon pixel detectors, providing precise measurements of charged particle trajectories and secondary vertex positions, followed by ten outer layers of silicon microstrip detectors, which ensure high spatial resolution in the high track multiplicity environment.

- **Electromagnetic calorimeter (ECAL).** The ECAL is a homogeneous calorimeter made of lead tungstate ($PbWO_4$) crystals, with coverage up to $|\eta| < 3.0$. It measures the energy of electrons and photons through the development of electromagnetic showers.

- **Hadronic calorimeter (HCAL).** The HCAL surrounds the ECAL and is designed to measure the energy of hadrons, contributing to jet reconstruction and missing transverse energy measurements. It consists of a central brass/scintillator sampling calorimeter covering the barrel and endcap regions up to $|\eta|< 3.0$, complemented by an additional outer layer (HO) in the barrel region to improve hadronic shower containment. The coverage is extended up to $|\eta|< 5.0$ by forward calorimeters based on iron/quartz-fibre technology, which are suitable for the high radiation environment in the forward region [21].

- **Muon system.** The outermost subsystem is the muon system, which is described in detail in the following section (Section 1.2.1). Owing to the high penetration capability of muons, their detection requires dedicated gaseous detectors installed outside the calorimeters.

1.2.1 The CMS muon system

Muon identification is one of the key features of the CMS experiment, as many SM and BSM processes produce muons in the final state. Owing to their relatively low interaction probability with matter, muons can traverse the calorimeters and reach the outermost part of the detector, providing clean experimental signatures even in the high-background environment of the LHC. A notable example is the Higgs boson decay channel $H \to ZZ^{(*)} \to 4\ell$, for which the four-muon final state represents the cleanest experimental signature and is therefore commonly referred to as the *golden channel*. The ability to efficiently identify muons over a wide pseudorapidity range, accurately measure their momentum, and provide a reliable trigger is therefore essential for fully exploiting such physics channels.
The CMS muon system was therefore designed to fulfill three primary tasks: muon identification, momentum measurement, and trigger generation. Its performance relies on the combination of the 3.8 T superconducting solenoid and the large steel return yoke, which provides both the magnetic field necessary for momentum measurement and the mechanical support for the muon detectors.
The cylindrical geometry of the solenoid naturally divides the muon system into a central barrel section and two endcap regions. As shown in Fig. 1.4, the different detector operating conditions across the pseudorapidity range require the use of

three complementary detector technologies, each optimized for the local particle flux, magnetic field configuration, and background conditions.

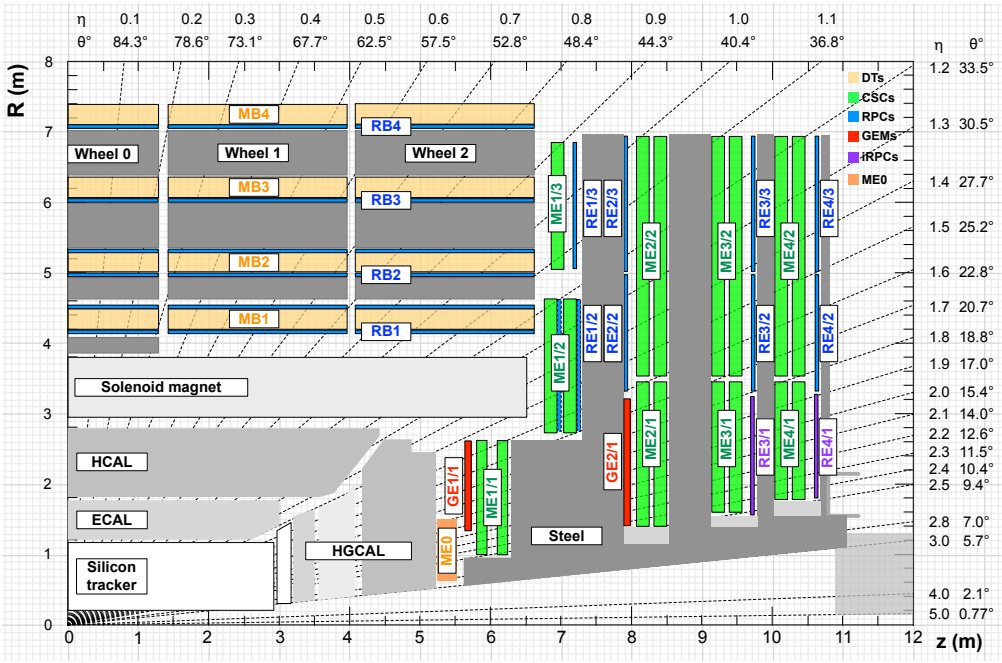


FIGURE 1.4: Quarter-section view of the CMS muon system, illustrating the detector layout and the pseudorapidity coverage of the different detector technologies [17].

In the barrel region ($|\eta| < 1.2$), where the muon rate is relatively low, the radiation background is moderate, and the magnetic field is nearly uniform, Drift Tubes (DTs) are well suited for muon detection. The DT chambers are arranged in four stations embedded within the layers of the steel return yoke. Their geometry and orientation provide high tracking efficiency, allowing hits from different stations to be combined into precise muon tracks while effectively suppressing spurious background signals.

In the endcap regions ($0.9 < |\eta| < 2.4$) the higher particle rates, higher radiation levels, and more complex magnetic field require a different technology. Here, Cathode Strip Chambers (CSCs) are employed because of their excellent time resolution, fine spatial segmentation, and radiation tolerance. Similarly to the DT system in the barrel, four CSC stations are installed in each endcap between successive layers of the return yoke, providing robust pattern recognition and accurate matching with tracks reconstructed in the silicon tracker.

Complementing both DTs and CSCs, Resistive Plate Chambers (RPCs) provide a dedicated triggering system in the pseudorapidity range $|\eta|< 2.1$. Their excellent time resolution enables an unambiguous identification of the bunch crossing associated with each muon candidate, while their independent trigger information improves the overall trigger efficiency and helps resolve ambiguities in track reconstruction. Although their spatial resolution is coarser than that of DTs and CSCs, RPCs play a crucial role in the Level-1 (L1) muon trigger and enhance the overall robustness of the CMS muon system [21, 22].

Muon momentum measurement and trigger principles

The momentum of charged particles is determined by exploiting the curvature of their trajectories in the magnetic field generated by the CMS superconducting solenoid. In the transverse plane, the radius of curvature R is related to the transverse momentum p_T through

$$p_T = 0.3\,BR, \tag{1.2}$$

where B is the magnetic field strength expressed in Tesla, R is the radius of curvature in meters, and p_T is measured in GeV/c. Consequently, particles with higher transverse momentum experience a smaller deflection in the magnetic field, making the determination of their momentum increasingly challenging, since even small uncertainties in the reconstructed trajectory translate into larger uncertainties on the momentum estimate [21].

Muon trajectories are reconstructed from the signals produced as they traverse the gaseous detectors of the muon system. Charged particles ionize the detector gas, generating electrical signals that are read out by the detector electronics. These signals are converted into spatial measurements, commonly referred to as *hits*, whose positions are reconstructed using algorithms specific to each detector technology [23].

The transverse momentum is determined by fitting the trajectory passing through the reconstructed hits. The precision of this measurement depends on several factors, including the intrinsic spatial resolution of the detectors, the number of hits, and the length of the trajectory over which the curvature is measured, which is the so-called *lever arm*. A larger number of precise measurements distributed over

a longer lever arm allows the track curvature to be determined more accurately, resulting in an improved momentum resolution.
Although the same reconstruction principles apply throughout the detector, the momentum measurement performance is not uniform over the full pseudorapidity range. In the barrel region, the nearly uniform magnetic field allows an accurate determination of the track curvature. In contrast, the endcap regions are characterized by a more complex magnetic field configuration and by a larger amount of material traversed before the first muon station, resulting in increased multiple scattering and a degradation of the momentum resolution [22]. The reduction of the magnetic field at large pseudorapidities further limits the bending of high-momentum muons, making an accurate momentum measurement increasingly challenging [24].
The accuracy of the transverse momentum measurement plays a crucial role not only for offline reconstruction, but also for the real-time event selection performed by the L1 trigger. At this stage, muon candidates are identified by applying transverse momentum thresholds to the momentum estimated from the muon system. The accuracy of this estimate is therefore essential for controlling the trigger rate. A degraded momentum resolution increases the probability that low-p_T muons are reconstructed with an overestimated transverse momentum, causing them to exceed the trigger threshold and leading to an increase in the trigger rate. This effect is particularly relevant in the forward region, where the magnetic field is weaker and the background rates are higher [24].
At the HL-LHC, where the particle flux and background rates are expected to increase substantially, controlling the L1 trigger rate becomes increasingly challenging. In particular, the endcap region, which already suffers from more complex detector conditions, is expected to contribute significantly to the overall trigger rate.
For this reason, additional detector layers in the forward region are required to improve the measurement of the muon bending angle and maintain an acceptable L1 trigger rate at the HL-LHC.

1.3 Gas Electron Multiplier technology

The introduction of the multiwire proportional chamber (MWPC) [25] by Charpak in 1968 marked a major breakthrough in gaseous detector technology, providing fast detection and precise localization of ionization signals through avalanche

multiplication around thin anode wires. For several decades, MWPCs represented the standard solution for particle tracking in high-energy physics experiments. However, the increasingly demanding operating conditions of modern experiments exposed some intrinsic limitations of wire-based detectors, particularly in terms of rate capability and achievable spatial granularity. The slow evacuation of positive ions from the amplification region leads to space-charge accumulation at high particle fluxes, degrading detector performance.

The development of photolithographic manufacturing techniques enabled a new approach to gaseous detector design by replacing macroscopic wire structures with finely patterned metallic electrodes on insulating substrates. This concept was first demonstrated with the Microstrip Gas Chamber (MSGC) [26], in which the reduced electrode spacing significantly improves granularity and multi-hit capability, while the short drift path of positive ions strongly mitigates space-charge effects. Although the MSGC itself exhibited limitations in long-term operation under harsh radiation environments, it established the technological foundations for a new family of detectors known as Micro-Pattern Gaseous Detectors (MPGDs) [27].

MPGDs share several key characteristics, including high rate capability, excellent spatial resolution, fast signal formation, and good radiation tolerance, making them particularly well suited for the demanding environments of modern collider experiments. Among the various MPGD technologies developed over the past decades, the Gas Electron Multiplier (GEM) [28] has emerged as one of the most successful and versatile solutions, combining high gain with reliable operation and excellent performance over large active areas. For these reasons, GEM detectors have been adopted in several particle physics experiments, including the upgrade of the CMS muon system.

1.3.1 Operating principle

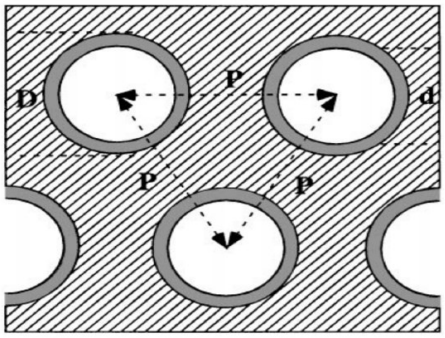
Like all gaseous detectors, GEMs rely on the ionization of the filling gas to detect charged particles traversing the sensitive volume[3]. As charged particles pass through the gas, they lose energy through inelastic collisions with gas atoms or

[3]Neutral particles, such as photons, can also be detected indirectly through their interactions with the detector material, which produce secondary charged particles. In their standard configuration, however, GEM detectors have a low sensitivity to neutral radiation and are therefore generally unsuitable for applications requiring efficient photon detection.

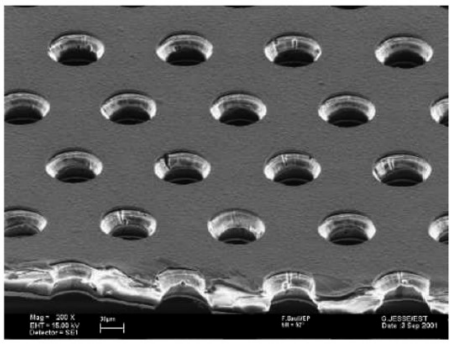
molecules. Whenever the transferred energy exceeds the ionization potential of the gas, electron–ion pairs are produced along the particle trajectory.
If a sufficiently strong electric field is applied, the liberated electrons drift towards the anode while gaining kinetic energy. When the electric field is high enough, electrons acquire sufficient energy between successive collisions to ionize additional gas molecules, initiating a Townsend avalanche. This multiplication process results in a large increase in the number of free electrons and forms the basis of gas amplification. The amplification factor, defined as the ratio between the final (N) and the initial (N_0) number of electrons,

$$G = \frac{N}{N_0} \tag{1.3}$$

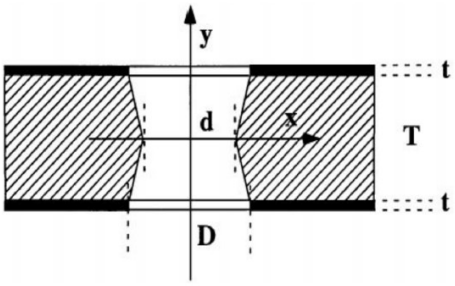
is referred to as the *gas gain* [29].
The challenge is therefore to create a localized region where such high electric fields can be achieved in a controlled and stable way. This is precisely the role of the GEM foil.
A GEM foil consists of a 50 µm thick polyimide layer, denoted by T in Fig. 1.5c, coated on both sides with 5 µm thick copper layers (t). Its geometry is illustrated in Fig. 1.5. The holes are arranged in a regular pattern with a pitch P of approximately 140 µm (Figs. 1.5a and 1.5b). The cross-sectional geometry, shown in Figs. 1.5c and 1.5d, is characterized by the polyimide thickness T, the copper thickness t, an outer hole diameter of D=70 µm at the copper surfaces, and an inner diameter of d=50 µm at the centre of the foil.
The electric field configuration inside and around a GEM foil is shown in Fig. 1.6. The double-conical geometry of the holes produces a strong concentration of the electric field, reaching values of the order of 50–100 kV/cm in the narrowest region of the hole, where the electron avalanche develops.
The GEM operation relies on three different electric field regions: the drift region above the foil, where primary electrons are guided towards the holes; the amplification region inside the holes, where electron multiplication occurs; and the transfer region below the foil, which extracts the avalanche electrons towards the readout electrode. The drift and induction fields are typically of the order of a few kV/cm and are optimized for efficient charge transport into and out of the GEM holes, respectively. Moreover, the shape of the electric field lines favours the collection of positive ions on the upper copper electrode, reducing the



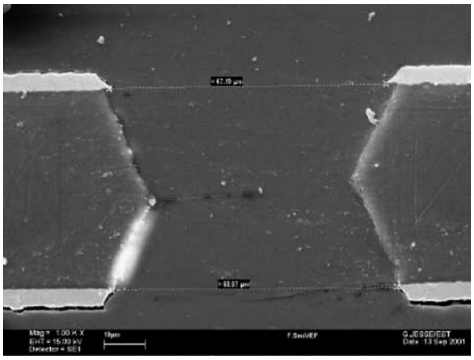
(a) Schematic view of the hole pattern, showing the hole pitch P.



(b) Scanning electron microscope (SEM) image of the GEM hole pattern.



(c) Cross-sectional view of a GEM hole, defining the outer and inner hole diameters (D and d)



(d) SEM image of the hole cross section.

FIGURE 1.5: Geometry of a standard GEM foil [28].

ion backflow towards the drift region and improving the detector performance in high-background environments.

A complete single-GEM detector (Fig. 1.7) consists of a drift electrode (cathode), a GEM foil, and a readout electrode (anode), separated by gas gaps where appropriate electric fields are applied. The electric fields required for charge transport and amplification are obtained by applying suitable voltage differences between the electrodes. In particular, the voltage difference across the GEM foil, ΔV_{GEM}, generates the intense electric field inside the holes, where electron avalanche multiplication occurs. The primary electrons produced in the drift region are guided towards the GEM holes, amplified through the avalanche process, and subsequently extracted towards the readout electrode by the induction field. The motion of the avalanche electrons towards the readout electrode induces an electrical signal, which is then processed by the detector electronics.

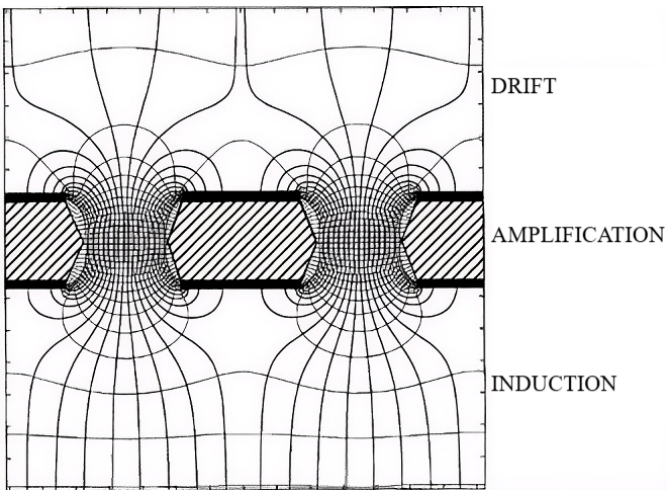


FIGURE 1.6: Electric field configuration in a GEM foil. The electric field lines and equipotential curves are shown around a GEM hole, highlighting the three operating regions: drift, amplification, and induction [30].

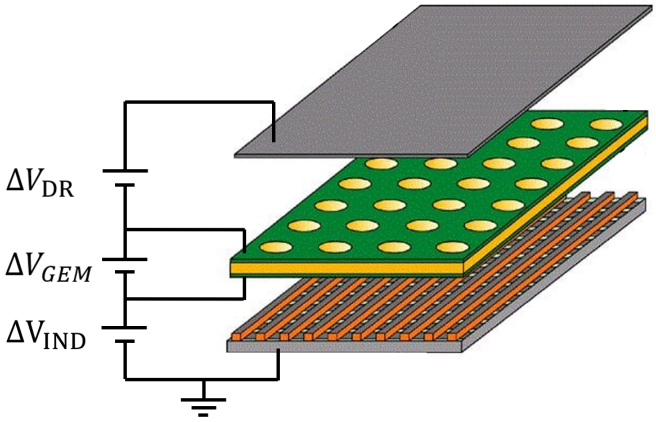


FIGURE 1.7: Schematic representation of a single-GEM detector. The cathode, GEM foil, and readout electrode are shown together with the voltage configuration used to establish the drift, amplification, and induction fields [31].

1.3.2 Triple-GEM detector

Although a single GEM foil is capable of providing substantial electron multiplication, operating at high gain increases the probability of electrical discharges and limits detector stability. These limitations are overcome by cascading multiple GEM foils, with the triple-GEM configuration being the most widely adopted in high-rate particle physics experiments [32].
As shown in Fig. 1.8, a triple-GEM detector consists of three GEM foils, labelled GEM1, GEM2, and GEM3 in order from the drift side to the readout side, arranged in cascade and separated by two transfer gaps, with a drift region above GEM1 and an induction gap between GEM3 and the readout electrode. Triple-GEM detectors can employ different gap configurations depending on the application. A commonly used configuration consists of 3/2/2/2 mm gaps for the drift, first transfer, second transfer, and induction regions, respectively. Each foil contributes only a fraction of the total gain, while the intermediate transfer fields efficiently transport the avalanche electrons from one amplification stage to the next [28].

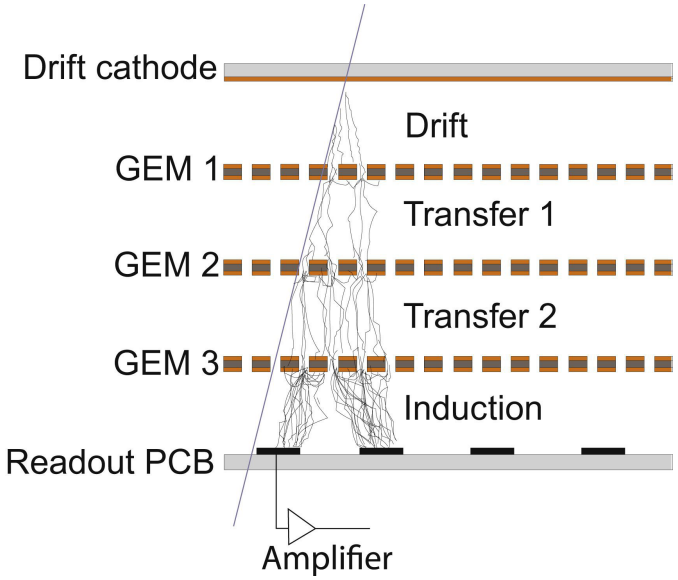


FIGURE 1.8: Schematic representation of a triple-GEM detector [17].

A triple-GEM detector comprises eight electrodes: the drift cathode, the two copper electrodes of each GEM foil, and the readout anode. To establish the electric fields required for electron multiplication inside the holes and efficient charge transport across the gas gaps, appropriate voltage differences must be applied between these electrodes. This can be achieved either by using a resistive voltage divider or by

independently controlling the voltage of each electrode. The former solution is simpler and widely adopted in large detector systems, whereas the latter provides greater flexibility in optimizing the operating conditions.
Triple-GEM detectors are typically operated with a continuous flow of gas under near-atmospheric pressure conditions. In large particle physics experiments, the most commonly adopted mixture is Ar/CO_2 (70:30), which provides a good compromise between detector stability, safe operation, and performance [28]. Alternative gas mixtures may be adopted when specific detector characteristics, such as time resolution or achievable gain, need to be optimized.

1.3.3 Performance and characteristics

The multi-stage amplification scheme of triple-GEM detectors provides an effective balance between high performance and operational robustness. Their widespread use in high-energy physics experiments is motivated by several key characteristics, including high effective gain, excellent spatial and time resolutions, and the flexibility offered by different gas mixtures and readout configurations. A brief overview of these aspects is presented in the following sections.

Effective gain

The effective gain is defined as

$$G = \frac{Q_D}{Q_P}, \tag{1.4}$$

where Q_D is the collected charge after multiplication and Q_P is the primary ionization charge produced by the incident particle.
Due to the electric field configuration in the vicinity of the GEM holes (Fig. 1.6), a fraction of the avalanche electrons is collected by the GEM electrodes instead of being transferred to the next amplification stage. As a result, the effective gain is always lower than the intrinsic gas gain.
High gain is essential to ensure efficient particle detection; however, increasing the amplification also leads to a higher probability of electrical discharges. As shown in Fig. 1.9, the use of multiple GEM foils allows the total amplification to be distributed over several stages, enabling triple-GEM detectors to reach effective gains over 10^4. Moreover, for a given effective gain, triple-GEM configurations

exhibit a significantly lower discharge probability compared with single- and double-GEM detectors, making them suitable for stable operation at high amplification levels.

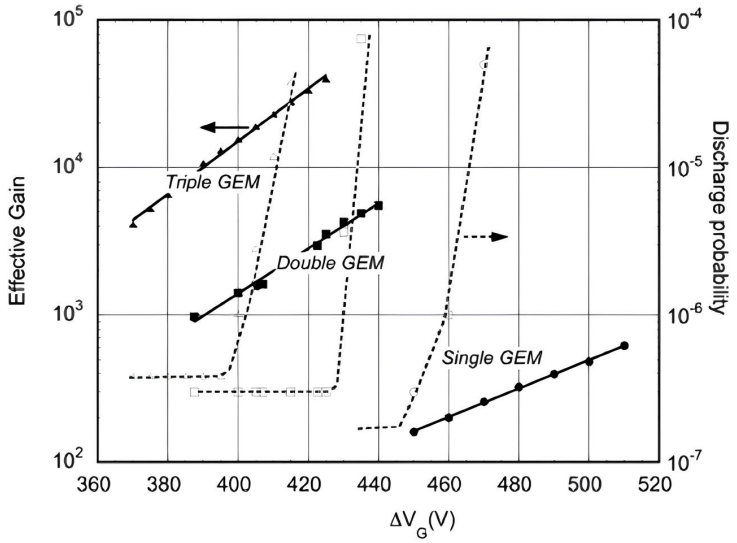


FIGURE 1.9: Effective gain (left axis) and discharge probability (right axis) as a function of the applied voltage for single-, double- and triple-GEM detectors [28].

The effective gain depends on several parameters, including the voltage applied across each GEM foil, the electric fields in the drift, transfer and induction gaps, the hole geometry, and the gas mixture. The influence of these parameters has been extensively studied both experimentally and through simulations [33, 34, 35]. In particular, the gas mixture strongly influences the achievable gain. Large gains can be achieved even in pure noble gases and their mixtures [36, 37], owing to the confinement of the electron avalanche within the GEM holes, which strongly suppresses secondary processes [28].

Spatial and time resolution

The spatial and time resolutions are key parameters characterizing the performance of GEM detectors. They depend on several factors, including the gas properties, electric field configuration, detector geometry and readout system.
The spatial resolution is mainly determined by the readout configuration and by the charge distribution induced on the readout electrodes. In strip-based readout systems, commonly used in large-area GEM detectors, the avalanche charge is

shared among neighbouring strips. The particle position can then be reconstructed from the measured charge distribution, achieving a resolution better than the strip pitch. Triple-GEM detectors can achieve spatial resolutions from a few tens to a few hundreds of micrometres, depending on the readout strip pitch and operating conditions [38, 28].
The time resolution of a GEM detector is determined by the electron transport properties in the gas and by the development of the avalanche signal. In particular, the electron drift velocity and longitudinal diffusion affect the temporal spread of the signal, while the electric field configuration can be optimized to improve the timing performance. Depending on the gas mixture and operating conditions, triple-GEM detectors can achieve time resolutions of a few nanoseconds [39, 28].

1.4 GEM detectors in CMS

The excellent performance of triple-GEM detectors has made them a key technology for the upgrade of the CMS muon system. Their capability to operate efficiently in high particle-rate environments, combined with their good spatial and time resolutions and high radiation tolerance, makes them well suited for the challenging conditions expected during the HL-LHC era.
For these reasons, triple-GEM detectors have been introduced as part of the Phase-2 upgrade of the CMS experiment. Installed in the forward (endcap) region of the muon system, they complement the existing CSCs by providing additional position measurements with high precision. Their inclusion improves the efficiency and robustness of muon reconstruction and enhances the L1 trigger performance, leading to a more accurate estimation of the muon transverse momentum and a better rejection of low-momentum background muons.
The CMS GEM upgrade includes three detector systems: GE1/1, GE2/1 and ME0. The GE1/1 and GE2/1 stations are installed in front of the first and second endcap CSC stations, respectively, improving muon triggering and reconstruction, while the ME0 detector extends the muon acceptance into the very forward region.
The discussion presented in this thesis is restricted to the GE1/1 system, which constitutes the detector technology investigated in the experimental studies described in the following chapters.
While the deployment of GEM detectors brings significant improvements to the CMS muon system, it also introduces new operational challenges. Among these,

electrical discharges and the formation of permanent short circuits represent one of the main reliability issues affecting the long-term operation of the detectors [17].

1.4.1 GE1/1

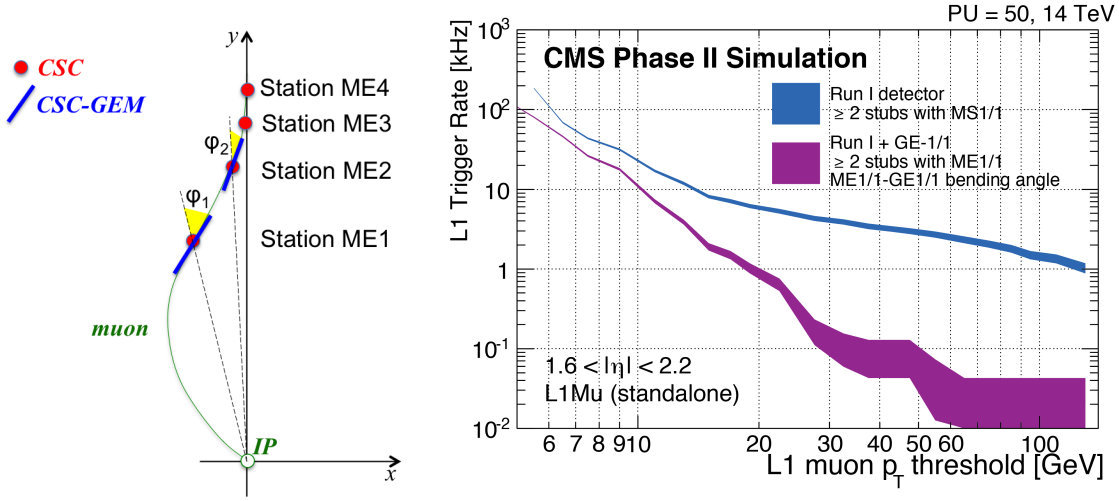
A key element of the Phase-2 muon upgrade is the deployment of GEM detectors in the endcap region. During Long Shutdown 2 (LS2, 2019-2022), GE1/1 GEM chambers were installed in CMS covering the pseudorapidity range $1.6 < |\eta| < 2.2$ (Fig. 1.4). This region experiences high particle rates and detector occupancies, posing significant challenges for efficient muon triggering and stand-alone momentum reconstruction.

GE1/1 chambers were installed immediately in front of the existing ME1/1 CSC chambers, providing an additional high-precision measurement of the muon trajectory within the first muon station.

As Fig. 1.10a shows, the additional measurement effectively increases the lever arm inside the first muon station, allowing a much more precise determination of the local bending angle. Since the magnetic field is stronger in the first muon station than in the subsequent stations, the bending angle carries significant information on the muon transverse momentum. Consequently, the combination of GE1/1 and ME1/1 substantially improves the stand-alone momentum resolution.

A more accurate momentum estimate greatly reduces the probability of misidentifying low-p_T muons as high-p_T candidates. As a result, the Level-1 muon trigger rate is significantly reduced (Fig. 1.10b), allowing the trigger thresholds to remain low while preserving high efficiency for physics processes containing relatively soft muons.

The GE1/1 station consists of trapezoidal triple-GEM chambers manufactured in two geometrical versions, referred to as Long and Short, to accommodate the mechanical constraints of the CMS endcap (Fig. 1.11a). Two triple-GEM chambers are assembled together with the same orientation, with their drift planes facing the interaction point and their readout sides facing away from it, to form a superchamber. This configuration provides two independent measurement planes, thereby increasing the overall detection efficiency. Each superchamber covers approximately a 10° sector in ϕ. A total of 72 superchambers (36 per endcap) are arranged to provide full azimuthal coverage, alternating Long and Short versions



(a) Schematic illustration of the additional lever arm provided by the GE1/1, GE2/1 and ME0 stations [24].

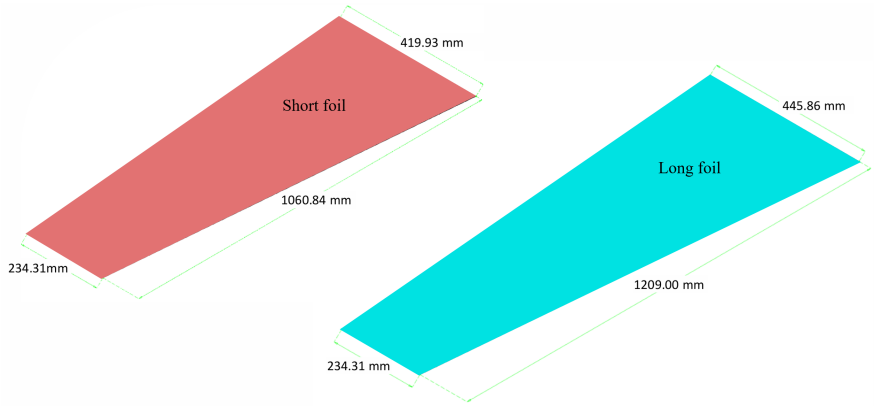
(b) Level-1 muon trigger rate as a function of the trigger threshold before and after the GE1/1 upgrade [17].

FIGURE 1.10: Impact of the GE1/1 station on the CMS Level-1 muon trigger.

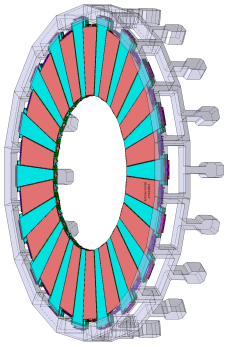
as shown in Fig. 1.11b. The complete GE1/1 ring is installed in the first CMS endcap muon station, as illustrated in Fig. 1.11c.
GE1/1 chambers operate with an Ar/CO_2 (70/30) gas mixture and a 3/1/2/1 mm drift/transfer1/transfer2/induction gap configuration. They are designed to maintain a single-chamber detection efficiency above 97% while sustaining hit rates exceeding 10 kHz/cm^2, corresponding to approximately twice the maximum hit rate expected in the GE1/1 region during HL-LHC operation. The use of two chambers in each superchamber increases the overall detection efficiency above 99.9%, ensuring the detector performance required for efficient muon triggering and reconstruction under HL-LHC operating conditions [17].

1.4.2 Discharges and short circuits in GE1/1

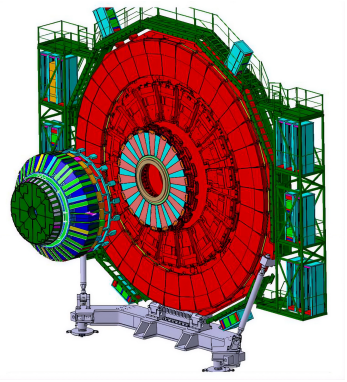
Although GEMs are generally robust against occasional electrical discharges, these events may lead to the formation of permanent short circuits, affecting the detector operating conditions and performance. Understanding the origin and consequences of these phenomena has therefore become an important aspect of the operation of the GE1/1 system.



(a) Long (right) and Short (left) GE1/1 foil geometries.



(b) Arrangement of Long and Short super-chambers forming the GE1/1 ring.



(c) Location of the GE1/1 station in the CMS endcap.

FIGURE 1.11: Geometry and installation of the GE1/1 detector station [17].

Discharges

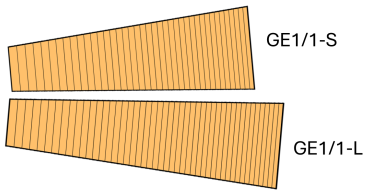
Electrical discharges are an intrinsic aspect of the operation of GEM detectors at high gas gain. Although they occur only rarely under nominal operating conditions, their probability increases at higher gains, in the presence of heavily ionizing particles and intense particle fluxes. The GE1/1 chambers operate at a gain of approximately 10^4, which is chosen as a compromise between detector performance and discharge stability. Under these conditions, a discharge can be initiated when the charge density produced during the avalanche multiplication exceeds the Raether limit [40], of the order of 10^7 electron–ion pairs. Such large avalanches can result from unusually high primary ionization, for example from heavily ionizing particles, while high particle fluxes increase the probability of

producing conditions favourable to discharge initiation. The transition from the avalanche to the streamer regime is followed by the propagation of the discharge towards the GEM electrodes, eventually causing a local electrical breakdown of the gas. Such discharges have been observed during data taking with the GE1/1 detectors in CMS in proton-proton collisions at the LHC, and remain the subject of ongoing studies aimed at understanding their origin and developing effective mitigation strategies [41, 42, 43].

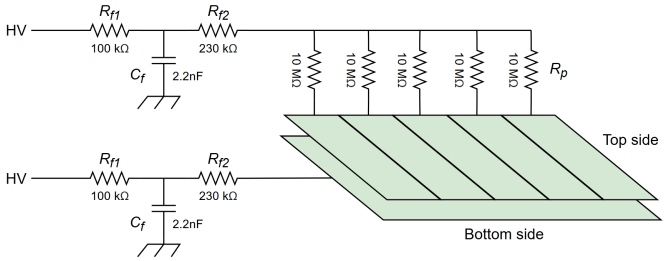
High-voltage system

The GE1/1 high-voltage (HV) distribution system has been specifically designed to ensure stable detector operation while minimizing both the probability and the consequences of electrical discharges. Fig. 1.12 illustrates the segmentation of a GEM foil together with the corresponding HV distribution network.
Each of the three GEM foils consists of two copper electrodes separated by a polyimide substrate. For every foil, the electrode facing the drift electrode (top electrode) is segmented into approximately equal-area HV sectors, whereas the opposite electrode (bottom electrode) is a continuous conductor. The top electrode is divided into 40 and 47 sectors for the GE1/1-S and GE1/1-L chambers, respectively, each covering an area of approximately $100\,\mathrm{cm}^2$ (Fig. 1.12a). This segmentation limits the energy released during a discharge, reducing the likelihood of damage severe enough to generate a permanent short circuit. Moreover, should a short circuit occur, the affected area remains confined to a single HV sector, allowing the rest of the detector to remain fully operational.
As shown in Fig. 1.12b, each top electrode HV sector is connected to the power supply through a dedicated $10\,\mathrm{M}\Omega$ protection resistor (R_p). Additional filter resistors (R_{f1} and R_{f2}), together with a filter capacitor (C_f), are included in the HV distribution network to suppress power-supply noise and ensure stable detector operation. In the event of a discharge, the protection resistor produces a voltage drop that limits the current flowing through the affected sector, thereby reducing the energy of the discharge and limiting its propagation.
In addition to the HV distribution network, the operating voltages of the three GEM foils are optimized to reduce the discharge probability. The voltage across the first GEM foil is approximately 3% higher than that across the second foil, while the second foil operates about 5% above the third. This asymmetric gain

sharing decreases the probability of streamer development while preserving the overall detector gain required for efficient operation.
Together, the asymmetric gain distribution, the sectorization of the GEM foils and the current-limiting protection resistors constitute the main design features adopted in the GE1/1 chambers to mitigate the occurrence and impact of electrical discharges [41, 42, 43].



(a) HV sectorization of the top electrodes in the GE1/1-S and GE1/1-L GEM foils.



(b) Schematic of the HV distribution network for a GEM foil.

FIGURE 1.12: High-voltage segmentation and distribution scheme of a GE1/1 GEM foil.

Short circuit formation

Although the HV distribution system is designed to minimize the effects of electrical discharges, in rare cases a discharge may lead to the formation of a permanent electrical connection between the top and bottom electrodes of a GEM foil. This phenomenon is referred to as a *short circuit*.
Short circuits can originate from different mechanisms. They may be caused by defects introduced during the manufacturing process, the presence of dust or chemical contaminants trapped inside a GEM hole, or local melting of the copper electrodes caused by repeated or particularly energetic discharges. In all these cases, a low-resistance conductive path is established between the two GEM electrodes, as schematically illustrated in Fig. 1.13.
The electrical resistance measured between the two electrodes of a healthy GEM foil exceeds 20 GΩ under controlled environmental conditions (relative humidity below 50%). In contrast, when a short circuit is present, the resistance inferred from the voltage-to-current ratio at the power-supply side is reduced to values of about 10 MΩ, corresponding to the protection resistor connected to the affected HV sector, or even lower in the case of multiple short circuits [42, 43, 44].

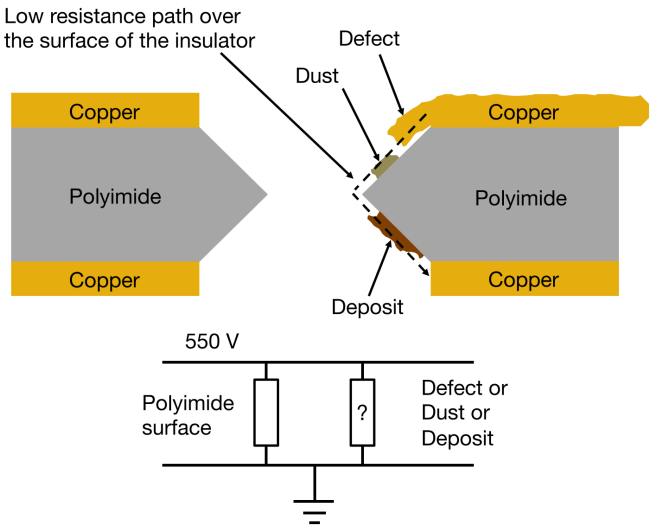


FIGURE 1.13: Formation of a low-resistance conductive path through a GEM foil and its equivalent electrical model [44].

Electrical consequences of a short circuit

The presence of a permanent short circuit forces the affected top HV sector and the bottom electrode to the same electrical potential, suppressing the amplification across the corresponding region of the GEM foil. Owing to the segmentation of the top electrode, the loss of amplification is confined to a single HV sector, corresponding to approximately 2.5% and 2.1% of the active area for the GE1/1-S and GE1/1-L chambers, respectively [42, 43].

The formation of a permanent short circuit establishes a conductive path between the top and bottom electrodes of a GEM foil. As a consequence, a current I_{short} flows through the affected HV sector, as illustrated in Fig. 1.14a. If the conductive bridge between top and bottom electrodes is assumed to have negligible resistance, this current can be calculated as

$$I_{short} = \frac{V_{top}}{R_f^{top} + R_f^{bot} + R_p^s}, \tag{1.5}$$

where V_{top} is the nominal voltage applied between top and bottom electrodes, R_f^{top} and R_f^{bot} denote the filter resistors connected to the top and bottom electrodes of the affected GEM foil, and R_p^s is the protection resistance in which the current flows.

Although a GE1/1 GEM foil is segmented into 40 (47) HV sectors, the effect of

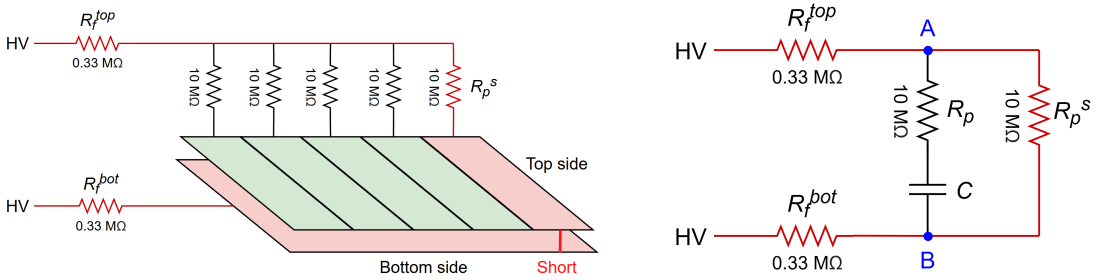
a short circuit can be understood by considering the simplified equivalent circuit shown in Fig. 1.14b, where only one healthy and one shorted sector are represented. The current flowing through the shorted branch modifies the voltage distribution within the HV network. As a consequence, the filter and protection resistors form a voltage divider, so that only a fraction of the nominal voltage V_{top} appears between nodes A and B:

$$V_{AB} = V_{top} \frac{R_p^s}{R_f^{top} + R_f^{bot} + R_p^s} = I_{short}\ R_p^s. \tag{1.6}$$

Since no current flows through the healthy branch, the entire voltage V_{AB} appears across its capacitor. Therefore,

$$\Delta V_C = V_{AB}, \tag{1.7}$$

where ΔV_C represents the voltage remaining across the healthy GEM sectors and therefore available for charge amplification.



(a) Schematic of the HV distribution network for a GEM foil with a sector affected by a short circuit.

(b) Simplified equivalent circuit of a GEM foil with one shorted sector.

FIGURE 1.14: Representation of a GEM foil affected by a permanent short circuit. The current path is highlighted in red.

As can be seen from Eq. (1.6), the after-short remaining voltage is lower than the one applied with the generator ($\Delta V_c < V_{top}$). Consequently, the gas gain of the unaffected sectors is reduced with respect to nominal operating conditions. The difference between the nominal and the remaining voltage corresponds to the voltage dropped across the two filter resistors,

$$V_{drop} = V_{top} - V_{AB} = I_{short}\,(R_f^{top} + R_f^{bot}) \tag{1.8}$$

which follows directly from Eqs. (1.5) and (1.6).

If multiple sectors of the same GEM foil are affected by short circuits, the equivalent protection resistance of the shorted branches is given by the parallel combination of the corresponding protection resistors. Assuming all protection resistors have the same value, the equivalent resistance becomes

$$R^s_{p,eq} = \frac{1}{\sum_{i=1}^{n} \frac{1}{R^s_{p,i}}} = \frac{R^s_p}{n} = \frac{10\,\mathrm{M\Omega}}{n}. \tag{1.9}$$

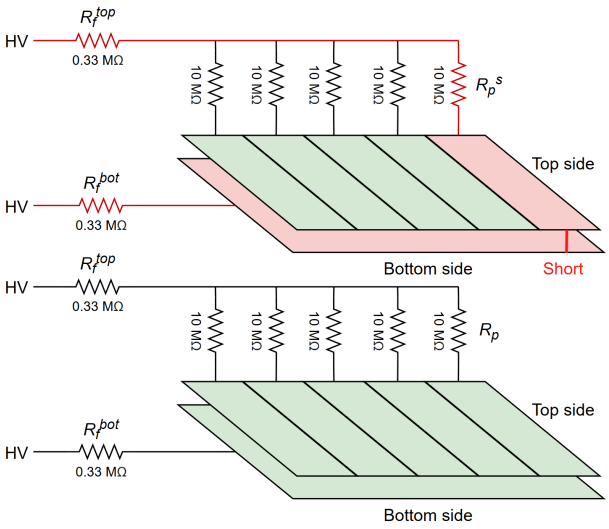
As follows from Eqs. (1.9) and (1.6), the voltage available across the healthy sectors decreases with the number of shorted sectors.
The reduction of the voltage across the shorted GEM foil not only decreases the gain of the affected foil, but also modifies the potential of its bottom electrode, thereby affecting the electric field in the subsequent gas gap.
As illustrated in Fig. 1.15, the current flowing through the bottom filter resistor of the shorted GEM foil produces a voltage drop across R^{bot}_f. As a consequence, the potential of the bottom electrode differs from its nominal value according to

$$V^{phys}_{bot} = V_{bot} + I_{short} \cdot R^{bot}_f. \tag{1.10}$$

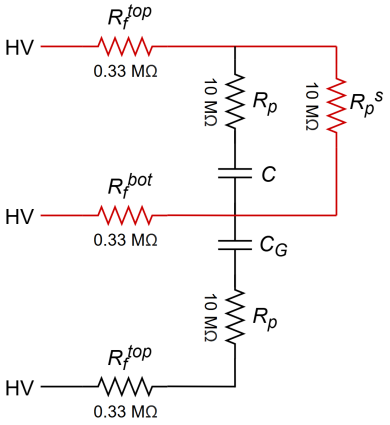
Since the potential of the following electrode is unaffected by the short-circuit current, the voltage difference across the subsequent transfer (or induction) gap increases with respect to the nominal configuration, leading to a higher electric field in that gap.
It is important to note that the increase in the gap voltage (Eq. (1.10)) is smaller than the voltage reduction across the shorted GEM foil (Eq. (1.8)). For GE1/1, where $R^{top}_f = R^{bot}_f = 0.33\,\mathrm{M\Omega}$, the increase is therefore half of the reduction.
Although smaller than the reduction of the GEM voltage, the increase of the electric field in the subsequent gap can influence the detector response and therefore deserves dedicated investigation (Section 3.5).

Operational experience during Run 3

The first years of operation of the GE1/1 station during LHC Run 3 provided the first large-scale assessment of the detector performance under realistic experimental conditions. During proton–proton collisions, each HV channel exhibits a non-zero baseline current originating from the continuous amplification of ionization electrons. Electrical discharges appear as sharp current spikes superimposed on this baseline,



(a) Schematic of the HV distribution network for a GEM foil with a sector affected by a short circuit and the healthy subsequent one.



(b) Simplified equivalent circuit of the bottom face of a GEM foil with one shorted sector and the upper face of the subsequent healthy electrode.

FIGURE 1.15: Representation of a GEM foil affected by a permanent short circuit and the subsequent healthy foil. The current path is highlighted in red.

and their occurrence was found to depend on the detector operating conditions and on the instantaneous luminosity.

As expected for GEM detectors, the chambers initially experienced a relatively high discharge rate when operated at the nominal working point. Following the first irradiation period, however, a progressive reduction of the discharge rate was observed even under unchanged operating conditions, indicating a conditioning effect of the GEM foils. In parallel, the detector operating voltage was optimized, leading to a substantial decrease in the discharge rate while preserving stable detector operation.

Despite the reduction in the discharge rate, short circuits were observed in several GE1/1 chambers during Run 3. The monitoring of the HV currents allowed both the generation and the subsequent healing of individual short circuits to be identified. In particular, a healing event corresponds to the recovery of the affected HV sector, accompanied by a reduction of the current drawn by the short circuit. In some cases, this reduction occurred gradually, indicating a progressive increase of the resistance of the electrical connection. This behaviour was interpreted as a gradual consumption of the electrical contact responsible for the short circuit, possibly due

to chemical processes occurring inside the detector [42]. Therefore, the formation of a short circuit cannot necessarily be regarded as an irreversible event. At the same time, healing does not imply that short circuits cease to represent an operational issue, since not all observed short circuits recover during the observation period. The occurrence of short circuits was not uniformly distributed among the three GEM foils. In particular, GEM3 was found to be involved in the generation of short circuits approximately twice as often as GEM1 and GEM2. This behaviour was tentatively attributed to the larger amount of charge collected by GEM3, which constitutes the final stage of the avalanche multiplication process [42]. The distribution of the observed events over the three foils during the 2021–2023 period is reported in Table 1.1. A total of 112 short-circuit generation events and 73 healing events were identified. These numbers refer to observed events rather than to unique GEM foils or detector chambers: a foil or a sector that heals may subsequently experience another short circuit or it can be affected by multiple short circuits at the same time, and therefore contribute more than once to the reported counts. Consequently, the values in Table 1.1 should not be interpreted as the number of distinct foils affected by short circuits.

GEM foil	**New short circuits**	**Healed short circuits**
GEM1	34	25
GEM2	21	10
GEM3	57	38
Total	112	73

TABLE 1.1: Number of short-circuit generation and healing events observed for the three GEM foils of the GE1/1 chambers during the 2021–2023 period.

The time evolution of the healing process also shows that recovery does not occur on a single characteristic timescale. The observed healing times span several orders of magnitude, from approximately 10^{-4} days to 10^{2} days. This broad distribution further highlights the dynamic nature of the phenomenon: when a short circuit heals, the recovery of the affected sector can occur on timescales ranging from seconds to several months. Moreover, since a fraction of the observed short circuits does not heal within the considered observation period, the occurrence of healing cannot be regarded as a mechanism that removes the operational impact of short circuits.

Another relevant observation is that most short-circuit events involved the generation or healing of a single HV sector at a given time [42]. This is consistent with the segmented HV distribution adopted in GE1/1, which confines the electrical effects of a short circuit to a limited portion of the detector. Nevertheless, the localized nature of the phenomenon also means that the operating conditions of the affected sector can differ from those of the surrounding detector. The resulting modification of the local HV configuration can therefore affect the electric fields in the GEM structure and, consequently, the detector response.

The formation and evolution of short circuits were also observed to depend on the detector operating conditions. In particular, studies performed during GE1/1 operation investigated the role of the applied high voltage and of the magnetic field [45] on detector stability, showing that the occurrence of discharges and short circuits cannot be described solely in terms of static properties of the GEM foils [42, 43]. These observations are particularly relevant for a detector operating in the CMS environment, where the high-voltage configuration and magnetic field evolve according to the experimental conditions.

Overall, the Run 3 experience demonstrated that short circuits are a non-negligible and dynamic phenomenon in triple-GEM detectors. Their occurrence is localized at the sector level, their probability is not uniform among the three GEM foils, and their evolution can involve either persistent short circuits or a healing process occurring over widely different timescales. Although the HV segmentation limits the region directly affected by a short circuit, the associated modification of the local voltage distribution can alter the electric fields and the detector response. These observations motivate a dedicated study of the effects of short circuits under controlled laboratory conditions. In particular, the experimental work presented in the following chapters aims to quantify the impact of an increasing number of short circuits on the performance of a triple-GEM detector and to investigate possible strategies for compensating their effects.

Chapter 2

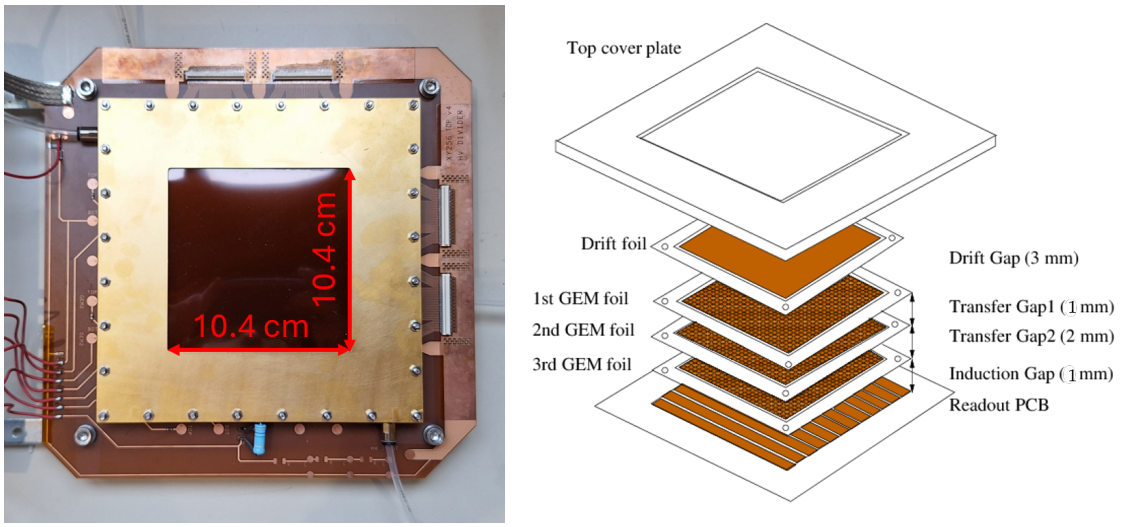
Experimental setup and detector characterization

This chapter describes the experimental setup developed to investigate the behaviour of a triple-GEM detector in the presence of short circuits. Since the study is motivated by the short-circuit problem observed in the GE1/1 detectors of the CMS experiment, a 10×10 triple-GEM detector was used as a laboratory-scale system in which short-circuit conditions could be reproduced and studied in a controlled setup.
The chapter first describes the detector and the main components of the experimental setup, including the gas system, the high-voltage supply and distribution, as well as the data acquisition and monitoring systems. The procedures used to characterize the detector under nominal operating conditions are then presented. The goal of this characterization is therefore to establish a reference set of performance parameters under nominal operating conditions, against which the impact of GEM foil short circuits can subsequently be quantified.

2.1 10×10 triple-GEM

The experimental studies presented in this thesis were performed using a 10×10 triple-GEM detector specifically assembled for laboratory investigations. Although considerably smaller than the GE1/1 chambers employed in CMS, the detector preserves all the essential characteristics governing its operation. The geometry of the GEM foils, the drift, transfer and induction gap configuration, the applied electric fields, and the gas mixture are identical to those adopted in the CMS detectors. Since the processes responsible for charge transport, gas amplification and electrical discharges are local phenomena determined primarily by these parameters,

their behaviour is largely independent of the detector active area. Consequently, a reduced-area detector provides a representative and flexible setup for investigating the effects of short circuits under controlled laboratory conditions while significantly simplifying the experimental setup and reducing operational complexity.
The detector employed in this work, shown in Fig. 2.1, has an active area of $10.4 \times 10.4\,\mathrm{cm}^2$. It is therefore referred to as the 10×10 triple-GEM throughout this work, with the name indicating its approximately $10 \times 10\,\mathrm{cm}^2$ active area. As illustrated in Fig. 2.1b, it adopts the same 3/1/2/1 mm drift/transfer1/transfer2/ induction gap configuration as the CMS GE1/1 chambers. During all measurements, the detector was operated with an Ar/CO_2 (70/30) gas mixture under continuous gas flow and with the same electric field configuration adopted for GE1/1 operation.



(a) Photograph of the 10×10 triple-GEM detector used throughout this work.

(b) Schematic view of the 10×10 triple-GEM detector [46].

FIGURE 2.1: 10×10 triple-GEM detector employed for the experimental studies.

The detector consists of three GEM foils, a drift cathode and a readout board enclosed in a sealed volume filled with gas and delimited by the top cover plate and the readout board itself. The cathode and the three GEM foils are fully bathed in the continuously flowing gas mixture.
The top cover consists of a frame supporting a polyimide window matching the detector active area. The drift cathode is mounted immediately below the window, while the three GEM foils are separated by glass-fiber spacer frames defining the drift, transfer and induction gaps.

Unlike the GE1/1 chambers, whose GEM foils feature top electrodes segmented into independent HV sectors as described in Section 1.4.2, the GEM foils of the 10×10 detector do not feature such segmentation. This difference is relevant for the study presented in this thesis, as it prevents the direct reproduction of a short circuit affecting a single HV sector. The strategy adopted to overcome this limitation is described in Section 3.3.
The readout board consists of an FR4 printed circuit board (PCB) patterned with 200 copper readout strips arranged in two orthogonal layers, providing two-dimensional position sensitivity.

2.2 Gas supply

The detector is operated under continuous gas flow provided by the gas distribution system shown in Fig. 2.2. The system is supplied by a pressurized gas cylinder containing an Ar/CO_2 (70/30) gas mixture.

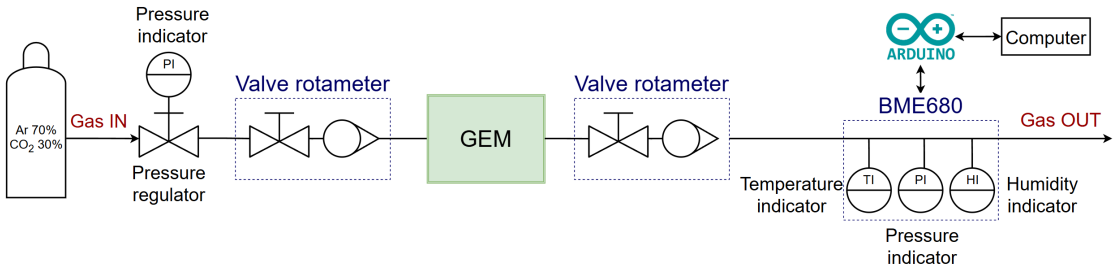
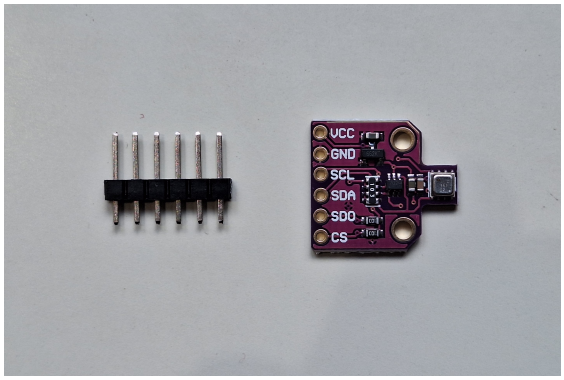


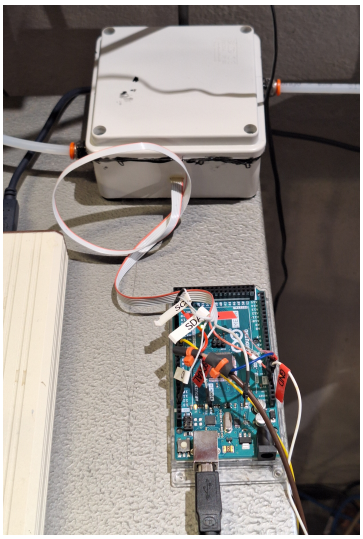
FIGURE 2.2: Schematic representation of the gas supply system.

Immediately downstream of the gas cylinder, a pressure regulator reduces the gas pressure from a maximum of approximately 200 bar to a constant output pressure of 0.5 bar. The gas then passes through an inlet variable-area flowmeter (rotameter), which is used to regulate and monitor the gas flow. During all measurements, the flow rate was set to 2 L/h.
The gas enters the detector, continuously flushing the gas volume, and exits through a second rotameter located at the outlet. The outlet rotameter provides a cross-check for possible gas leaks within the detector. Under normal operating conditions, with the outlet valve fully open, the flow rate measured at the outlet should match that measured at the inlet.
As shown in Fig. 2.3b, before being vented to the atmosphere, the gas flows through a sealed monitoring chamber housing a BME680 environmental sensor [47]

(Fig. 2.3a), which continuously measures the gas temperature, pressure and relative humidity. The sensor is powered by an Arduino Mega 2560 board [48] through the 5 V and GND lines and communicates with the microcontroller via the I^2C serial interface using the SDA (Serial Data) and SCL (Serial Clock) lines. The Arduino periodically acquires the sensor readings and transmits them to the control computer via a USB connection.



(a) BME680 sensor and its electrical connections before installation.



(b) Box housing the BME680 sensor and the Arduino used to read and transmit the sensor data.

FIGURE 2.3: BME680-based system used to monitor the temperature, pressure, and humidity of the gas supply system.

2.3 High Voltage supply

The high-voltage system used to operate the detector is described in the following, starting from the hardware components and their connection to the detector, and then moving to the software-based management of the applied voltages.

2.3.1 HV supply system

Fig. 2.4 shows the HV supply chain employed to power the GEM detector in the experimental setup.

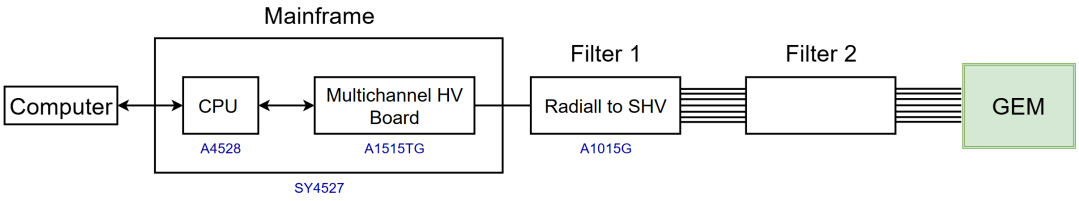
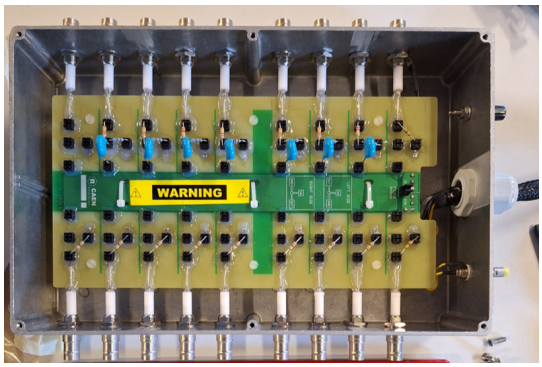


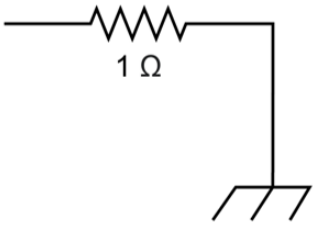
FIGURE 2.4: Schematic representation of the high-voltage supply chain used to power the GEM detector.

The core of the HV supply system is the CAEN SY4527 HV mainframe, which is equipped with two main modules: the CAEN A4528 CPU controller and the CAEN A1515TG eight-channel HV board. The CPU controller allows the mainframe to be remotely operated from a computer through an Ethernet connection, enabling the user to configure, monitor and control the high-voltage channels through the CAEN GECO software interface (Section 2.3.2).
The A1515TG board provides eight independently programmable high-voltage channels, used to establish the potential differences between the detector electrodes. The eight HV outputs are routed outside the mainframe through a Radiall connector and subsequently pass through two filtering stages before reaching the detector electrodes. The filters attenuate electrical noise on the high-voltage lines and provide protection against possible discharges occurring within the detector.
The first filtering stage is provided by the CAEN A1015G box, which implements a resistive-capacitive (RC) filter analogous to the one described in Section 1.4.2, with the only difference being the value of the filter resistor R_{f2}, which is 220 kΩ in the CAEN box. As shown in Fig. 2.5a, the box provides 18 output channels, of which only the eight channels in the upper-right section are used in the setup. The eight HV channels are routed through the box and distributed to eight independent SHV outputs. The first of these channels is dedicated to the anode and is connected to ground through a 1 Ω resistor (Fig. 2.5b), since the GEM anode is operated at ground potential.
A second filtering stage was subsequently introduced close to the detector. Although the A1015G filter already provides filtering of the HV lines, its relatively large distance from the detector was associated with significant electrical noise in the acquired signals. To further suppress this noise, an additional filter was installed immediately upstream of the detector (Fig. 2.5c). Each of its seven HV channels consists of a series of three 100 kΩ resistors, with two 2.2 nF capacitors connected

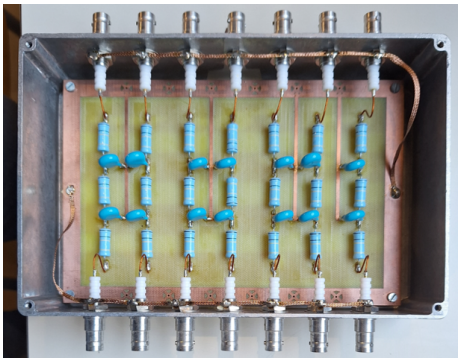
between the intermediate nodes and ground, as shown in Fig. 2.5d.



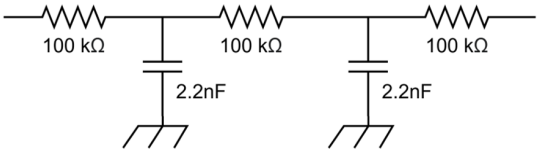
(a) Interior of the CAEN A1015G filter box, showing the Radiall input and the eight SHV output channels.



(b) Electrical schematic of the grounded anode channel of the CAEN A1015G filter.



(c) Interior of the additional HV filter installed close to the detector.



(d) Electrical schematic of one of the seven identical channels of the additional HV filter.

FIGURE 2.5: HV filtering stages employed in the experimental setup.

2.3.2 HV supply management

The operation of the detector requires the seven voltages between electrodes to be set according to well-defined configurations. The following subsections describe how these configurations are defined and managed during the measurements, both through the control software and through the automated setting procedure.

GEM voltage configuration and equivalent current

The voltage configuration of the detector is defined by the seven voltage differences applied between its electrodes. In the experimental setup, these voltage differences are controlled independently through seven HV channels, labelled as Drift, G1Top, G1Bot, G2Top, G2Bot, G3Top, and G3Bot. The Drift voltage corresponds to the potential difference between the cathode and the top electrode of the first GEM foil, while G1Top, G2Top, and G3Top correspond to the voltage differences across the three GEM foils, respectively. G1Bot and G2Bot define the voltage differences across the first and second transfer gaps, while G3Bot defines the voltage difference across the induction gap.
To identify the overall voltage configuration with a single parameter, the convention adopted for the CMS GEM detectors is followed [42]. The operating point is expressed in terms of an equivalent divider current, I_{eq}, defined as the current that would flow through a reference resistive divider providing the same voltage configuration. The reference divider, shown in Fig. 2.6, fixes the relative voltage differences between the seven channels. Therefore, once I_{eq} is specified, the voltage difference associated with each channel can be calculated as

$$\Delta V_i = R_i \, I_{\text{eq}}, \tag{2.1}$$

where R_i is the corresponding resistance of the reference divider.
The reference divider was not physically used to power the detector during the measurements. Instead, the seven HV channels were controlled independently, and their voltage values were calculated according to the resistance ratios of the reference divider. The corresponding I_{eq} value was then used to identify the complete voltage configuration. An example of the voltage configuration corresponding to a representative value of I_{eq} is reported in Table 2.1.
This convention provides a convenient way of describing the detector operating point with a single parameter and allows measurements performed under different voltage configurations to be readily compared.

GECO software

The voltages applied between the seven detector electrodes were set and monitored through the GECO software installed on the control computer. The main elements of the GECO interface used for the HV management are shown in Fig. 2.7. Each row

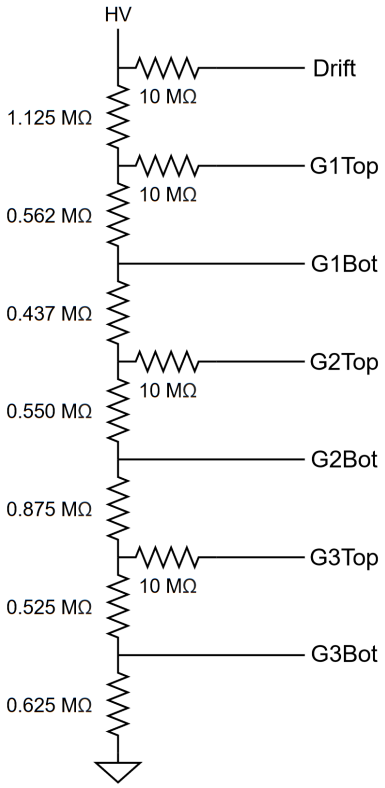


FIGURE 2.6: Electrical schematic of the reference resistive divider. The resistance values of the seven vertical resistors correspond to the R_i terms used in Eq. (2.1).

Channel	**Voltage [V]**
Drift	787.5
G1Top	392.0
G1Bot	306.6
G2Top	385.0
G2Bot	612.5
G3Top	367.5
G3Bot	437.5
Total	3288.6

TABLE 2.1: Voltage applied to each channel for a configuration corresponding to $I_{\text{eq}} = 700\,\mu\text{A}$.

corresponds to an individual HV channel, while the columns provide information on its settings, monitored values, and operating status.
The `Name` column identifies each channel through the label of the voltage difference it sets (Drift, G1Top, G1Bot, G2Top, G2Bot, G3Top, and G3Bot). The voltage applied to a channel is set through the `V0Set` field, while `VMon` reports the corresponding monitored voltage. Similarly, `IMon` displays the current measured on the HV power supply channel. The `Pw` parameter indicates whether the channel is powered, whereas `Status` reports its current operating state.
The interface also provides several parameters for controlling the channel protection and voltage ramping. The `I0Set` parameter defines the maximum allowed current for the channel. If the current exceeds this value for longer than the time specified by the `Trip` parameter, a trip is triggered, causing the HV channels to be switched off as a protection measure. The voltage ramp-up and ramp-down rates can be set independently through the `RUp` and `RDWn` parameters, respectively, expressed in V/s.

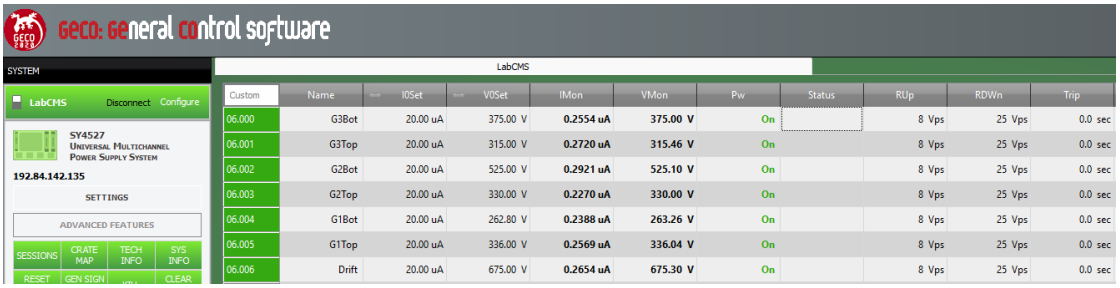


FIGURE 2.7: GECO software interface used to control and monitor the HV channels.

HV setting automation

In order to automate the setting and changing of the HV channels over time, I developed a C program that interfaces directly with the CAEN HV system. The automation made it possible to perform continuous data acquisition over extended periods of time, including periods in which no personnel were present in the laboratory. This was particularly useful in combination with the automated data acquisition system described in Section 2.4.1.
The program allows a sequence of different voltage configurations to be defined before starting the measurement. Each configuration can be specified either by a

single I_{eq} value or by directly providing the voltage values for the seven channels. In the former case, the seven voltages are calculated automatically according to the reference divider ratios (Section 2.3.2). The possibility of directly specifying the individual voltages was particularly useful for configurations in which the voltage of a single channel was reduced by a predefined percentage with respect to the nominal configuration. The duration for which each configuration is maintained is also defined in advance.

Once a configuration is selected, the program first sets the current protection threshold of all channels to the value specified for the voltage ramping phase. In the configurations used for the measurements, this value is set to 10 µA. The target voltage of the first channel is then applied while the program monitors the voltage through the `VMon` parameter. The program waits until the monitored voltage reaches the target value within a tolerance of 5%, before proceeding to the following channel. This procedure is repeated for all seven channels, ensuring that the voltage configuration is reached progressively rather than changing all channels simultaneously.

After all seven channels have reached their target voltages, an additional stabilization time of 60 s is introduced. The current protection threshold is then reduced to its nominal value, set to 0.5 µA for the configurations used in this work. The selected voltage configuration is subsequently maintained for the predefined duration, during which the data acquisition is performed.

During the measurement, the program also periodically checks the communication with the HV system. In case of a communication failure, it attempts to re-establish the connection automatically. If the connection is successfully restored, the measurement proceeds without interruption. If the reconnection attempts fail, the program terminates while leaving the HV configuration unchanged and sends a notification of the interruption. This allows the operator to remotely identify the problem and restart the measurement from the control computer. This feature was implemented to increase the robustness of the automated procedure during long unattended acquisitions.

2.4 Data acquisition chain

The detector response is investigated through three complementary measurements: counting rate, readout-strip current, and signal amplitude spectrum. The counting-rate measurement is based on the G3Bot signal and uses a chain of amplification and discrimination followed by conversion to a TTL-compatible signal for digital counting. The readout-strip current is measured directly with a picoammeter, while the signal amplitude is acquired from the G3Bot signal through amplification and processed by a multichannel analyzer (MCA). The specific acquisition chains are described in detail together with the corresponding detector characterization measurements in Section 2.5.

2.4.1 DAQ automation

The only measurement that I automated is the counting-rate measurement, as it requires the longest acquisition times.
The two configurations used for the counting-rate acquisition are schematically illustrated in Fig. 2.8.

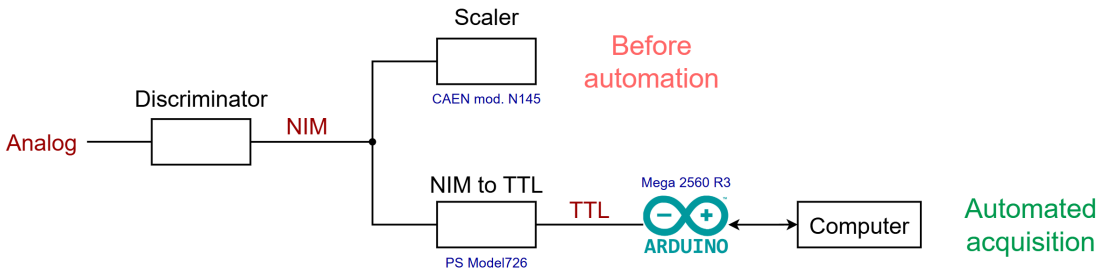


FIGURE 2.8: Schematic representation of the final part of the counting-rate acquisition chain. The upper branch corresponds to the setup used before the introduction of the data acquisition automation, while the lower branch shows the configuration implemented for the automated acquisition.

Before the introduction of the automation, the discriminated NIM signals were counted using the CAEN Mod. N145 Quad Scaler and Preset Counter-Timer, shown in Fig. 2.9, to determine the counting rate.
Fig. 2.9 shows all the NIM modules that have been employed in this work. Specific instrument and module models are stated explicitly only the first time they are

mentioned in this work. Whenever a given instrument or module type is subsequently referred to without repeating the model, it should be understood to be the same one specified at its first occurrence.
The scaler allows only one measurement to be performed at a time, after which the operator has to manually record the measured count and restart the measurement. This procedure therefore cannot be performed remotely or used for a sequence of consecutive measurements without the presence of an operator.

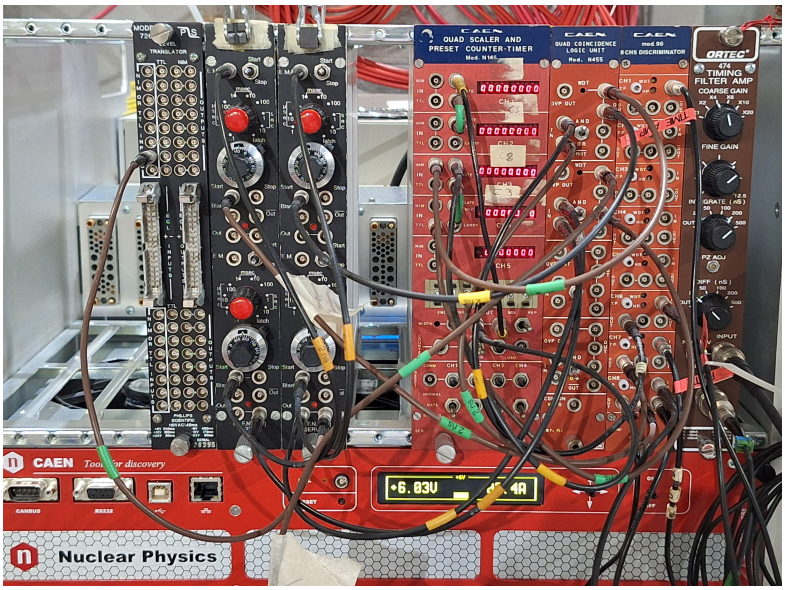


FIGURE 2.9: NIM crate with all the employed modules. From right to left: shaper, discriminator, logic unit, scaler, two dual gate generators, NIM-to-TTL converter.

The basic idea to automate this procedure was to exploit the digital inputs of the Arduino to count the incoming pulses and determine the corresponding counting rate. The NIM signal, however, does not reach a sufficiently high voltage level to be reliably recognized as a `HIGH` state by the Arduino digital input. NIM (Nuclear Instrumentation Module) signals use negative voltage levels, with the active state typically corresponding to approximately $-0.8\,\mathrm{V}$, whereas TTL (Transistor-Transistor Logic) signals use positive logic levels, with a `HIGH` state corresponding to a voltage above approximately $2\,\mathrm{V}$. A NIM-to-TTL conversion, performed with the Phillips Scientific Model 726 (Fig. 2.9), was therefore required to increase the signal amplitude to the voltage level required by the Arduino.
The setup allows the counting rates from two different sources to be recorded simultaneously.

The Arduino communicates with the control computer through the USB serial connection. At each acquisition cycle, the computer sends a request to the Arduino, which reads the environmental parameters from the BME680 sensor and retrieves the number of pulses accumulated since the previous request. The counters are then reset, and the measured quantities are transmitted to the computer through the serial interface. In this way, the time interval between two consecutive requests defines the counting interval, allowing the counting rate to be determined from the number of detected pulses and the corresponding acquisition time.

2.4.2 Remote monitoring via Grafana

The data collected by the Arduino are processed by a Python script running on the control computer. The script periodically requests the measurement data from the Arduino through the USB serial connection and stores them in a local InfluxDB database. In addition to the quantities directly measured by the Arduino (the two counting rates and pressure, temperature, and humidity of the gas), the script retrieves the latest monitored HV voltages and currents from the log file generated by the HV control program.
The collected quantities are therefore stored together in a common time-dependent database, allowing the detector operating conditions, gas parameters, and counting rates to be monitored simultaneously. Grafana, a data visualization and monitoring tool, is connected to the InfluxDB database and provides a graphical interface for visualizing these data through dedicated dashboards (Fig. 2.10).
This configuration allowed us to remotely monitor the measurements during long unattended acquisitions. In particular, the counting rates, environmental parameters, and HV values could be inspected remotely, making it possible to identify possible anomalies in the detector operation without being physically present in the laboratory.
Grafana also proved useful during the subsequent data analysis. Since the recorded quantities can be visualized as a function of time, the dashboards allowed us to easily identify the time intervals corresponding to individual measurements. Once the relevant time interval was identified, I used a dedicated Python script to retrieve the corresponding data from the InfluxDB database. The monitored counting rates, the seven HV channels, and the environmental parameters measured by the



FIGURE 2.10: Example of the Grafana dashboard. Starting from the top-left panel and moving clockwise: the two counting channels, the seven channels voltages, the seven channels currents, and the gas pressure, humidity, and temperature.

BME680 were retrieved simultaneously and stored according to their timestamps in a single CSV file, which was subsequently used as input for the data analysis.

2.5 GEM characterization

Before investigating the detector response in the presence of short circuits, the performance of the 10×10 triple-GEM detector was characterized under nominal operating conditions. This preliminary characterization provides a reference for the detector performance in the absence of short circuits and establishes the baseline operating conditions for the measurements presented in the following sections.
Three complementary measurements were performed to characterize the detector response: the effective gain, its spatial uniformity, and the detection efficiency. The gain characterizes the charge amplification capability of the detector, while the uniformity measurement provides information on the spatial dependence of its response. The efficiency, instead, evaluates the probability of detecting a particle crossing the detector. Together, these measurements provide a comprehensive baseline characterization of the detector performance.

2.5.1 Gain measurement

The effective gain of a detector is a key parameter characterizing its performance. Moreover, the gain as a function of the applied voltage is an important tool for determining the optimal operating point of a GEM detector, where a suitable compromise between detector performance and discharge probability is achieved, as discussed in Section 1.3.3.
Starting from the definition of the effective gain given in Eq. (1.4), the charge Q_D in the numerator can be experimentally determined from the anode current I_a. For a measurement performed over a time interval t, the total charge collected by the detector is

$$Q_D = I_a\, t. \tag{2.2}$$

During the same time interval, the total primary charge produced by the incident particles is

$$Q_P = e\, n_e\, R\, t, \tag{2.3}$$

where e is the elementary charge, n_e is the average number of primary electrons produced by a single incident particle, and R is the particle rate.
Substituting these expressions into Eq. (1.4) gives

$$G(HV) = \frac{I_a(HV)}{e\, n_e\, R}, \tag{2.4}$$

where the dependence of the gain on the applied high voltage is made explicit. Thus, for a given operating voltage, the detector gain can be determined from the corresponding anode current. This relation is used throughout this work to obtain the gain curve as a function of the GEM detector supply voltage.
The number of primary electrons n_e can be estimated for photon irradiation in an Ar/CO_2 gas mixture as

$$n_e = E_\gamma \left(\frac{\%\mathrm{Ar}}{W_i(\mathrm{Ar})} + \frac{\%\mathrm{CO_2}}{W_i(\mathrm{CO_2})} \right), \tag{2.5}$$

where E_γ is the energy of the incident photon in eV, %Ar and $\%CO_2$ are the percentages of the two gases in the mixture, and $W_i(\mathrm{Ar})$ and $W_i(\mathrm{CO_2})$ are the

corresponding work functions, i.e. the mean energies required for the production of an electron-ion pair in the two gases [49].

Experimental setup

Following Eq. (2.4), two quantities must be determined to measure the detector gain: the interaction rate R and the anode current I_a. Therefore, the experimental setup shown in Fig. 2.11 is divided into two parallel acquisition chains.

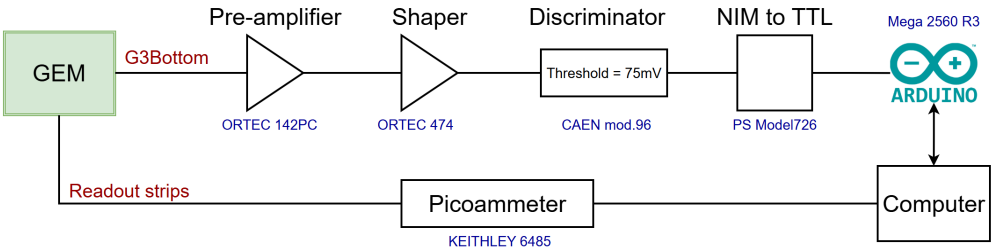


FIGURE 2.11: Schematic representation of the data acquisition chain for gain measurement.

The current signal is collected from the readout strips. The 200 readout strips of the GEM detector are divided into four groups of 50 strips. Each group is connected to a Panasonic-to-LEMO adapter, and the four outputs are connected in series using LEMO cables, as shown in Fig. 2.12, in order to obtain a single current signal. The resulting signal is measured with a KEITHLEY 6485 picoammeter, which can be remotely controlled and read out from the computer.
The particle rate is determined by counting the voltage signals produced by the detector. A voltage signal is extracted from the G3Bot through a CR circuit implemented on the readout board, which decouples the DC high voltage supplying the G3Bot from the signal readout electronics. The signal is first amplified by the ORTEC 142PC preamplifier and then processed by the ORTEC 474 shaper (Fig. 2.9). The CAEN Mod. 96 (Fig. 2.9) discriminator is subsequently used to discriminate the signal and generate a NIM output signal. This signal is then converted to TTL and transmitted to the computer through the Arduino, as described in Section 2.4.1.

Rate measurement

The particle rate R entering Eq. (2.4) is determined from the counting rate measured by the detector as a function of the applied voltage. As the voltage is increased,

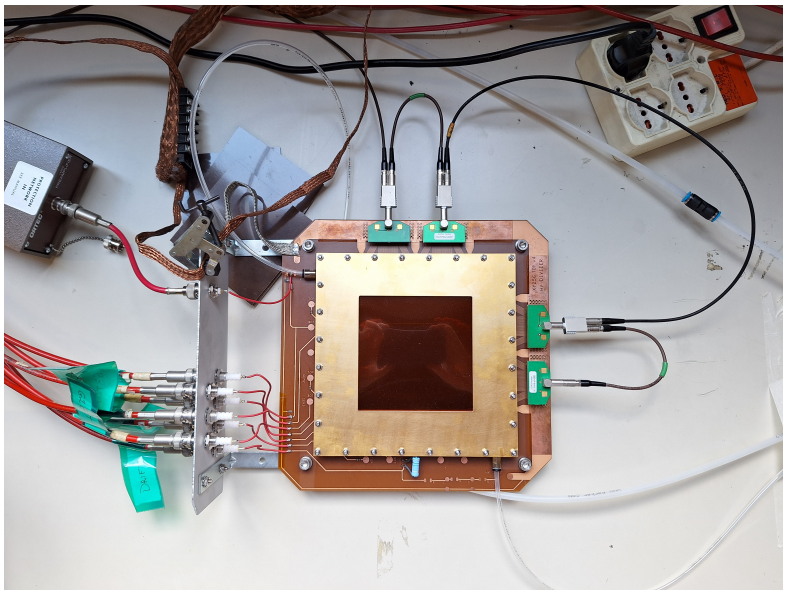


FIGURE 2.12: GEM detector setup for current measurement, with the four groups of readout strips connected in series.

the counting rate increases and eventually reaches a plateau. The plateau value is taken as the particle rate R used in the gain calculation.
I used two radioactive sources for this measurement (shown in Fig. 2.13): ^{55}Fe and ^{109}Cd.



FIGURE 2.13: The two radioactive sources employed for rate measurements.

The ^{55}Fe source decays by electron capture according to

$$^{55}\mathrm{Fe} + e^- \rightarrow {}^{55}\mathrm{Mn}^* + \nu_e. \tag{2.6}$$

The subsequent atomic relaxation of the daughter atom produces characteristic Mn X-rays, with the main K_α emission at approximately 5.9 keV [50].
These 5.9 keV photons constitute the main X-ray emission from the ^{55}Fe source contributing to the detector response.
The ^{109}Cd source also decays by electron capture,

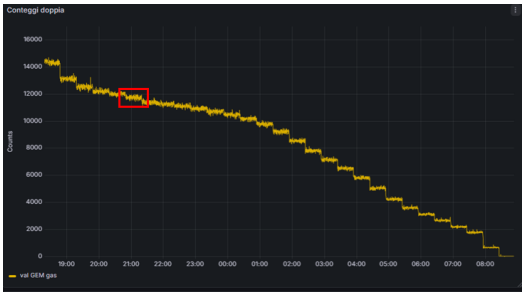
$$^{109}\mathrm{Cd} + e^- \rightarrow {}^{109}\mathrm{Ag}^* + \nu_e. \tag{2.7}$$

The atomic relaxation following the electron capture produces characteristic Ag X-rays, with the main K_α line at approximately 22.1 keV [50].
These photons can interact with the copper layers of the detector, producing characteristic Cu fluorescence X-rays around 8 keV that can subsequently contribute to the signal detected by the GEM [51].
Going back to Fig. 2.11, the configurations of the amplifier and discriminator were kept fixed for both radioactive sources. In particular, I set the shaper to a total amplification of 36, with an integration time of 200 ns and a differentiation time of 20 ns. I set the discriminator width to 200 ns, while I set the threshold to 75 mV.
I selected the discriminator threshold by performing counting measurements in the absence of a radioactive source, starting from the lowest available threshold and progressively increasing its value. This procedure allowed the contribution of electronic noise to be progressively suppressed. The selected threshold value corresponds to a residual counting rate of approximately 1–2 Hz, compatible with the expected contribution from cosmic rays. I estimated this contribution assuming a cosmic-ray flux of $\phi = 1\,\mathrm{cm}^{-2}\mathrm{min}^{-1}$ over the detector surface of 10.4×10.4 cm^2.
I acquired the two counting-rate curves, one for each source, using the HV control program described in Section 2.3.2. The program allows the number of voltage configurations and the corresponding values of I_{eq} to be selected. Once started, it automatically sets and maintains the voltage applied to each HV channel for the time required for the measurement, before changing it according to the selected sequence. This produces a step-like voltage profile as a function of time, such as the one shown in Fig. 2.14a. Each step corresponds to a constant value of the applied voltage. The corresponding counting signal is shown in Fig. 2.14b. For each constant voltage interval, the number of recorded counts remains approximately stable, with fluctuations between individual measurements. These fluctuations are shown in greater detail in Fig. 2.14c. The latter also illustrates the procedure adopted to determine the counting rate associated with each voltage value. For each

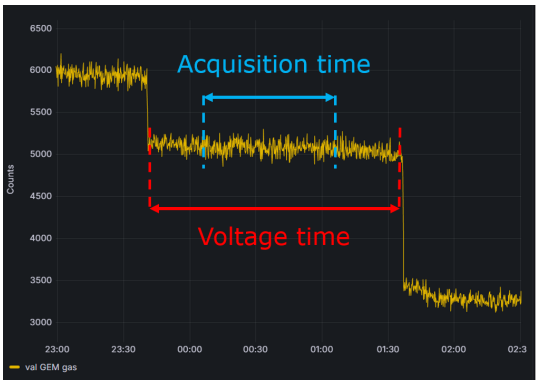
voltage step, I considered only the central portion of the corresponding counting interval for the rate calculation. This acquisition window, indicated as "acquisition time" in Fig. 2.14c, was selected to exclude the initial and final portions of the voltage step and to use the interval in which the counting rate was most stable. The acquisition time was set to half of the total duration of each voltage step. The total voltage-step duration and, consequently, the acquisition time were varied depending on the radioactive source, as described below.



(a) Example of a complete sequence of applied voltages. Each curve corresponds to the voltage applied to a single detector electrode.



(b) Counting data recorded during the voltage sequence shown in Fig. 2.14a.



(c) Zoomed view of a single counting-rate step. The voltage-step duration and the acquisition time used for the rate calculation are indicated.

FIGURE 2.14: Applied high voltage and counting data as a function of time, visualized in Grafana. The red rectangle highlights a single voltage step in the first panel and the corresponding counting-rate step in the second panel.

Each recorded count value corresponds to a counting interval of 10 s. For example, for a voltage-step duration of 2 h, the corresponding acquisition time is 1 h, resulting in 360 individual count measurements.

For each voltage value, the corresponding counting rate was calculated as the mean of the individual rates measured during the acquisition window,

$$R = \frac{1}{n}\sum_{i=1}^{n} R_i, \tag{2.8}$$

where n is the total number of measurements within the acquisition window and R_i is the rate measured in the i-th counting interval. Since each counting interval lasted 10 s,

$$R_i = \frac{\text{counts}_i}{10\,\text{s}}, \tag{2.9}$$

where counts_i is the number of counts recorded during the i-th interval.
The spread of the individual rate measurements around their mean is quantified by their sample standard deviation,

$$\sigma_R = \sqrt{\frac{1}{n-1}\sum_{i=1}^{n}(R_i - R)^2}, \tag{2.10}$$

and is used to assign the error bars to the corresponding rate values.
For the ^{55}Fe source, I selected 30 HV configurations, corresponding to values of I_{eq} ranging from 725 µA to 570 µA. Throughout this work, all voltage sequences were acquired monotonically, proceeding from the highest HV value down to the lowest, without ever reversing direction along the sequence; whenever a scan needed to be repeated, it was always restarted from the highest voltage rather than resumed from an intermediate point. I adopted this convention after observing that increasing the voltage halfway through a descending scan, and then decreasing it again, produced measurements that did not lie on the same curve as the original descent.
For this specific scan, the configurations were not equally spaced in I_{eq}: a higher density of points was used in the voltage region where the counting rate varies more rapidly, in order to better characterize the transition region. Each voltage configuration was maintained for 2 h, resulting in an acquisition time of 1 h for the determination of the corresponding counting rate. The total number of count measurements collected every 10 s to determine a single rate value was therefore 360 ($n = 360$ in Eq. (2.8)).
As the applied voltage is increased, the counting rate initially rises and eventually reaches a plateau, corresponding to the region in which the detector response is stable. This behaviour can be empirically described by a sigmoid function:

$$R(\mathrm{HV}) = \frac{L}{1 + e^{-k(\mathrm{HV}-\mathrm{HV}_0)}}, \tag{2.11}$$

where L is the plateau value, k determines the steepness of the transition, and HV_0 is the voltage at which the rate reaches half of the plateau value, i.e. $R(\mathrm{HV}_0) = L/2$. For the ^{55}Fe measurements, a single sigmoid function was found to be insufficient to adequately describe the observed counting-rate curve. Therefore, the data were fitted using the sum of two sigmoid functions as an empirical model:

$$R(\mathrm{HV}) = \frac{L_1}{1 + e^{-k_1(\mathrm{HV}-\mathrm{HV}_{01})}} + \frac{L_2}{1 + e^{-k_2(\mathrm{HV}-\mathrm{HV}_{02})}}, \tag{2.12}$$

where L_1 and L_2 are the plateau contributions of the two components, while k_1, k_2, HV_{01}, and HV_{02} determine their respective slopes and positions.
I performed the fit in Python using the `curve_fit` function from the SciPy optimization module, with six free parameters: L_1, L_2, k_1, k_2, HV_{01}, and HV_{02}.
All fits presented in this work were performed using the same procedure, based on the `curve_fit` function from the SciPy optimization module.
The result of the fit is shown in Fig. 2.15a. Since the gain calculation in Eq. (2.4) requires the counting rate corresponding to the plateau region, I take the asymptotic value of the fitted function as the particle rate R. For the double-sigmoid function, this value is given by the sum of the two plateau contributions,

$$R_{\mathrm{plateau}} = L_1 + L_2. \tag{2.13}$$

For the ^{55}Fe source, the resulting plateau rate is

$$\boxed{R^{^{55}\mathrm{Fe}}_{\mathrm{plateau}} = (812.73 \pm 3.81)\,\mathrm{Hz}.} \tag{2.14}$$

The uncertainty on R_{plateau} was obtained by propagating the uncertainties of the fitted parameters L_1 and L_2, including their covariance:

$$\sigma_{R_{\mathrm{plateau}}} = \sqrt{\sigma^2_{L_1} + \sigma^2_{L_2} + 2\,\mathrm{cov}(L_1, L_2)}, \tag{2.15}$$

where $\mathrm{cov}(L_1, L_2)$ is obtained from the covariance matrix returned by the fitting procedure.
Moving to the ^{109}Cd source, the measurement and fitting strategies remain the same as those described above. I selected the same 30 HV configurations in the I_{eq} range between 725 µA and 570 µA used for the ^{55}Fe measurements. The voltage-step

duration was instead reduced to 30 min, resulting in an acquisition time of 15 min. Since each individual counting measurement lasted 10 s, this corresponds to 90 measurements for each voltage configuration.
As Fig. 2.15b shows, for the ^{109}Cd source, the counting-rate curve exhibited a different behaviour from that observed for ^{55}Fe. In particular, after an initial increase and an apparent plateau, the counting rate showed a further rise at higher voltages, making the plateau value difficult to identify unambiguously. The first three points at the lowest voltages were excluded from the fit, as they were not adequately described by the sigmoid behaviour observed in the remaining data. Among the fitting models investigated, the double sigmoid function in Eq. (2.12) provided the best description of the data, with a reduced χ^2 close to unity.
The first sigmoid component reaches a plateau of $L_1 = (1195.22 \pm 9.45)$ Hz, whereas the second component is poorly constrained, yielding $L_2 = (464.03 \pm 355.19)$ Hz. The lower plateau, corresponding to the first sigmoid component, is directly supported by the measured data, whereas the second component is only weakly constrained and its asymptotic contribution cannot be reliably determined. Therefore, the first plateau was used as the counting rate R for the subsequent gain calculation:

$$\boxed{R^{^{109}\mathrm{Cd}}_{\mathrm{plateau}} = (1195.22 \pm 9.45)\,\mathrm{Hz}.} \tag{2.16}$$

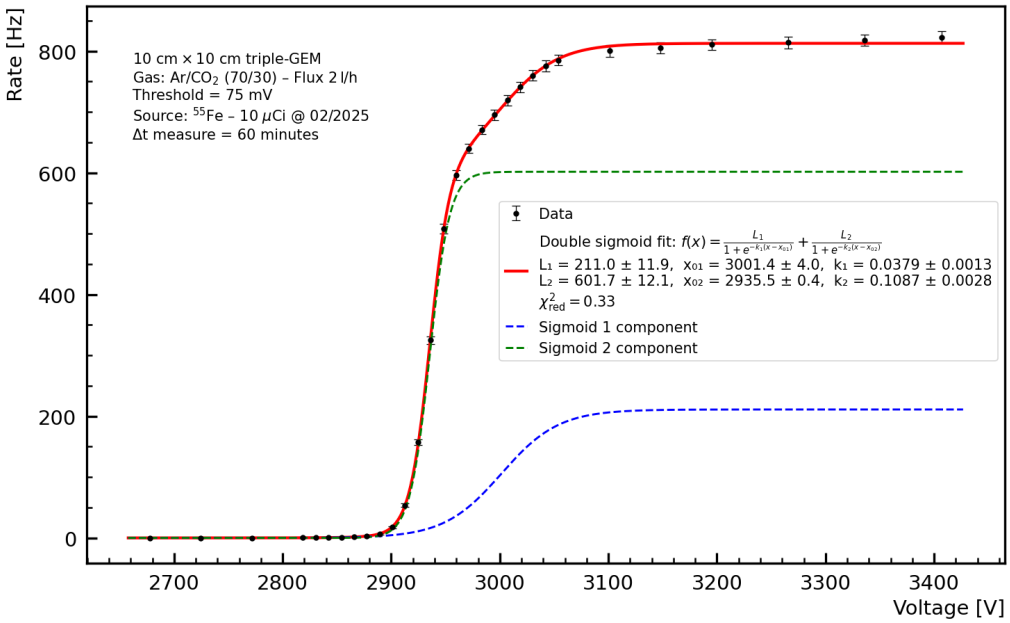
The different behaviours observed for the two radioactive sources indicate that the counting-rate response cannot be described by a single common functional form. These observations motivated the use of the two sources separately in the subsequent gain measurements.

Current measurement

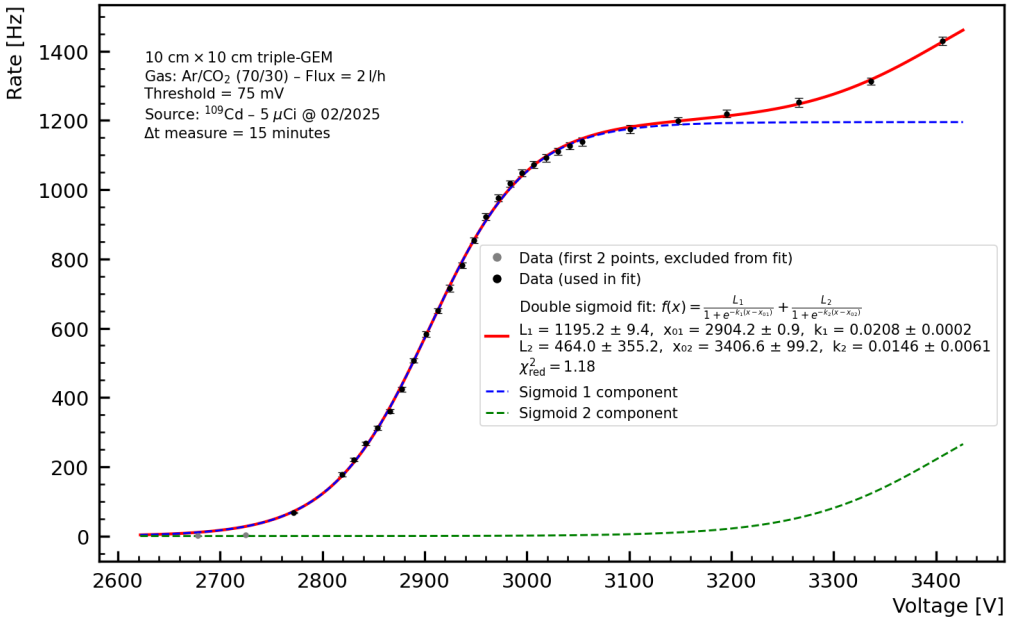
Referring to Fig. 2.11, the current signal collected from the readout strips was measured using the picoammeter, which was controlled remotely from the computer. A Python-based acquisition script was used to configure and perform the measurements. Before starting the acquisition, the script allowed us to set three parameters[1]:

- **Number of Power Line Cycles (NPLC).** The NPLC parameter determines the integration time of a single current reading. For a 50 Hz power-line

[1]Parameters definitions and allowed ranges are detailed in the instrument's user manual [52].



(a) Counting rate as a function of the applied voltage for the ^{55}Fe source.



(b) Counting rate as a function of the applied voltage for the ^{109}Cd source.

FIGURE 2.15: Counting rate as a function of the applied voltage, measured with the two radioactive sources.

frequency, one PLC corresponds to 20 ms. Therefore, the integration time is given by

$$t_{\text{int}} = \text{NPLC} \times 20\,\text{ms}. \tag{2.17}$$

For the measurements presented in this work, NPLC was set to 5, corresponding to an integration time of 100 ms.

- **Buffer size.** This parameter determines the number of individual readings stored by the acquisition program. A buffer size of 100 readings was used.
- **Measurement range.** The measurement range determines the maximum current that can be measured within a given range. It was kept fixed at 20 nA.

These parameters were selected to provide a suitable compromise between acquisition time and measurement precision, following the user's manual specifications [52]. The acquisition program collected the individual current readings and calculated their mean value and standard deviation, providing the measured current together with the spread of the collected readings.
Since the measured current also includes a contribution from the background, the current used in Eq. (2.4) was obtained by subtracting the current measured in the absence of the radioactive source (I_{bkg}) from that measured with the source positioned over the detector's window (I_{src}):

$$I_a = I_{\text{src}} - I_{\text{bkg}}. \tag{2.18}$$

For a selected value of the supply voltage, I consecutively recorded the two current measurements, I_{src} and I_{bkg}, and then computed their difference to obtain I_a.
Considering the independence of the two measurements, I calculated the associated uncertainty as

$$\sigma_{I_a} = \sqrt{\sigma^2_{\text{src}} + \sigma^2_{\text{bkg}}}. \tag{2.19}$$

Each chosen I_{eq} configuration corresponds to a single I_a measurement and, as a consequence of Eq. (2.4), to a single gain point. For both ^{55}Fe and ^{109}Cd sources I have selected 15 I_{eq} configurations in the range between 725 µA and 570 µA, starting from the highest value and proceeding with successive configurations obtained by alternately decreasing I_{eq} by 10 µA and 12.5 µA.

Gain curves

The last quantity required for the gain calculation is the number of primary electrons, n_e, which, according to Eq. (2.5), depends on the photon energy E_γ. Considering the 70/30 Ar/CO_2 gas mixture, I obtain

$$n_e = E_\gamma \left(\frac{0.7}{26} + \frac{0.3}{33}\right) = E_\gamma \times 0.036\,\mathrm{eV}^{-1}. \tag{2.20}$$

Using $E_\gamma = 5.9\,\mathrm{keV}$ for ^{55}Fe and $E_\gamma = 8.0\,\mathrm{keV}$ for ^{109}Cd, I obtain

$$n_e^{^{55}\mathrm{Fe}} = 212.4, \qquad n_e^{^{109}\mathrm{Cd}} = 288.0.$$

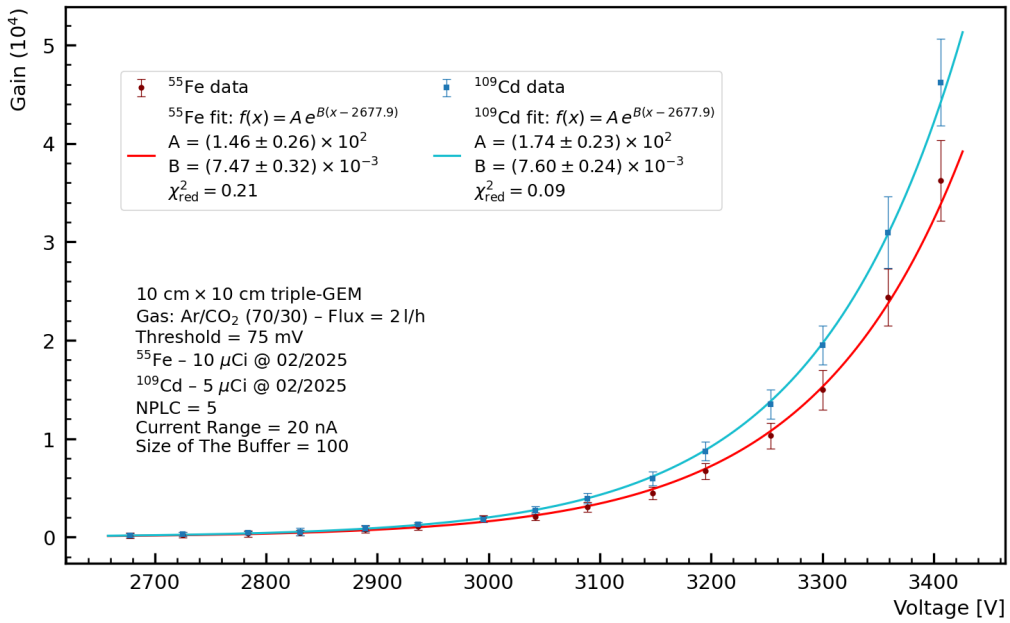
The gain at each voltage point can now be calculated by substituting all the quantities discussed above into Eq. (2.4).
The uncertainty on each gain value is calculated using standard error propagation:

$$\begin{aligned} \sigma_G &= \sqrt{\left(\frac{\partial G}{\partial I_a}\,\sigma_{I_a}\right)^2 + \left(\frac{\partial G}{\partial R}\,\sigma_R\right)^2} \\ &= \frac{1}{e\,n_e\,R}\sqrt{\sigma_{I_a}^2 + \left(\frac{I_a}{R}\right)^2 \sigma_R^2}. \end{aligned} \tag{2.21}$$

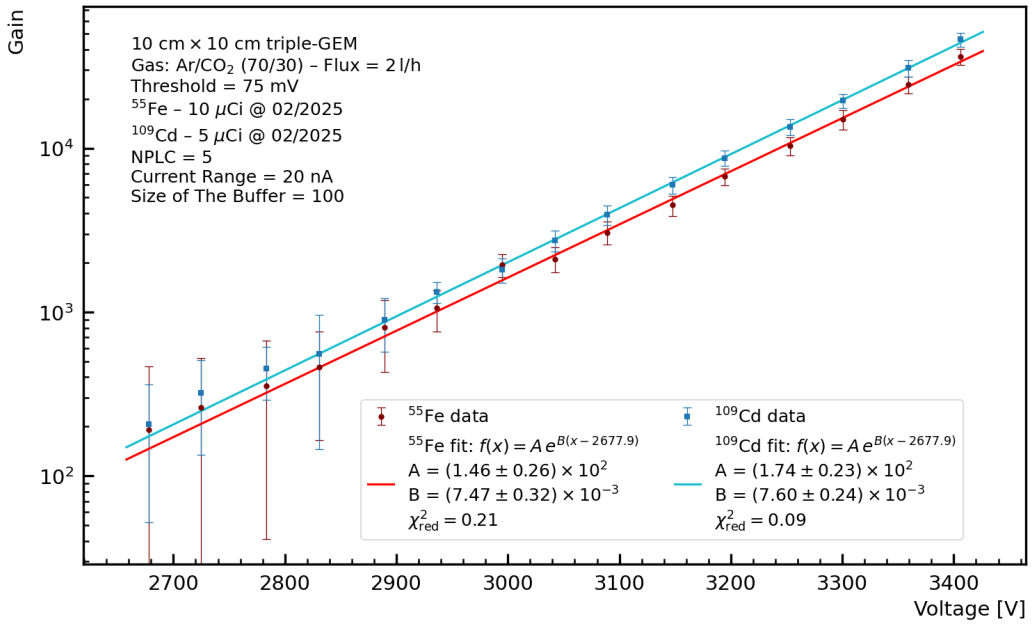
I selected an exponential function to describe the gain dependence on the applied voltage:

$$G(\mathrm{HV}) = A\,e^{B\,(\mathrm{HV} - 2677.9\,\mathrm{V})}, \tag{2.22}$$

where B determines the steepness of the exponential dependence. I have chosen the voltage offset value as 2677.9 V, corresponding to the GEM supply voltage of the lowest I_{eq} configuration (570 µA). With this choice, A directly corresponds to the gain at the lowest voltage point.
The resulting gain curves are shown in Fig. 2.16a. The same curves are shown in Fig. 2.16b with a logarithmic scale on the gain axis, making the exponential dependence on the applied voltage appear linear.
The highest gain value obtained with the 10×10 triple-GEM detector is well above 10^4, in agreement with the typical values mentioned in Section 1.3.3.



(a) Gain as a function of the applied voltage, shown on a linear scale.



(b) Gain as a function of the applied voltage, shown on a logarithmic scale.

FIGURE 2.16: Gain as a function of the applied voltage obtained using the ^{55}Fe and ^{109}Cd sources.

The gain curves obtained with the two sources are compatible within, at most, slightly more than one standard deviation. The good agreement between the two gain curves, obtained from sources with different photon energies, supports the consistency of the gain determination. The small differences observed between the curves may partly originate from the determination of the counting rate R, which relies on the plateau values extracted from the rate–voltage fits. In particular, the different behaviour of the two sources required the use of different plateau regions, introducing a possible systematic contribution to the observed difference.

Gain with the multichannel analyzer

The observation of a double plateau in the ^{55}Fe counting-rate curve as a function of the supply voltage (Fig. 2.15a) motivated us to investigate possible interpretations of this behaviour. Therefore, the pulse-height spectrum produced by the detector was studied using the ORTEC EASY-MCA MultiChannel Analyzer (MCA). The acquisition chain, shown in Fig. 2.17, starts from the signal collected at the G3Bot electrode, which is processed by the preamplifier and the shaper (shaper parameters: total amplification = 36, integration time = 200 ns, differentiation time = 20 ns) before being recorded by the MCA. The MCA is connected to the computer via USB and is operated through the MAESTRO software, which allows the acquisition of the signal spectrum.

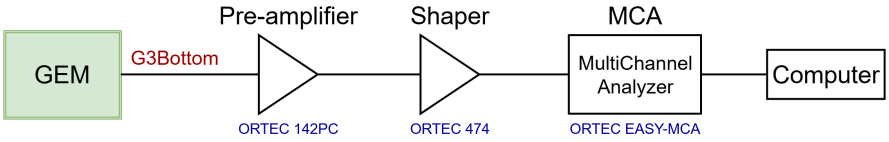


FIGURE 2.17: Schematic representation of the data acquisition chain used for the MCA measurements.

Since the MCA was not calibrated, its output is a histogram of the number of counts as a function of the MCA channel. For each detected pulse, its amplitude determines the corresponding MCA channel, whose content is then increased by one count.
An example of the acquired spectrum is shown in Fig. 2.18. The spectrum was obtained by acquiring signals for 150 s at a fixed supply voltage of 3265.1 V.
Two different peaks can be clearly identified in the spectrum. The peak in the green “Region 2” corresponds to the photopeak produced by the 5.9 keV photons

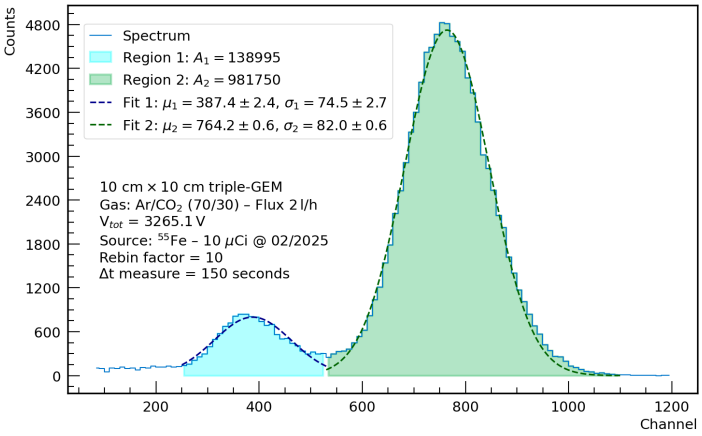


FIGURE 2.18: Histogram of the number of counts as a function of MCA channel for the ^{55}Fe source.

emitted by the ^{55}Fe source, while the peak in the blue "Region 1" is attributed to the Ar escape peak[2].

The two peaks were fitted independently with a Gaussian function of the form

$$f(\mathrm{ch}) = A\, e^{-\frac{(\mathrm{ch}-\mu)^2}{2\sigma^2}}, \tag{2.23}$$

where ch denotes the MCA channel, A is the peak amplitude, μ is the centroid (mean) channel, and σ is the standard deviation of the distribution.

Neither the ratio between the areas under the two peaks (~ 7) nor the ratio between their μ values (~ 2) is consistent with the ratio between the two plateaus of the counting-rate curve (~ 3). Therefore, the comparison does not reveal a correspondence between the two spectral components and the two plateaus observed in the counting-rate curve.

Nevertheless, the MCA spectra provide an independent way of studying the dependence of the detector response on the applied voltage. The spectra acquired at different supply voltages are shown in Fig. 2.19.

In particular, at fixed photon energy and acquisition conditions, the detector gain is proportional to the position of the photopeak in MCA channels, C_{peak}. Therefore, the $C_{\mathrm{peak}}(\mathrm{HV})$ curve can be used as an alternative representation of the gain dependence on the applied voltage.

[2]Ar atoms in the gas mixture can be ionized by the 5.9 keV photons emitted by the ^{55}Fe source and subsequently emit a fluorescence photon with an energy of approximately 3 keV. These photons can escape the detector's active gas volume before being reabsorbed, carrying away part of the energy deposited by the initial interaction.

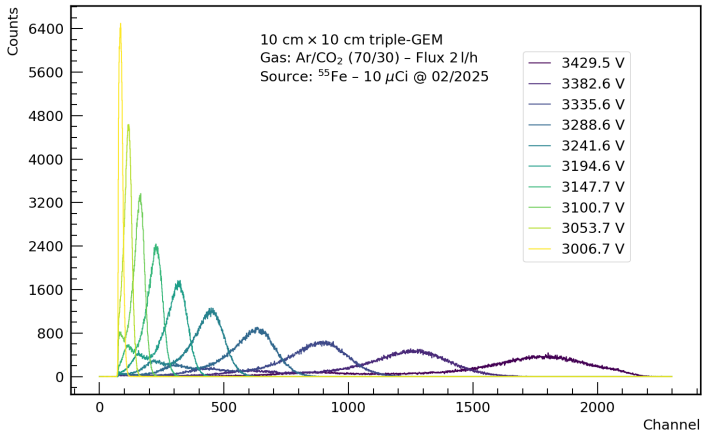


FIGURE 2.19: Histogram of the number of counts as a function of MCA channel for the ^{55}Fe source at different supply voltages.

I selected ten I_{eq} configurations in the range between 730 µA and 640 µA, with steps of 10 µA. For each configuration, the radioactive source was placed at the centre of the GEM window and the spectrum was acquired for 300 s. The photopeak in each recorded spectrum was then fitted using the Gaussian function defined in Eq. (2.23). The peak position, C_{peak}, was obtained from the centroid μ of the Gaussian fit, while its uncertainty was estimated from the standard deviation σ of the fitted Gaussian.

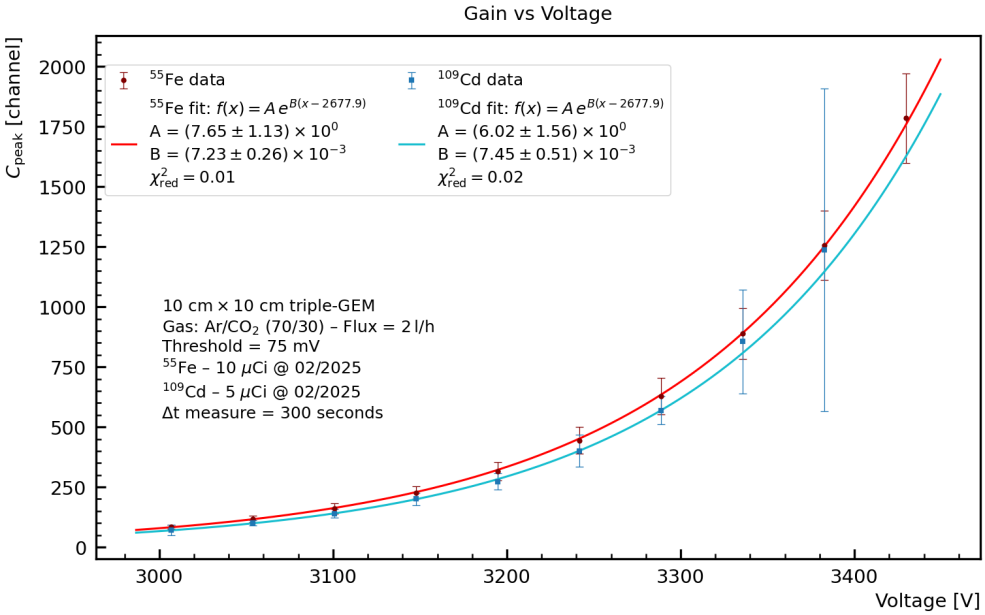
Both the ^{55}Fe and ^{109}Cd sources were employed for this measurement. For the ^{109}Cd source, the highest-voltage point is missing because the photopeak could not be reliably identified.

The resulting curves are shown in Fig. 2.20. The same exponential function defined in Eq. (2.22) was used to fit the data.

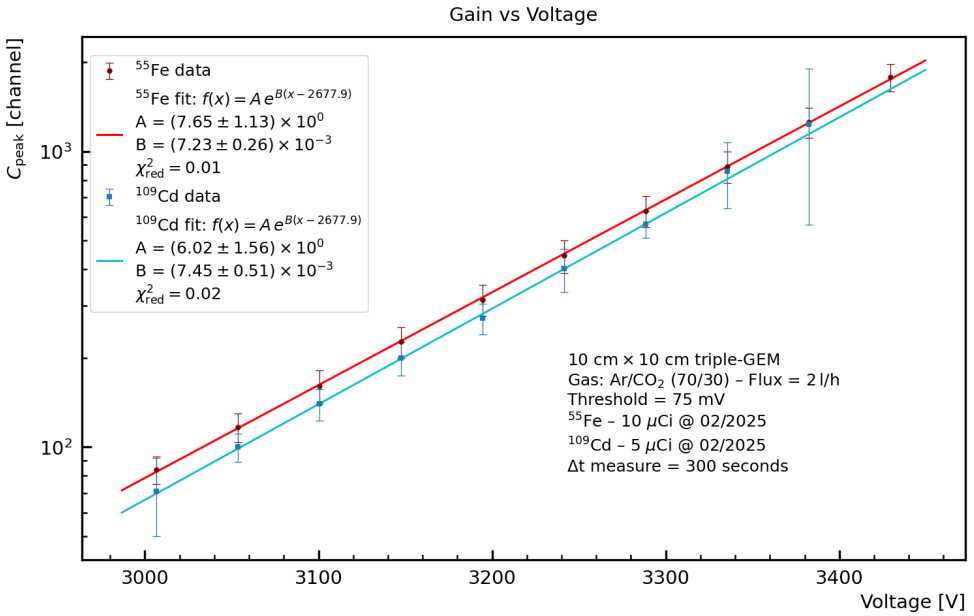
Also with this technique, the curves obtained with the two sources are compatible within one uncertainty.

GEM sensitivity

The counting-rate plateau values obtained in Section 2.5.1 correspond to the event rate measured by the detector. As discussed previously, the main emissions of both the ^{55}Fe and ^{109}Cd sources are photons, while the GEM detector can directly detect only charged particles. Therefore, only a fraction of the photons emitted by the sources can contribute to the measured counting rate. A photon can be detected



(a) Peak position as a function of the applied voltage, shown on a linear scale.



(b) Peak position as a function of the applied voltage, shown on a logarithmic scale.

FIGURE 2.20: Photopeak position as a function of the applied voltage obtained using the ^{55}Fe and ^{109}Cd sources and the MCA.

indirectly if it interacts either in the detector gas or in the detector materials, producing charged particles that subsequently generate a detectable signal.
If R_{plateau} denotes the plateau value obtained from the sigmoid fit and R_{source} denotes the rate of photons emitted by the source, their relation can be expressed as

$$R_{\text{plateau}} = S \times R_{\text{source}}, \tag{2.24}$$

where S is the effective sensitivity of the detector, defined as the probability that a photon emitted by the source ultimately produces a detected event.
The values of R_{plateau} for the ^{55}Fe and ^{109}Cd sources were obtained from the sigmoid fits reported in Eq. (2.14) and Eq. (2.16), respectively. In order to estimate R_{source}, the activity of each source was first calculated using

$$A(t) = A(0)\, e^{-\frac{t}{\tau}}, \tag{2.25}$$

where $A(0)$ is the initial activity of the source, equal to 10 µCi for ^{55}Fe and 5 µCi for ^{109}Cd, and τ is the mean lifetime.
The mean lifetime is related to the half-life $t_{\frac{1}{2}}$ by

$$\tau = \frac{t_{\frac{1}{2}}}{\ln 2}. \tag{2.26}$$

The resulting mean lifetimes are $\tau^{^{55}\text{Fe}} = 3.93$ years and $\tau^{^{109}\text{Cd}} = 1.82$ years, corresponding to half-lives of $t_{\frac{1}{2}}^{^{55}\text{Fe}} = 2.73$ years and $t_{\frac{1}{2}}^{^{109}\text{Cd}} = 1.26$ years, respectively.
The time elapsed between the initial activity measurement and the counting-rate measurements was also taken into account. The corresponding time intervals were $\Delta t^{^{55}\text{Fe}} = 255$ days and $\Delta t^{^{109}\text{Cd}} = 259$ days.
Using Eq. (2.25), the activities at the time of the measurements were found to be

$$A(t_{\text{meas}})^{^{55}\text{Fe}} = 8.38\,\mu\text{Ci} = 3.10 \times 10^5\,\text{Bq},$$
$$A(t_{\text{meas}})^{^{109}\text{Cd}} = 3.38\,\mu\text{Ci} = 1.25 \times 10^5\,\text{Bq}.$$

As a first approximation, these activities were taken as the corresponding source rates, R_{source}, in Eq. (2.24). This approximation assumes that each decay contributes one relevant photon to the source rate and neglects geometrical acceptance and attenuation effects between the source and the detector.

Under this assumption, the effective sensitivities are

$$S^{^{55}\mathrm{Fe}} = (2.62 \pm 0.01) \times 10^{-3}, \qquad S^{^{109}\mathrm{Cd}} = (9.55 \pm 0.08) \times 10^{-3}.$$

The uncertainty on the sensitivity was obtained by propagating the uncertainty on R_{plateau}. Since no uncertainty was specified for the initial activity values reported on the sources, and the passed time was considered exact, the uncertainty on R_{source} was neglected. Starting from Eq. (2.24), the resulting uncertainty is therefore

$$\sigma_S = S\sqrt{\left(\frac{\sigma_{R_{\mathrm{plateau}}}}{R_{\mathrm{plateau}}}\right)^2} = \frac{\sigma_{R_{\mathrm{plateau}}}}{R_{\mathrm{source}}}. \tag{2.27}$$

Rather than a single, source-independent quantity, the effective sensitivity S is expected to depend on photon energy, since the probability of a photon interacting either in the detector gas or in the surrounding materials, and thus of being indirectly detected, is itself energy-dependent. As the ^{55}Fe and ^{109}Cd sources emit photons of different energies, the two effective sensitivities obtained here are correspondingly expected to differ. The factor of about three between them is consistent with this energy dependence, rather than indicating an inconsistency in the estimate.

In addition, using the source activity directly as R_{source} further limits the comparison between the two values: this approximation does not account for the fraction of photons that actually reaches the detector, nor for the probability that a decay produces the photon relevant for the measurement, and neglects the different attenuation probabilities of the two photon energies in the source encapsulation, surrounding materials, and detector structures. For these reasons, the values obtained here should be regarded as source- and energy-dependent effective sensitivities, rather than as a single intrinsic property of the GEM detector.

Nevertheless, both sensitivity values are below 1%, indicating the same order of magnitude for the probability of indirectly detecting photons with a GEM detector. This result is consistent with the general statement introduced in Section 1.3.1, where GEM detectors were described as having low sensitivity to neutral radiation and therefore being generally unsuitable for applications requiring high photon detection efficiency.

2.5.2 Gain uniformity

For the gain measurements presented in the section above, the radioactive sources were always positioned at the centre of the GEM window. However, several factors can affect the gain locally across the GEM surface. Among these are, for example, the non-perfectly uniform tensioning of the GEM foils, local variations in the detector materials, and differences in the gas exchange across the detector due to its geometry.

As the detector area increases, ensuring a uniform response over the whole active surface becomes more challenging. At the same time, a uniform response is important to avoid differences in the detector performance depending on the position at which the ionization occurs.

Since a perfectly uniform response cannot be achieved in practice, it is important to characterize its spatial variation. Knowing how the detector response changes as a function of position allows the non-uniformity to be properly taken into account and, if necessary, corrected for in the analysis. The gain uniformity is therefore an important characterization measurement for GEM detectors.

The acquisition chain for the gain uniformity measurement of the 10×10 triple-GEM is the same as that described in Section 2.5.1. I performed this measurement using only the ^{55}Fe source. I divided the GEM surface into 49 areas using a 7×7 grid, as shown in Fig. 2.21.

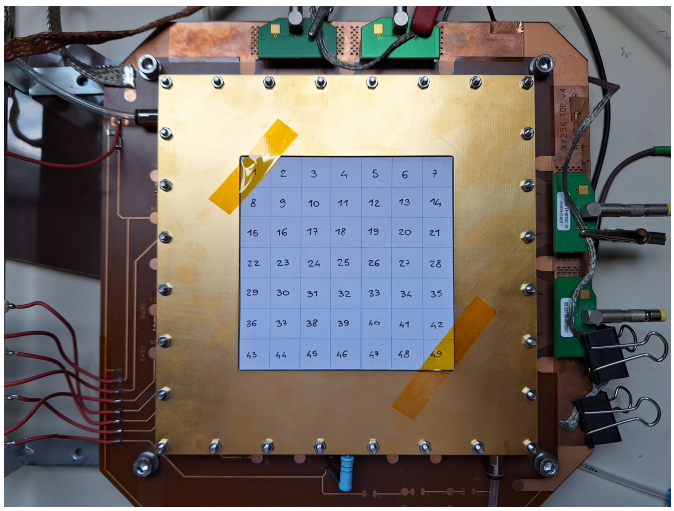


FIGURE 2.21: 10×10 triple-GEM equipped with the 7×7 grid used for the gain uniformity measurement.

I selected a single value of the supply voltage, $V = 3265.1\,\mathrm{V}$, corresponding to $I_{eq} = 695\,\mu\mathrm{A}$, and kept it fixed throughout the measurement in order to maintain the same operating conditions for all positions. For each area, I positioned the source approximately at its centre, acquired the corresponding spectrum using the MAESTRO software, and processed it as described in Section 2.5.1 to obtain the centroid of the Gaussian fit to the photopeak. As in the gain measurement described in the previous section, the MCA was not calibrated, so the resulting centroid values are expressed in channels. Since here the interest is focused on the relative uniformity of the detector response rather than its absolute gain, this calibration is not required.

Once the spectrum of one area was acquired, I moved the source to the centre of the following area. I set the acquisition time to 150 s in order to perform all measurements within a limited time interval and thus minimize possible changes in the environmental conditions that could affect the detector gain.

The result of the gain uniformity measurement is shown in Fig. 2.22. Each value is expressed as a percentage, obtained by normalizing the corresponding centroid to the largest measured centroid and multiplying the result by 100.

The maximum value was obtained in the upper-left region of the detector, corresponding to the position of the gas inlet. Moving approximately along the diagonal towards the lower-right region, in the direction of the gas flow, the measured response gradually decreases, reaching its lowest values close to the gas outlet.

The difference between the maximum and minimum measured values corresponds to a relative variation of approximately 33.6%. The presence of a spatially correlated variation, rather than a purely local fluctuation, suggests that the observed non-uniformity may be related to the gas distribution inside the detector. In particular, the higher response measured close to the gas inlet could be associated with the different gas-flow conditions in this region. The gas velocity is expected to be higher close to the inlet and to decrease as the gas travels through the detector towards the outlet. This behaviour is associated with a variation of the gas pressure along the flow direction, with lower pressure at the inlet and higher pressure towards the outlet. Since the detector performance depends on the gas pressure, as will be shown in Sec. 3.2, this variation may contribute to the observed spatial gradient. The internal geometry of the detector may also influence the local gas flow and the efficiency of gas exchange.

However, the present measurement alone does not allow the gas-flow effect to

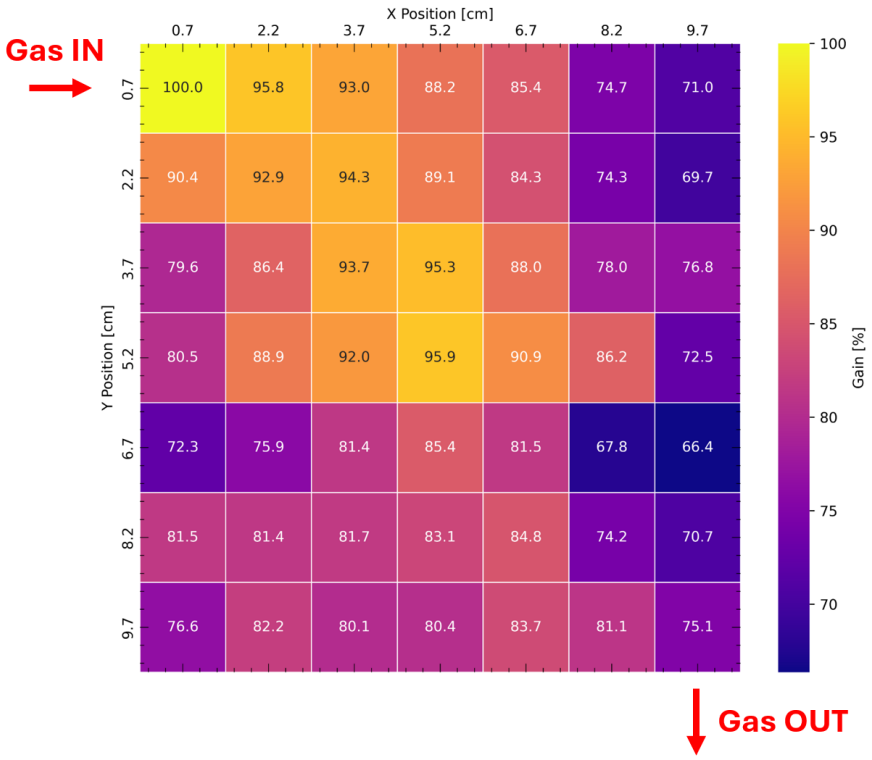


FIGURE 2.22: Relative gain uniformity measured over the 49 sub-areas of the 10×10 triple-GEM.

be unambiguously identified as the origin of the observed gradient. Other local effects, such as geometrical or mechanical non-uniformities, may also contribute to the measured distribution. Nevertheless, the correlation between the measured response and the position along the gas-flow direction supports the hypothesis that the gas distribution plays a role in the spatial uniformity of the detector response.

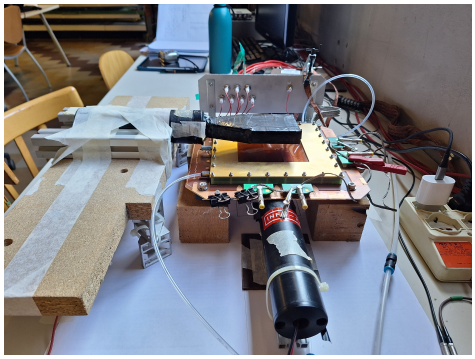
2.5.3 Efficiency

The detection efficiency of a detector is a fundamental characterization parameter. It is defined as the ratio between the number of particles detected by the detector and the number of particles crossing its active area. Ensuring a high detection efficiency is therefore a key requirement for a particle detector.

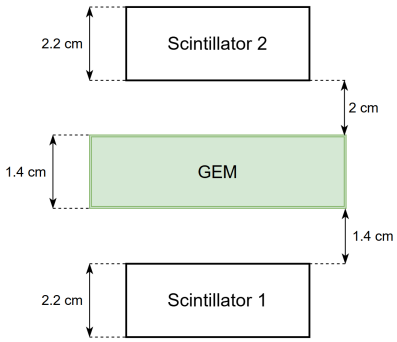
The efficiency of the GEM detector was therefore measured as a function of the applied supply voltage.

In order to perform the efficiency measurements, I modified the experimental setup by adding two polymethyl methacrylate plastic scintillators, each read out by its own photomultiplier tube (PMT). As shown in Figs. 2.23a and 2.23b, the GEM

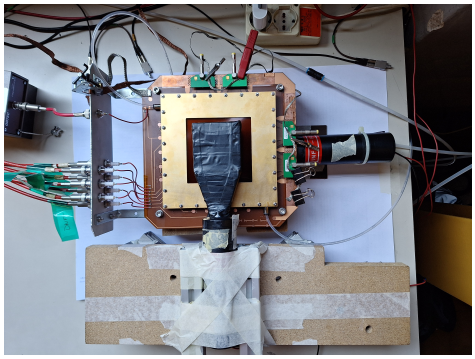
detector was raised to position one scintillator above and the other below it. The scintillators were positioned as close as possible to the triple-GEM in order to maximize the geometrical acceptance of the apparatus. As can be seen from the top views in Figs. 2.23c and 2.23d, the two scintillators have a square shape with a side of 7.4 cm and were placed with their centres aligned with the centre of the GEM window.



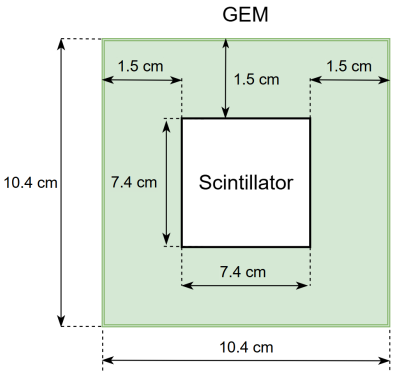
(a) Side view of the experimental setup.



(b) Schematic side view.



(c) Top view of the experimental setup.



(d) Schematic top view.

FIGURE 2.23: Experimental setup used for the efficiency measurement, shown from the side and top views.

The acquisition chain is shown in Fig. 2.24.

Three voltage signals are extracted from the two PMTs and from the G3Bot electrode of the GEM detector. The latter is processed by the preamplifier and the shaper, with the same parameters described in Section 2.5.1: total amplification of 36, integration time of 200 ns, and differentiation time of 20 ns. The three signals are then discriminated using three different channels of the discriminator.

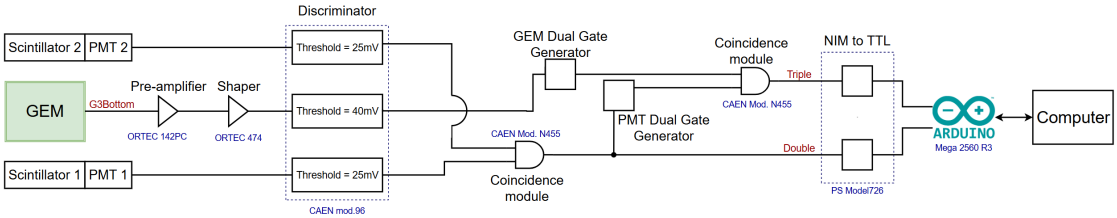
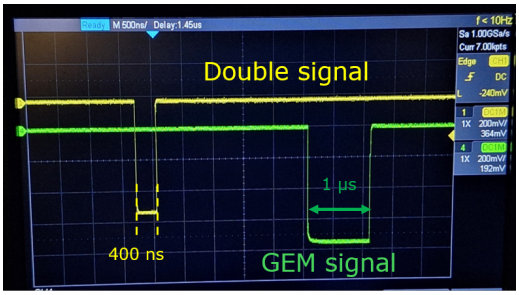
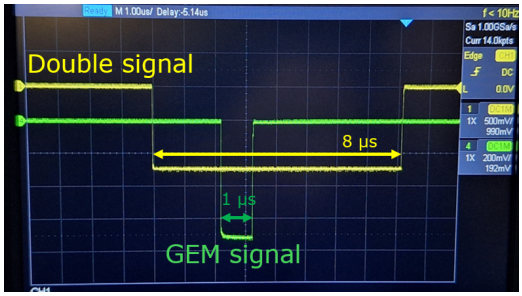


FIGURE 2.24: Schematic representation of the data acquisition chain used for the efficiency measurement.

The two PMT signals are then put in coincidence using the CAEN Mod. N455 quad coincidence logic unit (Fig. 2.9). The resulting double-coincidence signal is split into two branches. One branch is sent to the NIM-to-TTL module and then acquired by the Arduino in order to perform the double-count measurement. The other branch, together with the discriminated G3Bot signal, is sent to two different dual gate generators (Fig. 2.9). The operation of the dual gate generators is illustrated in Fig. 2.25. Before passing through the dual gate generators, the two signals do not overlap in time because they originate from different detectors and are processed by different acquisition chains, as shown in Fig. 2.25a. The dual gate generators are therefore used to stretch and delay the signals, obtaining the configuration shown in Fig. 2.25b, where the GEM signal is fully contained within the double-coincidence signal.



(a) Signals before the two dual gate generators.



(b) Signals after the two dual gate generators.

FIGURE 2.25: Double-coincidence (yellow) and GEM (green) signals visualized using the Teledyne T3DSO1204 oscilloscope.

This signal configuration allows us to obtain, using a second channel of the logic unit, the coincidence between the double-coincidence signal and the GEM signal. The resulting triple-coincidence signal is then converted into a TTL signal and recorded by the Arduino and the computer.

For the efficiency measurements, cosmic rays were used as the source of particles, since their high penetrating power allows them to cross both scintillators and the GEM detector. The efficiency of the GEM detector was determined as the ratio between the number of triple counts recorded in a given time interval, N_3, and the number of double counts recorded in the same time interval, N_2:

$$\epsilon = \frac{N_3}{N_2}. \tag{2.28}$$

The double-coincidence signal identifies events in which a particle crossed both scintillators and therefore provides a reference sample of particles crossing the GEM. Ideally, each of these events should also produce a detectable signal in the GEM. If no GEM signal is recorded for a given double-coincidence event, the event contributes to N_2 but not to N_3, resulting in a reduction of the measured efficiency according to Eq. (2.28).

For this measurement, the discriminator thresholds were set to 25 mV for both PMT signals and to 40 mV for the GEM signal. These values were selected using the trigger function of the oscilloscope. Lower thresholds could be used with respect to the previous measurements because the requirement of a coincidence between the signals intrinsically suppresses the contribution of electrical noise.

In order to provide the high voltage to the two PMTs, a CAEN A1733N board was added to the mainframe. This board allowed us to control the two PMT high-voltage channels through the GECO software (Section 2.3.2). I selected the operating voltage of each PMT by studying the single- and double-coincidence counting rates as a function of the PMT supply voltage. The single counting rate increases with the applied voltage, mainly due to the increasing contribution of random noise. In contrast, the double-coincidence counting rate increases at lower voltages and then reaches a plateau, as shown in Fig. 2.26. The plateau corresponds to the regime in which the coincidence detection efficiency is maximized and remains stable, as the measured double-coincidence rate is determined by the particles crossing the two scintillators. The plateau region was identified by fitting the double-coincidence counting rate with a sigmoid function (Eq. (2.11)). The working point was then selected within this plateau region.

The resulting working points were:

$$\mathrm{HV}^1_{\mathrm{WP}} = 1250\,\mathrm{V}, \qquad \mathrm{HV}^2_{\mathrm{WP}} = 1550\,\mathrm{V},$$

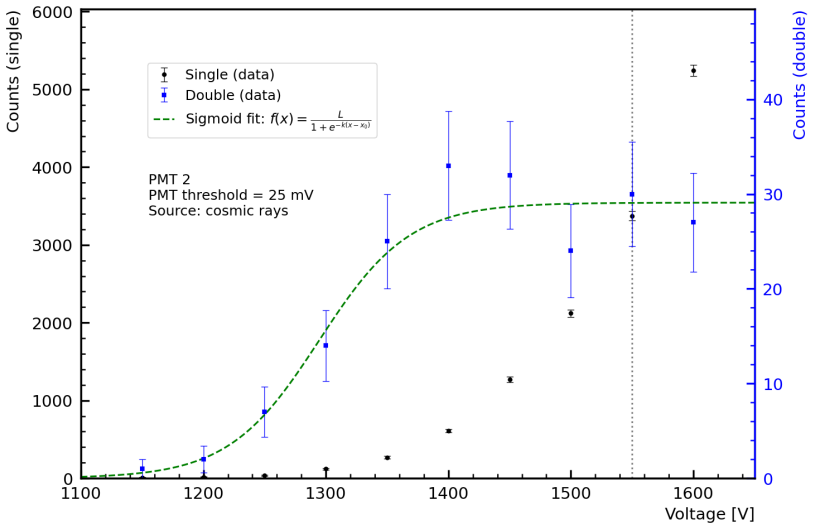


FIGURE 2.26: Single (black) and double (blue) counting rates as a function of the upper PMT supply voltage. The dashed vertical line indicates the selected working point for this PMT (1550 V).

where the superscripts 1 and 2 denote the lower and upper PMT, respectively.
The GEM efficiency measurements were performed using the automatic voltage setting described in Section 2.3.2, the automatic count acquisition described in Section 2.4.1, and the remote monitoring system described in Section 2.4.2. As will be discussed in Chapter 3, the combination of these three elements allowed us to acquire multiple consecutive efficiency curves.
I chose to keep each supply voltage value constant for 1 h. Unlike the rate measurement described in Section 2.5.1, where only the central portion of each voltage step was used as the acquisition window to exclude the initial and final, less stable portions of the step, here the acquisition time for the efficiency measurement was set equal to the full duration of the voltage configuration, with no additional time selection applied within the step. This difference follows from the lower cosmic-ray rate: reaching a statistically significant number of counts required a much longer counting interval, 9 min, compared to the 10 s interval used for the rate measurement.
Data acquisition proceeded continuously, with no interruption or waiting period during the voltage transition between configurations. Six independent, non-overlapping 9 min counting windows were defined within each 1 h voltage step, together spanning 54 min out of the 60 min step duration. This value was deliberately chosen shorter than 10 min — which would have made six consecutive windows span the

full hour exactly — so as to leave an unused margin of about 6 min at the end of each step. Since the exact instant of the voltage transition was not perfectly reproducible, this margin ensured that the transition always fell within the unused interval rather than inside one of the six counting windows, so that no single count measurement ever mixed counts recorded under two different voltage configurations. The counts collected during this margin, while the transition was taking place, were discarded and not used in the efficiency calculation. As a result, six independent count measurements, each fully contained within a stable-voltage 9 min window, were obtained for each voltage value.

For each voltage configuration, a single efficiency value was obtained by averaging the six individual measurements:

$$\epsilon = \frac{1}{6}\sum_{i=1}^{6}\epsilon_i = \frac{1}{6}\sum_{i=1}^{6}\frac{N_{3,i}}{N_{2,i}}. \tag{2.29}$$

The uncertainty associated with each efficiency value was estimated from the standard deviation of the six individual measurements:

$$\sigma_\epsilon = \sqrt{\frac{1}{5}\sum_{i=1}^{6}(\epsilon_i - \epsilon)^2}. \tag{2.30}$$

To obtain the efficiency curve, I selected 16 I_{eq} configurations in the range between 600 µA and 735 µA, with steps of 9 µA.

The resulting efficiency curve is shown in Fig. 2.27. The data were fitted using the sigmoid function defined in Eq. (2.11).

From a physical point of view, the efficiency cannot exceed unity. Therefore, the L parameter of the sigmoid function, which represents the plateau value, was constrained to be at most equal to one. The fit provides a reduced χ^2 of 0.64, indicating a good agreement between the measured data and the sigmoid function.

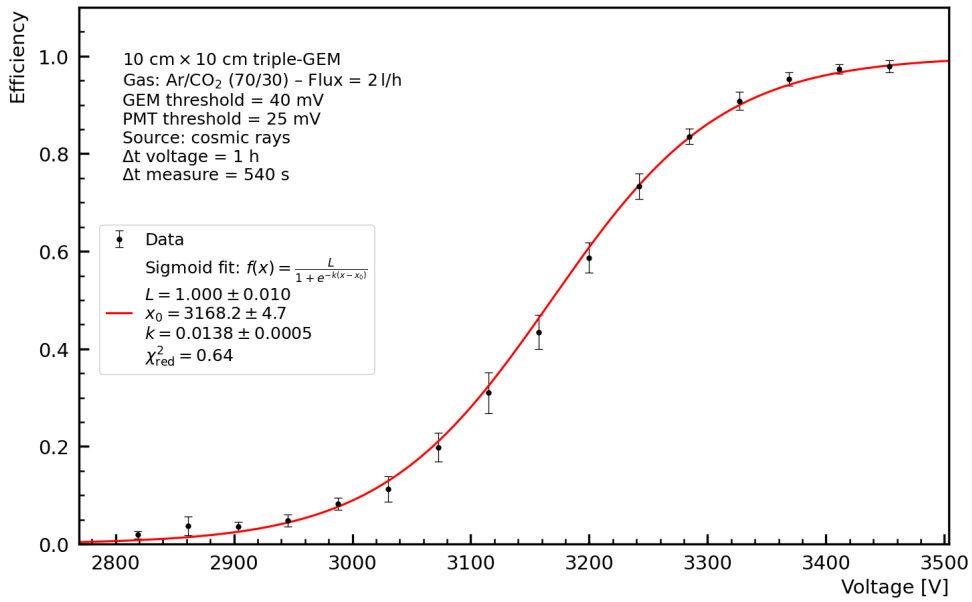


FIGURE 2.27: GEM detector efficiency as a function of the applied voltage.

Chapter 3

Study of short circuits in triple-GEM detectors

This chapter presents the experimental study of the effects of short circuits on the performance of triple-GEM detectors.
Starting from the detector characterization described in the previous chapter, the detection efficiency is used as the main observable to quantify the impact of modified high-voltage (HV) configurations on detector response. The chapter first discusses the correction for pressure and temperature variations and the method adopted to reproduce short-circuit conditions in the laboratory using the 10×10 triple-GEM detector. The effects of voltage reductions applied to individual GEM foils are then investigated, comparing the response of the three foils and extending the study to simultaneous voltage reductions. The corresponding modifications of the electric fields across the gas gaps are also examined. Finally, the HV compensation procedure currently adopted for the GE1/1 chambers is described and related to the individual voltage effects characterized in the laboratory.

3.1 Why detection efficiency: a key performance parameter

The effect of short circuits on the detector performance was investigated by focusing on the detection efficiency. This choice was primarily motivated by the importance of this quantity for the operation of the CMS muon system. As discussed in Chapter 1, efficient muon detection is essential for both muon reconstruction and triggering. In particular, the GE1/1 chambers are designed to achieve a single-chamber detection efficiency above 97%, while the use of two chambers in

a superchamber results in an overall efficiency above 99.9%. A loss of detection efficiency can therefore directly affect the ability of the detector to provide the measurements required for efficient muon reconstruction and triggering.
From an experimental point of view, the detection efficiency provides a direct observable of the detector ability to register particles crossing its active area. This makes it particularly suitable for investigating the consequences of a short circuit: a modification of the high-voltage configuration can alter the electric fields and the amplification conditions inside the detector, potentially affecting the probability of detecting an incoming particle. The resulting change in efficiency can therefore be used as a direct measurement of the impact of the modified operating conditions on detector performance.
The choice was also motivated by practical considerations related to the systematic nature of the study. Efficiency measurements are particularly well suited to automated data taking, since, once the experimental setup and acquisition sequence are configured, they do not require continuous manual intervention.
The automation procedures described in Chapter 2 therefore made it possible to investigate a large number of configurations with minimal manual intervention. Measurements could be carried out during nights and weekends and, more generally, for extended periods of unattended operation. This capability was essential, since the large number of configurations investigated required several months of data taking, interrupted only by occasional technical or unforeseen issues.

3.2 HV correction for pressure and temperature

The operating conditions of gaseous detectors are affected by variations in environmental parameters, in particular pressure and temperature. In GEM detectors, these variations modify the gas density and consequently the amplification conditions for a fixed applied voltage. The dependence of the gas gain on pressure and temperature is well established and is related to the dependence of the Townsend coefficient on the gas density [53]. Although the present study focuses on the detection efficiency rather than the gas gain, variations in the amplification conditions can affect the probability that the signal produced by a traversing particle exceeds the detection threshold, and therefore can result in a variation of the measured efficiency. The pressure and temperature dependence of the detector response must

therefore be taken into account when comparing measurements performed under different environmental conditions [44].
An indication of this effect was observed during a long-term efficiency measurement performed with the 10×10 triple-GEM. Fig. 3.1 shows the evolution of the measured efficiency during an acquisition lasting approximately 68 h. At the beginning of the measurement, the heating system of the laboratory was switched off, and the laboratory was neither opened nor accessed during the acquisition. Since I performed this trial in January, the temperature therefore progressively decreased over the following approximately three days. The detector high-voltage configuration was kept fixed at a total voltage of 3194.6 V, corresponding to an equivalent divider current of $I_{\mathrm{eq}} = 680\,\mu\mathrm{A}$. The measurement was performed in the rising region of the efficiency curve, where the detector response is particularly sensitive to changes in the operating conditions. Over the acquisition, the temperature changed by approximately 10 °C.

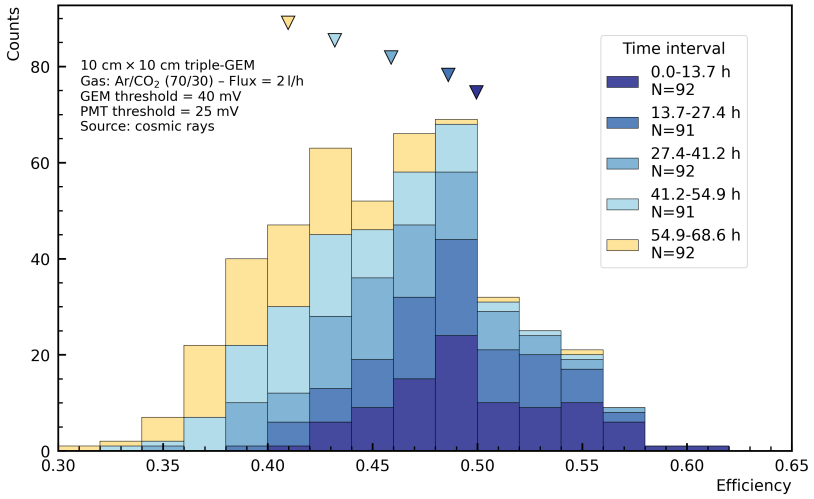


FIGURE 3.1: Time stack plot of the efficiency measurements. The markers indicate the arithmetic mean efficiency of each stack. The vertical position of the markers has no physical meaning and is used only to improve their visual separation.

The data are divided into five consecutive time intervals, represented by the five stacked histograms in Fig. 3.1. For each interval, the marker indicates the arithmetic mean of the efficiency values measured during that period. As the acquisition time increases, the markers progressively shift towards lower efficiency values, indicating a gradual decrease in the measured efficiency. Since the temperature simultaneously decreased during the acquisition, this observation indicates a correlation between

the environmental temperature and the measured detector efficiency under the chosen operating conditions.

This observation does not by itself provide a quantitative dependence of the detection efficiency on temperature. Nevertheless, it demonstrates that variations in the environmental conditions can produce a measurable change in the efficiency even when the applied high-voltage configuration is kept unchanged. Since the measurements presented in this study were collected over several months and under different environmental conditions, a correction is therefore required in order to compare efficiency measurements obtained at different times on a common reference basis.

The correction was applied to the voltage coordinate of the efficiency curves. For each measurement point, the applied voltage was corrected according to the pressure and temperature recorded during the acquisition. Two different correction parametrizations were considered and compared.

As a first approach, a linear correction was adopted, using the dependence of the gas density on pressure and temperature as a simple approximation. The corrected voltage was therefore defined as

$$V_{\mathrm{corr}} = V_{\mathrm{meas}} \frac{P_0}{P} \frac{T}{T_0}, \tag{3.1}$$

where P and T are the pressure and temperature measured during the acquisition, while P_0 and T_0 are the reference pressure and temperature. The values

$$P_0 = 964.4\,\mathrm{mbar}, \qquad T_0 = 297.1\,\mathrm{K} \tag{3.2}$$

were adopted, corresponding to the reference conditions used in the CMS GEM studies [54].

The linear parametrization provides a simple approximation to the pressure and temperature dependence of the detector response. A more general parametrization can be written as

$$G(T,P) = G(T_0,P_0) \left(\frac{P_0}{P}\right)^a \left(\frac{T}{T_0}\right)^b, \tag{3.3}$$

where a and b are empirical parameters.

In a previous study, for a $10\times10\,\mathrm{cm}^2$ triple-GEM detector operated with an Ar/CO_2 (70/30) gas mixture, values of

$$a = 0.398, \qquad b = 0.461 \tag{3.4}$$

were obtained by the CMS GEM group from a fit to measurements of the effective gas gain as a function of pressure and temperature [51]. These values are close to each other, suggesting that the pressure and temperature dependence can be approximated using a common exponent. In CMS GEM studies, the following empirical correction is adopted:

$$I_{\mathrm{divider}}^{\mathrm{corr}} = I_{\mathrm{divider}} \left[\left(\frac{P_0}{P} \right) \left(\frac{T}{T_0} \right) \right]^{0.43}, \tag{3.5}$$

with P_0 and T_0 given in Eq. (3.2) [54].
Since the equivalent divider current and the applied voltage are related through the fixed resistance of the detector's resistive divider (Eq. (2.1)), the same correction can be expressed directly in terms of the applied voltage:

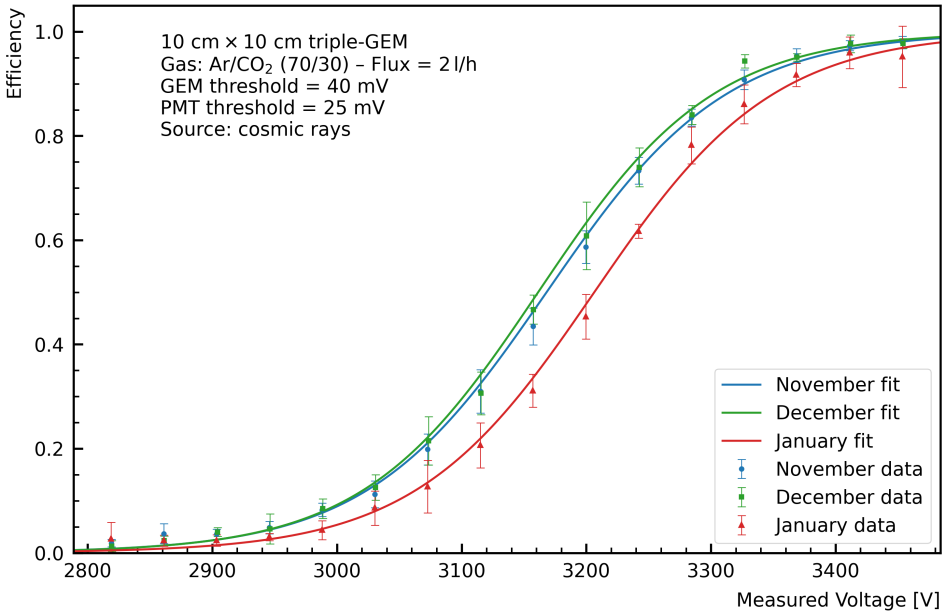
$$V_{\mathrm{corr}} = V_{\mathrm{meas}} \left[\left(\frac{P_0}{P} \right) \left(\frac{T}{T_0} \right) \right]^{0.43}. \tag{3.6}$$

The exponent 0.43 is therefore an empirical parametrization of the pressure and temperature dependence of the GEM response, rather than a fundamental constant. For each stable high-voltage interval, the efficiency was calculated as the arithmetic mean of the individual efficiency measurements within the interval (Eq. (2.29)). The pressure and temperature correction was instead applied to each voltage measurement separately. The corrected voltage associated with the interval was then obtained as the arithmetic mean of the corrected voltages. Each point of the corrected efficiency curve therefore corresponds to a pair $(\overline{V}_{\mathrm{corr}}, \bar{\varepsilon})$, where the efficiency is unchanged with respect to the uncorrected curve and only its associated voltage coordinate is modified. The same procedure was applied independently to the two correction parametrizations illustrated in Eqs. (3.1) and (3.6). The resulting points were then used as input to the sigmoid fit (Eq. (2.11)).
Using the same procedure described in Section 2.5.3, the efficiency measurements were repeated in three different months: November, December, and January.
The uncorrected curves, shown in Fig. 3.2a, show a different detector response for the three measurement periods. In particular, the January measurement exhibits lower

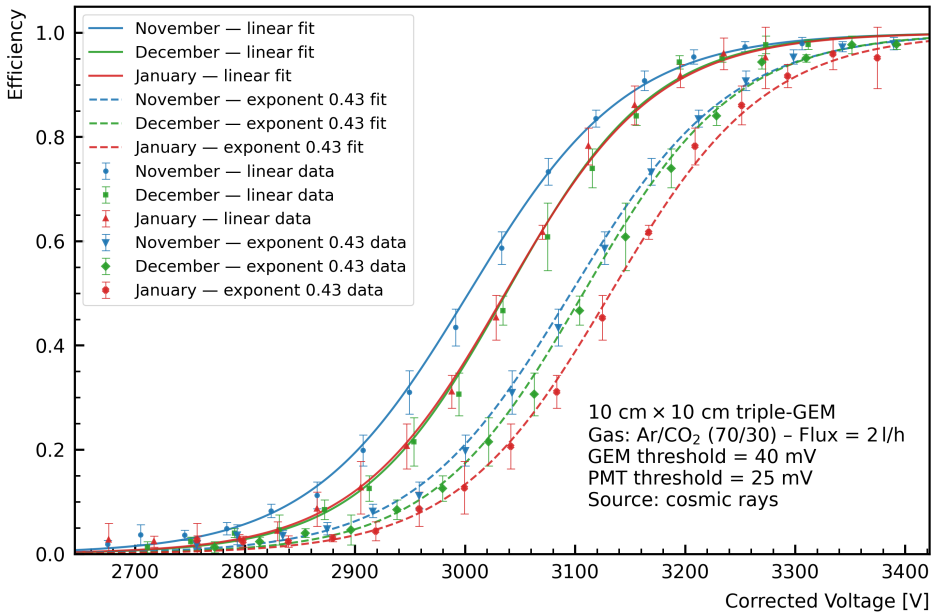
efficiency values in the rising region of the curve, despite being performed at the same applied voltage configurations as the November and December measurements. This indicates that the detector response at a given applied voltage depends on the environmental conditions, and therefore that the same applied voltage does not necessarily correspond to the same effective operating conditions of the detector. After applying the corrections (Fig. 3.2b), the relative position of the three curves changes. However, neither parametrization produces a complete overlap of the measurements. In particular, the correction that improves the agreement for one pair of curves does not necessarily provide the same improvement for another pair. To further investigate the effect of the correction, the exponent in Eq. (3.6) was varied between zero and one. The aim was to determine whether a single exponent could provide a consistent improvement in the agreement between measurements performed at different times. No unique value was found: the exponent providing the closest agreement depended on the specific pair of efficiency curves considered. Therefore, determining the exponent uniquely from the present measurements would result in a parametrization that is dependent on the selected dataset.
For the analysis presented in the following sections, the exponent 0.43 was therefore adopted. This choice follows the empirical parametrization used in CMS GEM studies [54], rather than an optimization performed on the present dataset. The correction should consequently be regarded as a common reference prescription for the measurements, rather than as a procedure that completely removes the effects of variations in the environmental conditions.
The comparison between the raw and corrected efficiency curves obtained using the selected correction (Eq. (3.6)) is shown in Fig. 3.3. In this figure, and in the following analysis, unless explicitly specified, the reference efficiency curve is the same one already presented in Fig. 2.27, corresponding to the November measurement. For this curve, the overall effect of the correction is a shift of the corrected curve towards lower voltage values.
All efficiency plots reported in the following sections are therefore obtained using the selected pressure and temperature correction for the voltage, reported in Eq. (3.6).

3.3 Mocking of short circuits

As described in Section 2.1, the GEM foils of the 10×10 detector do not feature the HV sectorization present in the GE1/1 chambers. A short circuit affecting a



(a) Efficiency curves, without voltage correction.



(b) Comparison between the two different voltage corrections for the three efficiency curves.

FIGURE 3.2: November, December, and January efficiency curves before and after the voltage corrections.

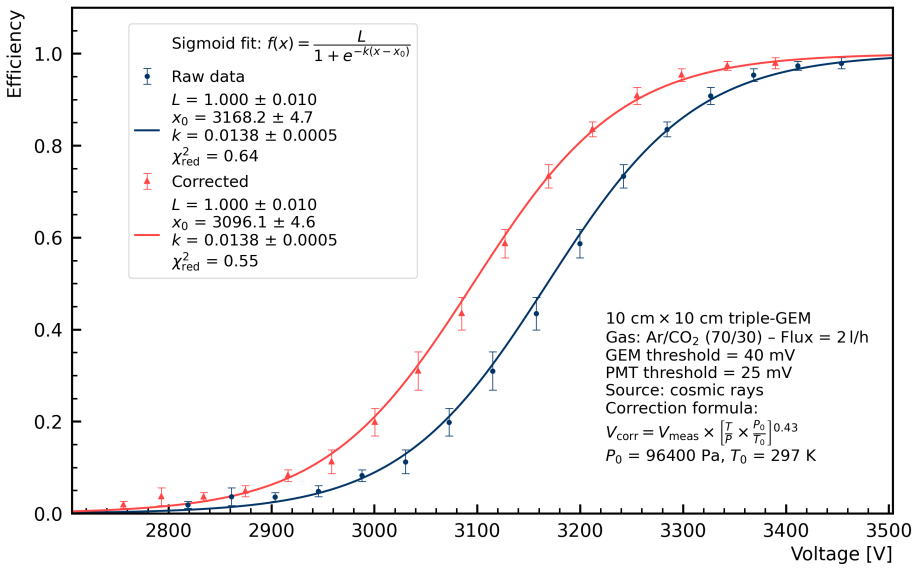


FIGURE 3.3: Comparison between the raw data efficiency curve (without correction) and the efficiency curve obtained after applying the voltage correction of Eq. (3.6).

single HV sector can therefore not be reproduced directly. In GE1/1, the main consequence of a short circuit on the rest of the foil, as shown in Section 1.4.2, is a reduction of the voltage across the healthy sectors: the current flowing through the shorted sector produces a voltage drop in the HV distribution network, so that only a fraction of the nominal voltage is available for charge amplification. In the 10×10 detector, whose foils are not segmented, the whole foil behaves as a set of healthy sectors. This situation can thus be reproduced by directly reducing the voltage applied to the corresponding top channel by an equivalent percentage, as schematized in Fig. 3.4.

The terminology used for the different HV channels and their corresponding voltage differences was introduced in Section 2.3.2. In the following, the names of the HV channels are used to refer to the corresponding voltage differences in the detector. For example, a reduction of the *G1Top* voltage denotes a reduction of the voltage across the first GEM foil, i.e. the potential difference between its top and bottom electrodes (which are the two faces of the foil). Similarly, the *G1Bot*, *G2Bot*, and *G3Bot* channels refer to the voltage differences across the first transfer, second transfer, and induction gaps, respectively.

For the 10×10 detector, the voltage set on a given HV channel directly corresponds to the physical voltage difference between the associated electrodes. This is not

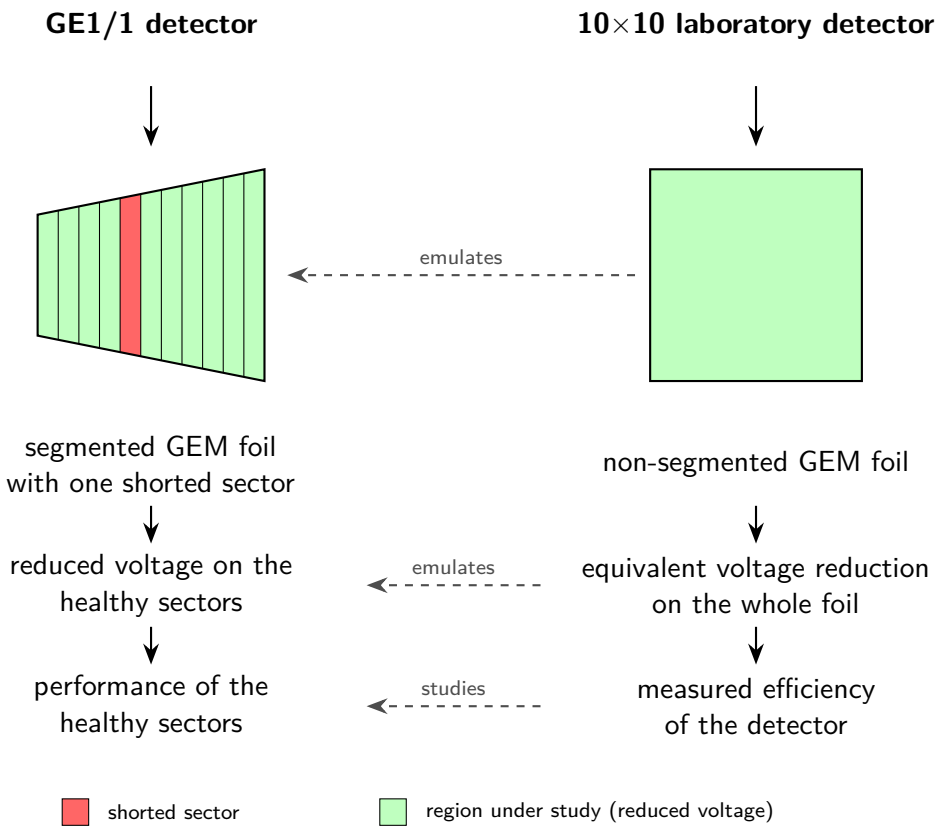


FIGURE 3.4: Correspondence between the study of the healthy sectors of a segmented GE1/1 foil affected by a short circuit and the study performed on the non-segmented 10×10 detector. The voltage reduction experienced by the healthy sectors (green) is emulated by an equivalent voltage reduction applied to the whole laboratory foil. The number and shape of the sectors are purely illustrative.

necessarily the case for a GE1/1 chamber in the presence of a short circuit. In that case, the voltage supplied by the power supply, denoted as V_{top}, differs from the voltage physically present across the healthy sectors of the affected foil, denoted as $V_{\text{top}}^{\text{phys}}$, due to the voltage drop in the HV distribution network caused by the current flowing through the shorted sector. Therefore, the voltage reduction applied to the 10×10 detector in the present study is intended to reproduce directly the physical voltage reduction experienced by the healthy sectors of a GE1/1 foil affected by a short circuit.

A relationship between the number of shorted HV sectors on a GE1/1 GEM foil and the corresponding percentage reduction of the voltage across the healthy sectors can be derived from the resistive network introduced in Section 1.4.2. The percentage

voltage reduction is defined as

$$V_{\text{loss}}^{\%} = \frac{V_{\text{drop}}}{V_{\text{top}}}, \tag{3.7}$$

where V_{top} is the voltage setting of the power supply and V_{drop} is the voltage drop produced by the short circuit. The latter is given by

$$V_{\text{drop}} = V_{\text{top}} - V_{\text{top}}^{\text{phys}}, \tag{3.8}$$

where $V_{\text{top}}^{\text{phys}}$ is the voltage remaining across the healthy GEM sectors after the short circuit. As defined in Eq. (1.7), $V_{\text{top}}^{\text{phys}} \equiv \Delta V_C$.

The value of $V_{\text{loss}}^{\%}$ obtained from the GE1/1 resistive network is then used to reproduce the same effect in the 10×10 detector. In particular, for a given number of shorted sectors, the corresponding percentage reduction is directly applied to the voltage set on the relevant HV channel of the 10×10 detector. In this way, the voltage physically present across the GEM foil in the 10×10 detector is reduced by the same fraction as the voltage across the healthy sectors of a GE1/1 foil affected by the same number of short circuits.

The voltage drop can be calculated from the voltage-divider relation in Eq. (1.6):

$$V_{\text{drop}} = V_{\text{top}} \left(\frac{R_f^{\text{top}} + R_f^{\text{bot}}}{R_f^{\text{top}} + R_f^{\text{bot}} + R_{p,\text{eq}}^{s}} \right), \tag{3.9}$$

where $R_{p,\text{eq}}^{s}$ is the equivalent protection resistance of the shorted sectors, given by Eq. (1.9). It represents the total protection resistance through which the current associated with the short circuit flows.

Substituting Eq. (3.9) into Eq. (3.7), the percentage voltage reduction becomes

$$V_{\text{loss}}^{\%} = \frac{R_f^{\text{top}} + R_f^{\text{bot}}}{R_f^{\text{top}} + R_f^{\text{bot}} + R_{p,\text{eq}}^{s}}. \tag{3.10}$$

If n HV sectors are affected by short circuits, their protection resistors are connected in parallel. Therefore, according to Eq. (1.9),

$$R_{p,\text{eq}}^{s} = \frac{R_p^{s}}{n}, \tag{3.11}$$

where R_p^s is the protection resistance of a single sector. The voltage reduction can consequently be expressed as a function of the number of shorted sectors:

$$V_{\text{loss}}^{\%} = \frac{R_f^{\text{top}} + R_f^{\text{bot}}}{R_f^{\text{top}} + R_f^{\text{bot}} + \dfrac{R_p^s}{n}}. \tag{3.12}$$

Figure 3.5 shows the dependence described by Eq. (3.12). The plot relates the number of shorted HV sectors on a GEM foil (n) to the corresponding percentage reduction of the voltage applied to the top channel. The values of the resistances used to obtain the curve are reported in the legend and correspond to those introduced in Section 1.4.2.

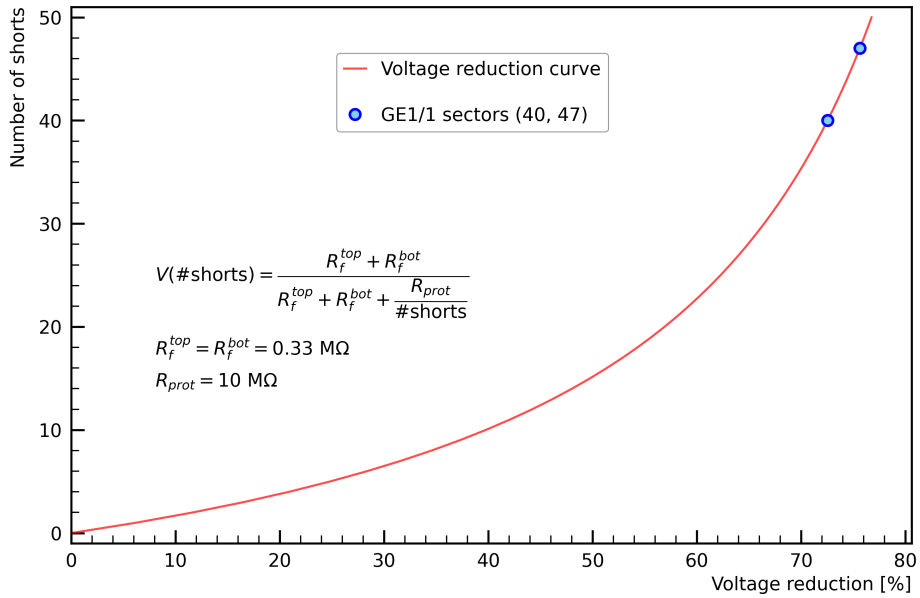


FIGURE 3.5: Number of shorted HV sectors as a function of the percentage reduction of the voltage applied across the GEM foil, calculated according to Eq. (3.12).

For a small number of shorted sectors, the dependence is approximately linear, while the number of shorted sectors increases more rapidly for larger voltage reductions. This behaviour results from the inverse dependence of the equivalent protection resistance on the number of shorted sectors.

The two blue points in Fig. 3.5 correspond to the maximum number of shorted sectors, namely the total number of HV sectors present on the top foil of the GE1/1 Short and Long chambers. These numbers are 40 and 47, respectively. Interestingly,

the corresponding voltage reductions are between approximately 70% and 80%, rather than 100%. This is a consequence of the resistive network: even when all HV sectors are shorted, part of the applied voltage is still dropped across the resistive elements of the network. However, the voltage remaining across the GEM foil itself is zero, so no electric field is established across the GEM holes and electron multiplication can no longer take place.
For the measurements presented in this thesis, the percentage voltage reduction was therefore chosen as the experimental parameter rather than the number of shorted sectors. This allows different degrees of degradation to be reproduced directly on the 10×10 triple-GEM, despite the absence of segmented HV sectors. The specific voltage reductions used for each measurement are reported in the corresponding sections. Typically, the reduction was varied in steps of 5%, with values ranging from 5% to 30%, although the specific values and range were adapted to the requirements of each measurement.

3.4 Voltage reductions across a single foil

As discussed in Section 1.4.2, a short circuit produces two main effects on the detector operation. The first one, described by Eqs. (1.6), (1.7), and (1.8), is a reduction of the voltage across the affected GEM foil, and consequently of the electric field available for charge multiplication. In a real short-circuit condition, this reduction is not caused by a change in the voltage set by the high-voltage power supply, but results from the current flowing through the shorted branch, which modifies the voltage distribution within the HV network. In the present experiment, this effect was instead mocked by directly reducing the voltage applied to the corresponding top HV supply channel.
Since this section focuses on the primary effect of short circuit presence on a single GEM foil, each foil was studied separately by reducing the voltage of one top channel at a time, while keeping the voltages of the other two top channels at their nominal values. Throughout this chapter, the *nominal configuration* associated with a given equivalent current I_{eq} is the set of seven channel voltages $\Delta V_i = R_i I_{\mathrm{eq}}$ (Eq. (2.1)), which respects the voltage ratios of the reference divider of Fig. 2.6. An example for $I_{\mathrm{eq}} = 700\,\mu\mathrm{A}$ is given in Table 2.1. The nominal efficiency curve is the one measured by varying I_{eq} along this family of configurations.

The three cases corresponding to G1Top, G2Top, and G3Top are presented in the following subsections. For each foil, different voltage reductions were investigated, followed by a comparison of the detector response to the same voltage reduction applied to the three different foils.

3.4.1 G1Top

The first foil studied was GEM1, focusing on voltage reductions applied to the G1Top channel.
For each measurement, the G1Top voltage was set to a fixed fraction of its nominal value throughout the entire scan, i.e. $V_{\mathrm{G1Top}} = (1 - V_{\mathrm{loss}}^{\%})\, R_{\mathrm{G1Top}}\, I_{\mathrm{eq}}$, while the other six channels were set to their nominal values $R_i I_{\mathrm{eq}}$ at each point of the scan. The corresponding efficiency curve was then measured by varying I_{eq}. The value of I_{eq} used to label each point therefore refers to the unreduced configuration, and not to the one actually applied.
The first point of each curve corresponds to the nominal configuration, with an equivalent current of 735 µA. The subsequent HV points were obtained by decreasing the equivalent current in steps of 9 µA. The lower end of each scan was not fixed a priori, but was determined by the behaviour of the corresponding efficiency curve. In particular, once the efficiency had reached values close to zero, additional points were not considered necessary.
For each curve, the acquisition time was kept constant for all HV points, but could differ between different curves. This choice was driven by the available statistics in terms of triple-coincidence counts. At lower efficiencies, the number of triple coincidences decreases, and a longer acquisition time is therefore required to obtain sufficient statistics. Since the acquisition time of a single measurement is fixed to 9 min, as described in Section 2.5.3, increasing the total acquisition time results in a larger number of measurements, and this contributes to the mean efficiency value calculated according to Eq. (2.29).
The voltage reductions, number of HV points, and acquisition time per point that I chose for the G1Top channel were the following:

- **5%, 10%**: 16 HV points of 1 h each.
- **15%, 20%**: 16 HV points of 2 h each.
- **25%**: 12 HV points of 1.5 h each.

- **30%**: 11 HV points of 2 h each.

The resulting six efficiency curves are shown in Fig. 3.6. For comparison, the efficiency curve obtained at the nominal HV configuration in Section 2.5.3 is also reported, providing a reference for the effect of the G1Top voltage reduction.

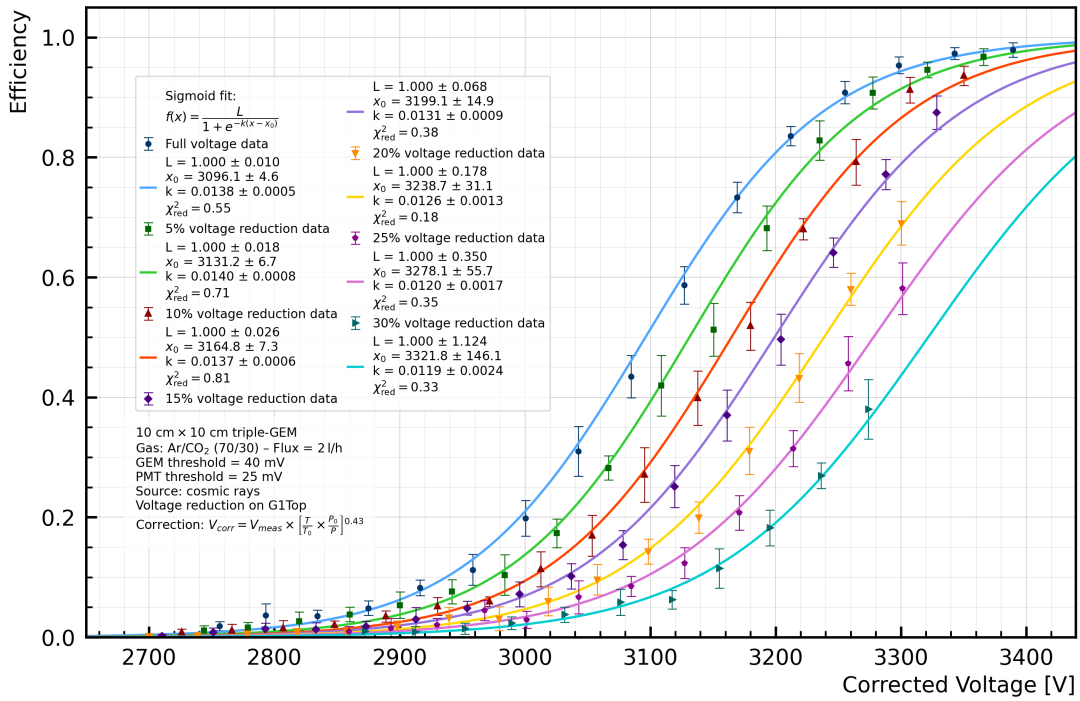


FIGURE 3.6: Efficiency curves as a function of the HV configuration for different voltage reductions applied to the G1Top channel, ranging from 5% to 30%. The nominal-HV efficiency curve is also shown as a reference.

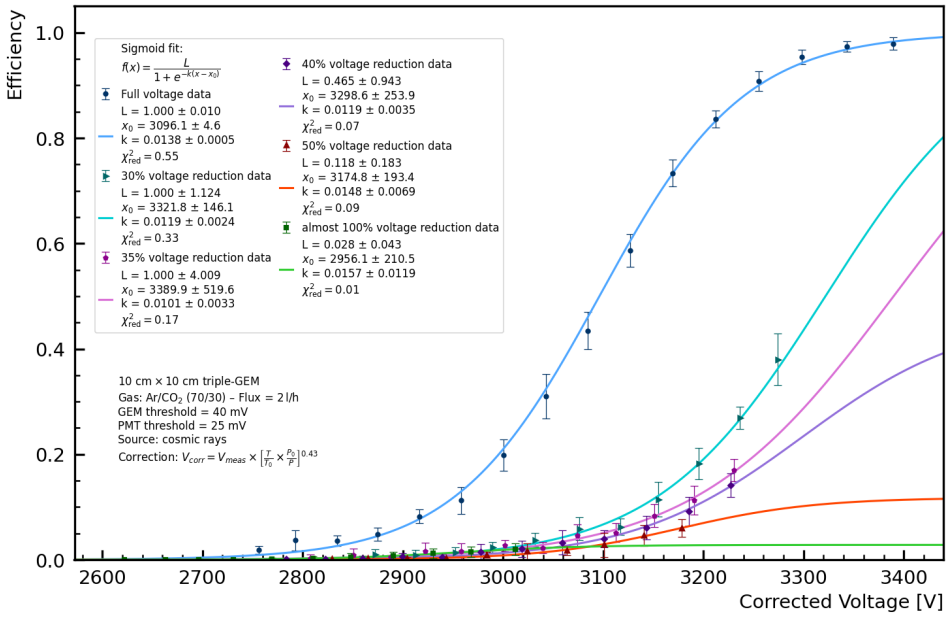
The seven efficiency curves are clearly separated from each other, with the curves corresponding to larger voltage reductions shifted towards lower efficiency values. This behaviour is consistent with the expected effect of reducing the voltage across GEM1, which decreases the electric field available for charge multiplication. As the voltage reduction increases, the point corresponding to the highest total applied voltage also shifts towards lower voltage values. This is a direct consequence of the procedure adopted for the scan: the voltages of the other six channels are kept unchanged, while the G1Top voltage is reduced by different amounts in the different scans. Therefore, the total voltage, obtained as the sum of the channel voltages, is lower for larger reductions.

It is worth noting that the points at the highest voltage of the different curves do not correspond to the same total applied voltage, but to the same nominal equivalent current, $I_{\text{eq}} = 735\,\mu\text{A}$. In particular, the highest-voltage point of the -30% curve is already the point corresponding to the maximum-voltage configuration used for that scan. The lower total voltage with respect to the nominal curve is therefore a direct consequence of the applied G1Top reduction, rather than an indication that a higher-voltage point should have been included.
The evolution of the fitted plateau values provides another indication of the effect of the voltage reduction. In all cases, the fitted plateau parameter reaches the upper limit allowed in the fit, $L \leq 1$. It should be noted that the value $L = 1$ was not imposed in the fit; rather, the fit converges to this value within the imposed upper bound. The corresponding uncertainties increase progressively with the voltage reduction, from approximately 0.01 for the nominal curve to 1.12 for the 30% reduction. This behaviour is expected because, as the voltage reduction increases, the highest-voltage point of the corresponding curve moves to lower efficiency values. The plateau is therefore increasingly determined by an extrapolation of the fitted sigmoid beyond the measured region, resulting in a larger uncertainty on the fitted plateau value.
For the curves with the largest voltage reductions, the increasingly large extrapolation also means that other functional forms could provide alternative descriptions of the data. Nevertheless, for consistency, the same sigmoid function was used for all the curves. The resulting reduced χ^2 values are 0.55, 0.71, 0.81, 0.38, 0.18, 0.35, and 0.33, respectively, and do not show an evident dependence on the applied voltage reduction. This indicates that the chosen function provides a compatible description of the measured efficiency curves over the investigated range.

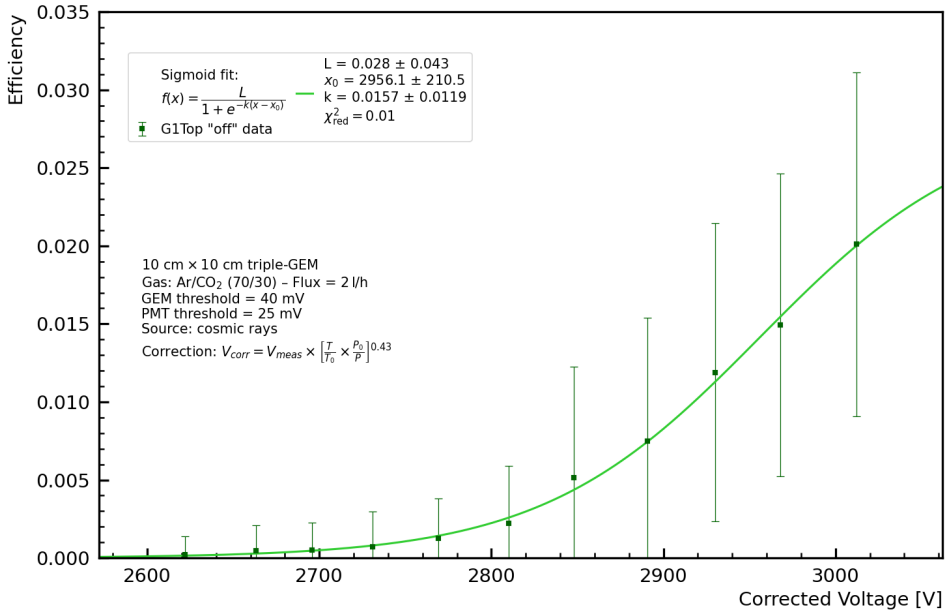
Large voltage reductions

After studying voltage reductions up to 30%, the investigation was extended to larger reductions of the G1Top voltage, namely 35%, 40%, and 50%. For each of these configurations, the efficiency curve was measured using 10 HV points. As for the previous measurements, the first point corresponded to the maximum-voltage configuration, with an equivalent current of 735 µA, while the subsequent points were obtained by decreasing the equivalent current in steps of 9 µA. Each point was acquired for 2 h in order to collect sufficient statistics also at the lower efficiencies reached for these larger voltage reductions.

The resulting efficiency curves are shown in Fig. 3.7a, together with the full voltage curve and the previously shown -30% curve, in order to compare these results with those previously discussed.
As already observed for the smaller voltage reductions, increasing the reduction applied to the G1Top voltage results in a progressive shift of the curves towards lower efficiency values. The three curves corresponding to 35%, 40%, and 50% reductions are therefore located below the curves obtained for smaller reductions over the investigated voltage range.
The fitted plateau values also show a significant change with respect to the smaller reductions. For the -35% curve, the fit gives a plateau value of $L = 1.000 \pm 4.009$. Although the central value reaches the upper limit imposed in the fit, the uncertainty is very large, making the fitted plateau essentially unconstrained. This uncertainty is substantially larger than that obtained for the -30% curve, for which the fitted value was $L = 1.000 \pm 1.124$. The increase in the uncertainty is consistent with the progressively larger extrapolation required to estimate the plateau as the voltage reduction increases.
For the -40% curve, the fitted plateau decreases to $L = 0.465 \pm 0.943$. This is the first case in which the fit does not converge to the upper limit $L = 1$, although the large uncertainty still prevents a precise determination of the plateau value. The -50% curve gives an even lower fitted plateau, $L = 0.118 \pm 0.183$. Thus, starting from the -40% reduction, the fitted plateau values, obtained with the same functional form, remain below the upper limit allowed by the fit. These results indicate that the large-voltage-reduction regime is increasingly dominated by the extrapolation of the fitted function beyond the measured region, and the corresponding plateau values should therefore be interpreted with caution.
The reduced χ^2 values obtained for the three fits are 0.17, 0.07, and 0.09 for the 35%, 40%, and 50% reductions, respectively. These values are smaller than those obtained for the lower voltage reductions. This is consistent with the larger statistical uncertainties associated with the lower counting rates observed in this regime, which reduce the weight of the individual data points in the fit.
The same plot (Fig. 3.7a) also includes the efficiency curve corresponding to a 100% voltage reduction of the G1Top channel. In this case, the curve appears to be essentially flat and compatible with almost zero efficiency over the displayed range. However, the apparent flatness is mainly due to the scale of the plot, as the corresponding measurements are better resolved in Fig. 3.7b.



(a) Efficiency curves as a function of the HV configuration for 35%, 40%, and 50% voltage reductions applied to the G1Top channel. The nominal-HV efficiency curve, the −30% curve, and the −100% curve are also shown as references.



(b) Efficiency curve obtained with a 100% voltage reduction applied to the G1Top channel, as a function of the HV configuration.

FIGURE 3.7: Efficiency curves obtained for large voltage reductions applied to the G1Top channel.

The 100% voltage reduction was investigated as an extreme condition in which the voltage across GEM1 is reduced to a value such that the electric field inside the GEM holes is equal to the electric field in the drift gap,

$$E_{\mathrm{GEM1}} = E_{\mathrm{drift}}. \tag{3.13}$$

At this field strength, electrons can be transported through the GEM holes, while electron multiplication is expected to be negligible.
The condition in Eq. (3.13) was obtained by calculating the electric field in the drift gap for each HV configuration and then determining the voltage to be applied across GEM1 according to

$$V_{\mathrm{G1Top}} = E_{\mathrm{drift}}\ d, \tag{3.14}$$

where d is the thickness of the GEM foil. The voltage values obtained in this way were then applied to the G1Top channel for each point of the scan.
The parameters used to determine the G1Top voltage at the initial HV configuration are reported in Table 3.1. The voltage difference across the drift gap at $I_{\mathrm{eq}} = 735\,\mu\mathrm{A}$ corresponds to an electric field of approximately $2.75\,\mathrm{kV\,cm^{-1}}$. The corresponding voltage across the GEM foil is therefore chosen to reproduce the same electric field across its 0.05 mm thickness.

TABLE 3.1: Voltage differences and corresponding electric fields in the drift gap and across the GEM1 foil for the initial HV configuration at $I_{\mathrm{eq}} = 735\,\mu\mathrm{A}$.

HV channel	**Distance [mm]**	**Voltage difference [V]**	**Electric field [kV/cm]**
Drift	3.00	826.9	2.75
G1Top	0.05	13.8	2.75

The same procedure was repeated for each HV configuration of the scan. Starting from the configuration corresponding to $I_{\mathrm{eq}} = 735\,\mu\mathrm{A}$, the equivalent current was decreased in steps of $9\,\mu\mathrm{A}$, resulting in a total of 11 HV points. For each point, the acquisition was performed for 8 h, owing to the very low number of detected triple coincidences in this regime. The resulting efficiency values and the corresponding fit are shown in Fig. 3.7b.

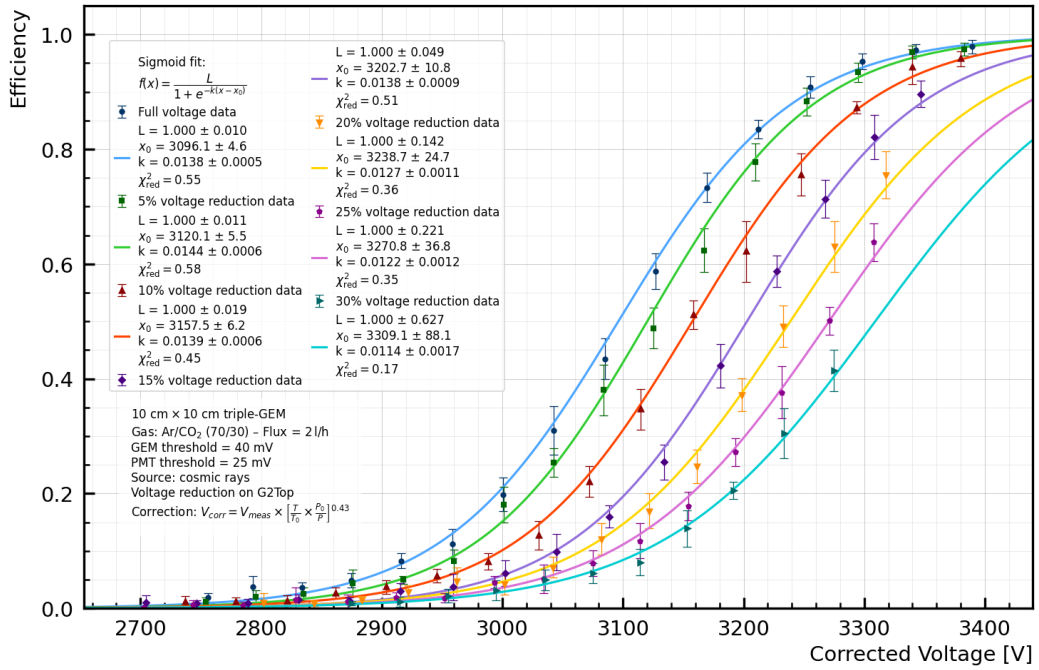
The fitted plateau for the 100% G1Top voltage reduction is $L = 0.028 \pm 0.043$. Despite the large uncertainty, the fitted central value corresponds to an efficiency of only about 3%, indicating that the complete removal of the voltage across GEM1 leads to a strong suppression of the detector response. The large uncertainty reflects the very low number of detected events in this regime and the consequent limited constraint on the fitted plateau.
The same limiting condition was also investigated for GEM2 and GEM3, by applying the corresponding voltage configuration at the maximum equivalent current of $I_{\text{eq}} = 735\,\mu\text{A}$. In both cases, no triple coincidences were observed during an acquisition period of 8 h. Since even the maximum-voltage configuration produced no detectable signal, it was not possible to measure an efficiency curve for the complete voltage reduction of G2Top or G3Top.
These measurements show that a complete loss of the voltage across any of the three GEM foils has a severe impact on the detector response. In the case of GEM1, a small residual efficiency was still observed, whereas the complete voltage reduction of GEM2 or GEM3 resulted in no detectable signal under the investigated conditions. This difference highlights the increasingly severe impact of losing a GEM stage at the later stages of the amplification chain.

3.4.2 G2Top and G3Top

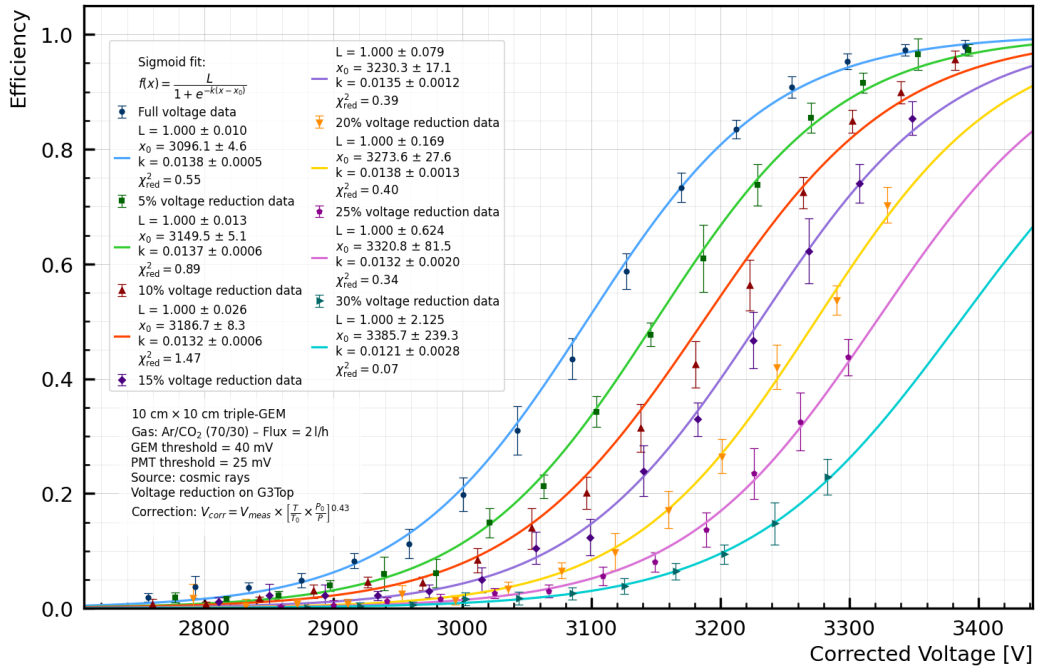
The experience gained from the G1Top study allowed the acquisition procedure to be refined by optimizing the number of HV points and the acquisition time per point. The optimized procedure was then adopted for both G2Top and G3Top, using the same measurement conditions for the two channels. I selected the voltage reductions, number of HV points, and acquisition time per point as follows:

- **5%, 10%**: 16 HV points of 1 h each.
- **15%, 20%**: 14 HV points of 1.5 h each.
- **25%**: 12 HV points of 1.75 h each.
- **30%**: 11 HV points of 2 h each.

Fig. 3.8 shows the resulting efficiency curves for G2Top (Fig. 3.8a) and G3Top (Fig. 3.8b).



(a) Efficiency curves obtained for different voltage reductions applied to the G2Top channel.



(b) Efficiency curves obtained for different voltage reductions applied to the G3Top channel.

FIGURE 3.8: Efficiency curves as a function of the HV configuration for voltage reductions ranging from 5% to 30% applied to the G2Top and G3Top channels. The nominal-HV efficiency curve is also shown as a reference.

As for G1Top, increasing the voltage reduction results in a progressive shift of the efficiency curves towards lower values. The fitted plateau parameters reach the upper limit allowed in the fit, $L \leq 1$, while their uncertainties increase with the voltage reduction. This behaviour is consistent with the progressively larger extrapolation required to determine the plateau as the maximum-voltage point of each curve moves towards lower efficiency values.

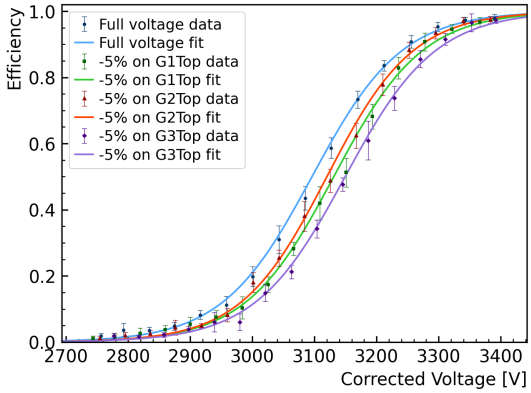
3.4.3 Foil comparison

The results presented in the previous sections show the effect of reducing the voltage applied across each of the three GEM foils separately. While this representation is useful to study the response of each foil as a function of the applied voltage reduction, it does not provide a direct comparison of the three foils under equivalent conditions. Such a comparison is of interest to investigate whether the detector efficiency is affected differently depending on which GEM foil is subjected to the voltage reduction.

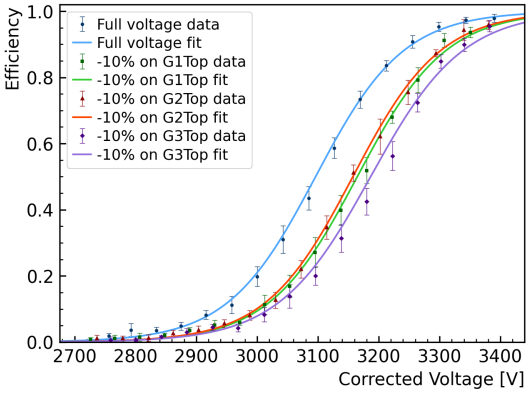
For this purpose, the efficiency curves previously presented for the three foils are rearranged in Fig. 3.9 according to the applied voltage reduction. Each panel corresponds to a given reduction, ranging from 5% (Fig. 3.9a) to 30% (Fig. 3.9f) in steps of 5%. For each value, the curves obtained by reducing the voltage of G1Top, G2Top, and G3Top are shown together with the reference curve measured at the nominal voltage configuration. This representation allows a direct comparison of the detector response to the same relative voltage reduction applied to different GEM foils.

It is worth stressing that no new measurements are introduced in this comparison. The curves shown in Fig. 3.9 are the same data already discussed in the previous sections; only their representation is changed.

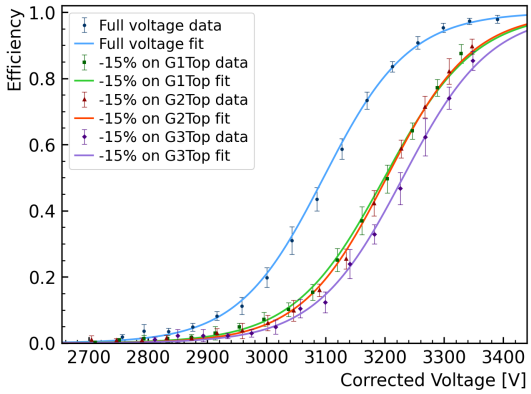
The comparison shown in Fig. 3.9 confirms the general trend already observed in the previous sections: for all three GEM foils, the efficiency decreases as the magnitude of the voltage reduction increases. More interestingly, the comparison at fixed voltage reduction highlights a different behaviour among the three foils. The curves obtained for G1Top and G2Top remain very close to each other over the whole range of investigated reductions. Although small differences can be observed for some configurations, with G2Top showing a slightly higher efficiency at a 5% (Fig. 3.9a) reduction and G1Top being marginally higher at 15% (Fig. 3.9c),



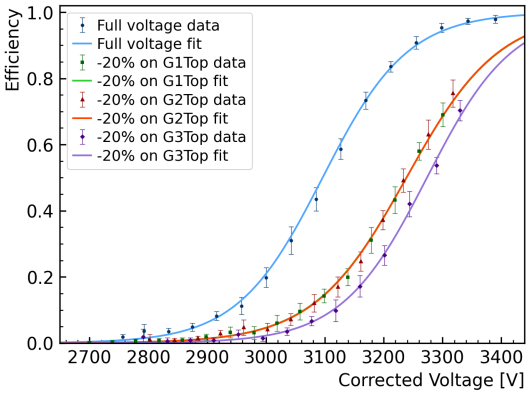
(a) 5% voltage reduction.



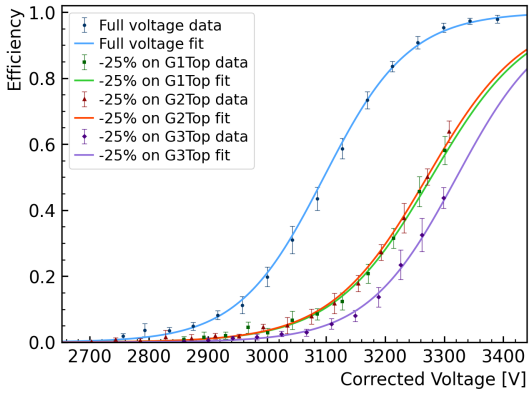
(b) 10% voltage reduction.



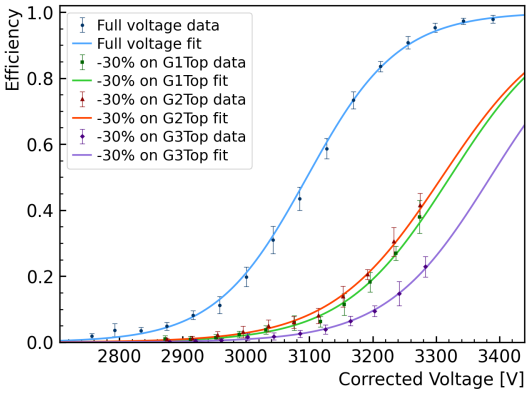
(c) 15% voltage reduction.



(d) 20% voltage reduction.



(e) 25% voltage reduction.



(f) 30% voltage reduction.

FIGURE 3.9: Comparison of the efficiency curves at different voltage reductions. Each panel corresponds to a fixed reduction, from 5% to 30%, and shows the reference curve at nominal voltage together with the curves obtained by applying the same reduction to G1Top, G2Top, and G3Top.

no systematic difference between the two foils can be identified. In some cases, such as for the 20% reduction (Fig. 3.9d), the two curves are almost completely superimposed. Therefore, within the precision of the present measurements, the effect of a voltage reduction on G1Top and G2Top appears to be substantially similar, and no clear hierarchy between the two foils can be established.
In contrast, the G3Top curve is the one with the lowest efficiency already for the smallest investigated reduction of 5% (Fig. 3.9a). This difference becomes progressively more pronounced as the magnitude of the voltage reduction increases, with the largest separation from the G1Top and G2Top curves observed for the 30% reduction (Fig. 3.9f). This indicates that, among the three GEM foils, GEM3 is the one for which a reduction of the applied voltage produces the strongest degradation of the detector efficiency. Within the conditions investigated in this study, GEM3 can therefore be identified as the most critical foil in terms of the impact of a voltage reduction on the detector response. This behaviour is expected, as GEM3 is the last multiplication stage and therefore provides the final contribution to the avalanche charge before the signal reaches the readout. A reduction of its gain can consequently have a direct impact on the signal amplitude and on its ability to exceed the discriminator threshold. The importance of this effect is quantified experimentally in the present study.
This result is particularly relevant when considered in the context of the operational experience of GE1/1 during Run 3. As discussed in Section 1.4.2, the monitoring of the CMS chambers during the 2021–2023 period showed that GEM3 was involved in the generation of short circuits approximately twice as often as GEM1 and GEM2. The present measurements do not establish a causal relationship between the higher occurrence of short circuits on GEM3 and its larger sensitivity to voltage reductions. Nevertheless, the two observations are particularly relevant when considered together: the GEM foil that was observed to be most frequently affected by short circuits during CMS operation is also the one for which a voltage reduction produces the largest degradation of the detector efficiency in the present study. Consequently, the higher sensitivity of GEM3 to the loss of applied voltage makes the occurrence of short circuits on this foil particularly detrimental to the detector performance.
As a complementary representation of the results, the efficiency curves presented in this section can also be plotted as a function of alternative quantities describing the detector operating conditions. In particular, the use of the equivalent current

and the sum of the voltages applied to the top channels provides two alternative ways of comparing the detector response. These representations are based on the same measurements discussed above and are presented in Appendix A.

3.5 Voltage increase across gas gaps

As described in Section 1.4.2, in addition to the reduction of the voltage across the affected GEM foil, a short circuit also modifies the voltage across the subsequent gas gap. This effect originates from the current flowing through the shorted branch. The resulting voltage drop across the bottom filter resistor shifts the physical potential of the bottom electrode of the affected foil, while the potential of the following electrode is not affected by the short-circuit current. Consequently, the voltage difference across the gas gap increases with respect to its nominal value, as described by Eq. (1.10). In the present experiment, this effect was reproduced by increasing the voltage applied to the corresponding bottom HV channel.
Although Eq. (1.10) shows that the voltage increase across the gas gap is smaller than the voltage reduction across the affected GEM foil (Eq. (1.8)), its impact on the detector performance cannot be inferred from the magnitude of the voltage variation alone. The purpose of the measurements presented in this section is therefore to investigate the effect of an increased gas-gap voltage on the detection efficiency of the detector.
The increase in the gas-gap voltage was investigated only in combination with the primary effect of a short circuit, namely the reduction of the voltage across the affected GEM foil. The configuration in which the gas-gap voltage is increased while the GEM foils remain at their nominal voltages was not investigated. In addition, such a configuration would correspond to an over-voltage condition with respect to the nominal operating point and was therefore not considered appropriate for the experimental setup.
More generally, a reduction of the voltage applied to an HV channel does not introduce an over-voltage condition in the detector. Conversely, increasing the voltage above its nominal value modifies the electric-field configuration beyond the established operating conditions and may result in undesirable or potentially unsafe operating conditions. For this reason, the voltage increases investigated in this section were considered only together with the corresponding voltage reductions across the GEM foils.

The simultaneous reproduction of both effects of a short circuit was therefore investigated only for a 5% reduction of the voltage across the affected GEM foil. While the voltage to be applied to the top channels can be directly determined by reducing the corresponding nominal values by the chosen percentage, the voltage increase to be applied to the bottom channel requires an additional calculation. The voltage to be applied to the bottom channel, $V_{\mathrm{bot}}^{\mathrm{inc}}$, can be expressed as the sum of its nominal value, V_{bot}, and the increase induced by the short circuit, V^{inc}:

$$V_{\mathrm{bot}}^{\mathrm{inc}} = V_{\mathrm{bot}} + V^{\mathrm{inc}}. \tag{3.15}$$

The value of V^{inc} can be determined from the voltage reduction chosen as the experimental parameter. Starting from Eq. (3.12), the equivalent protection resistance $R_{p,\mathrm{eq}}^{s}$ associated with a given percentage voltage reduction $V_{\mathrm{loss}}^{\%}$ can be obtained as

$$R_{p,\mathrm{eq}}^{s} = \frac{R_f^{\mathrm{top}} + R_f^{\mathrm{bot}}}{V_{\mathrm{loss}}^{\%}} - \left(R_f^{\mathrm{top}} + R_f^{\mathrm{bot}}\right). \tag{3.16}$$

Substituting this expression into Eq. (1.5) gives the corresponding short-circuit current:

$$I_{\mathrm{short}} = \frac{V_{\mathrm{top}}\, V_{\mathrm{loss}}^{\%}}{R_f^{\mathrm{top}} + R_f^{\mathrm{bot}}}. \tag{3.17}$$

According to Eq. (1.10), the increase in the voltage of the bottom electrode is given by the voltage drop across the corresponding bottom filter resistor:

$$V^{\mathrm{inc}} = I_{\mathrm{short}} \cdot R_f^{\mathrm{bot}}. \tag{3.18}$$

Combining this expression with the short-circuit current above yields

$$V^{\mathrm{inc}} = V_{\mathrm{top}}\, V_{\mathrm{loss}}^{\%}\, \frac{R_f^{\mathrm{bot}}}{R_f^{\mathrm{top}} + R_f^{\mathrm{bot}}}. \tag{3.19}$$

For the GE1/1 configuration, where $R_f^{\mathrm{top}} = R_f^{\mathrm{bot}}$, this expression simplifies to

$$V^{\mathrm{inc}} = V_{\mathrm{loss}}^{\%}\, \frac{V_{\mathrm{top}}}{2}. \tag{3.20}$$

Therefore, once the percentage reduction of the voltage across the affected GEM foil is selected, the corresponding increase of the voltage across the subsequent gas

gap can be directly determined.
As already mentioned, the only voltage reduction that I tried for this study was 5%, so using Eq. (3.20) it is possible to calculate the incremented voltages that have to be applied to the bottom channels. The results, for the higher I_{eq} configurations, using Eq. (2.1), are shown in Table 3.2.

TABLE 3.2: Nominal and increased voltage values for the three bottom channels for a 5% voltage reduction across the previous GEM foil in the avalanche multiplication chain (for example in case of GEM2 foil, the altered electric field is the one generated by G2Bot HV channel). The first row reports the maximum voltage previously applied to each channel, corresponding to the highest equivalent current configuration, $I_{eq} = 735\,\mu A$. The remaining rows report the corresponding voltage values after applying the calculated increase. Grey-highlighted values indicate the highest I_{eq} configuration for which the increased voltage does not exceed the maximum voltage previously applied to the corresponding channel.

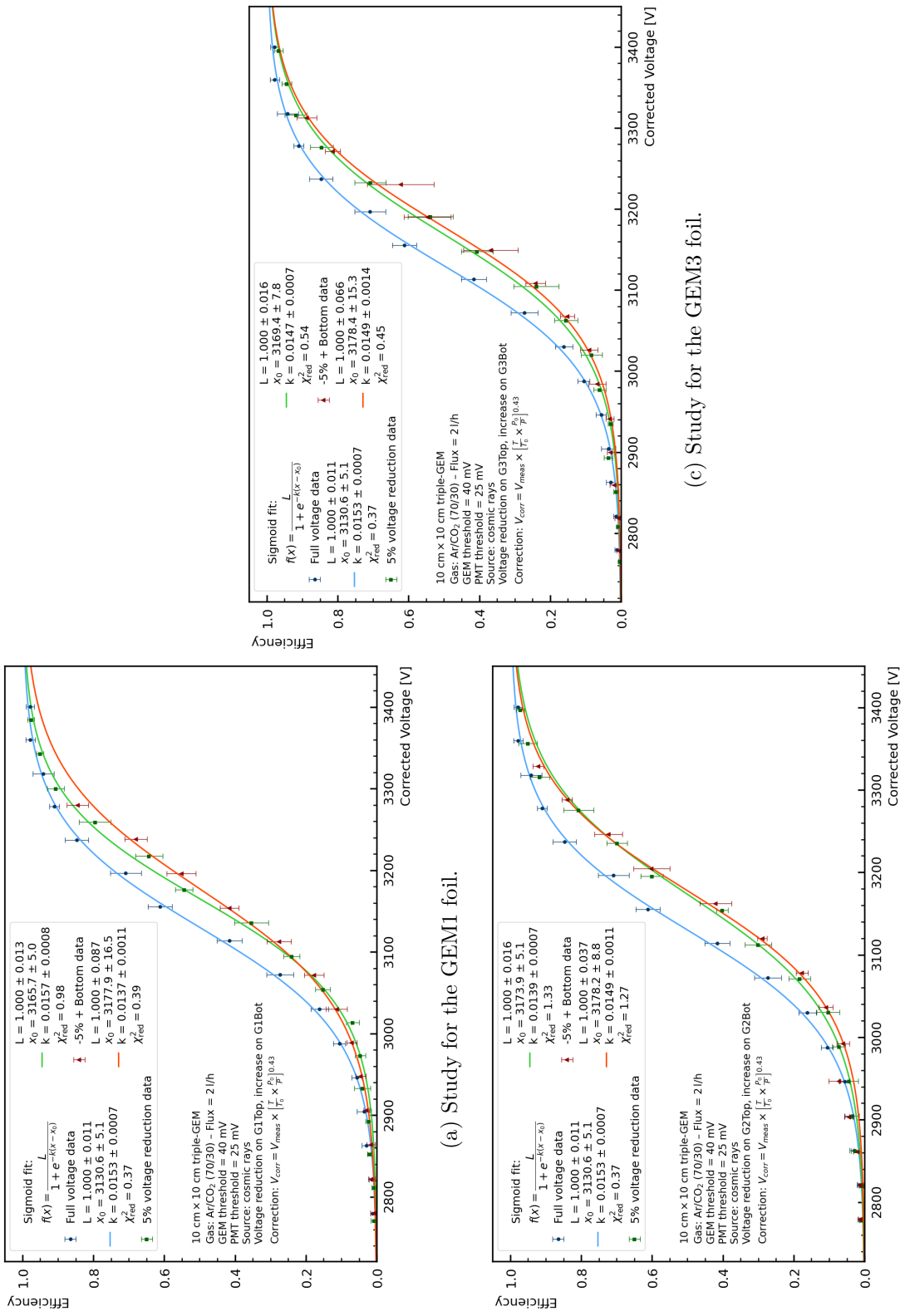
I_{eq} **(μA)**	V_{G1Bot} **(V)**	V_{G2Bot} **(V)**	V_{G3Bot} **(V)**
735	**321.9**	**643.1**	**459.4**
735	332.2	653.2	469.0
726	328.2	645.2	463.3
717	324.1	**637.2**	**457.5**
708	**320.0**	629.2	451.8
699	315.9	621.2	446.0

The resulting voltage increases were then compared with the maximum values previously applied to the corresponding channels, in order to define the I_{eq} range compatible with this constraint. For the 5% voltage reduction on top channel, the corresponding increase can be calculated using Eq. (3.20). The resulting values for the highest I_{eq} configurations, calculated using Eq. (2.1), are reported in Table 3.2. The I_{eq} range was selected for each bottom channel so that the increased voltage would remain below the maximum voltage provided in Table 3.2: the safety limit used corresponded to the voltage provided by the configuration I_{eq} =735 µA. For example, the maximum voltage previously applied to G1Bot was 321.9 V. After applying the calculated increase, the voltage at $I_{eq} = 735\,\mu A$ would become 332.2 V, exceeding this value. The highest I_{eq} configuration for which the increased voltage remains below the reference value is therefore $I_{eq} = 708\,\mu A$, corresponding to an

increased voltage of 320.0 V. The same procedure gives a maximum equivalent current of $I_{eq} = 717\,\mu A$ for both G2Bot and G3Bot.
In order to obtain results comparable with the efficiency measurements performed with a 5% voltage reduction across each foil, the same I_{eq} configurations and acquisition times were used for each corresponding measurement, as described in Section 3.4.1 for G1Top and Section 3.4.2 for G2Top and G3Top. However, since the highest-voltage configurations were excluded when the corresponding voltage increase across the gas gap was applied, the number of voltage points could not be kept identical between the original -5% curves and the corresponding curves including the gas-gap voltage increase.
Since several months had elapsed since the previous efficiency measurements, a new set of reference measurements was acquired, including the full-voltage configuration and the 5% voltage reductions on the top channels. These measurements were performed using the same I_{eq} configurations and acquisition times as the corresponding previous measurements.
To summarize, the efficiency curves presented in this section were acquired under the following conditions:

- **Full voltage, -5% on G1Top, -5% on G2Top, -5% on G3Top**: 16 HV points of 1 h each, starting from $I_{eq} = 735\,\mu A$.
- **-5% on G1Top + G1Bot voltage increase**: 13 HV points of 1 h each, starting from $I_{eq} = 708\,\mu A$.
- **-5% on G2Top + G2Bot voltage increase, -5% on G3Top + G3Bot voltage increase**: 14 HV points of 1 h each, starting from $I_{eq} = 717\,\mu A$.

The results are shown in Fig. 3.10.
In all three cases, the efficiency curve obtained by applying the voltage increase to the bottom channel lies slightly below the corresponding curve with only the 5% voltage reduction. This indicates that the increase in the voltage across the corresponding gas gap has a small negative effect on the detector efficiency. Although the difference is relatively small, the same behaviour is observed for all three GEM foils.
No clear difference in the magnitude of this effect can be identified among the three foils. Therefore, unlike the comparison of the effects produced by voltage reductions on the individual top channels (section 3.4.3), these measurements do not provide



(a) Study for the GEM1 foil.

(b) Study for the GEM2 foil.

(c) Study for the GEM3 foil.

FIGURE 3.10: Efficiency curves obtained by applying a 5% voltage reduction to a top channel together with the corresponding voltage increase on the bottom channel. The full-voltage and −5% curves are also shown in each plot as reference.

evidence for a different sensitivity of the three foils to the gas-gap voltage increase. The main observation is instead the systematic behaviour observed in all three cases.
From the point of view of the short-circuit compensation strategy, this result indicates that the voltage increase across the gas gap represents a secondary effect that slightly worsens the detector efficiency. Consequently, if this voltage increase could be compensated while preserving the voltage reduction across the affected GEM foil, a small improvement in efficiency would be expected.

3.6 Double voltage reductions across foils

In the previous sections, the effect of a short circuit was investigated by applying a voltage reduction to only one GEM foil at a time. However, scenarios in which more than one foil is affected simultaneously cannot be excluded. This section presents the study of simultaneous voltage reductions on two GEM foils.
The voltage reductions on the individual foils were applied following the same procedure described in Sections 3.4.1 and 3.4.2. In particular, each foil was treated independently, and the selected percentage reduction was applied to the corresponding top channel. The difference in the present study is that the reductions on two different foils were applied simultaneously.
Only voltage reductions on the top channels were investigated in this study. No measurements combining the voltage reductions with the corresponding increases on the bottom channels were performed.
The set of possible voltage reductions was limited to 5%, 10%, 15%, and 20%. For each pair of GEM foils, a fixed reduction was applied to one foil while all possible reductions were tested on the other foil. Combinations in which the same pair of reductions was obtained by exchanging the two foils were not repeated. The complete set of combinations investigated is reported in Table 3.3, resulting in a total of 48 efficiency curves.
The experience gained from the previous measurements allowed the I_{eq} configurations, the number of voltage points, and the acquisition time for each point to be defined for the present study. As in the previous efficiency measurements, all curves were acquired starting from the maximum equivalent current of $I_{eq} = 735\,\mu A$, with the subsequent configurations obtained using steps of $9\,\mu A$.

TABLE 3.3: Summary of the 48 combinations of voltage reductions applied simultaneously to two GEM foils. Each row represents four combinations, obtained by fixing the reduction on one top channel and varying the reduction on the other among 5%, 10%, 15%, and 20%. Combinations corresponding to the same pair of reductions applied to the same two foils were not repeated.

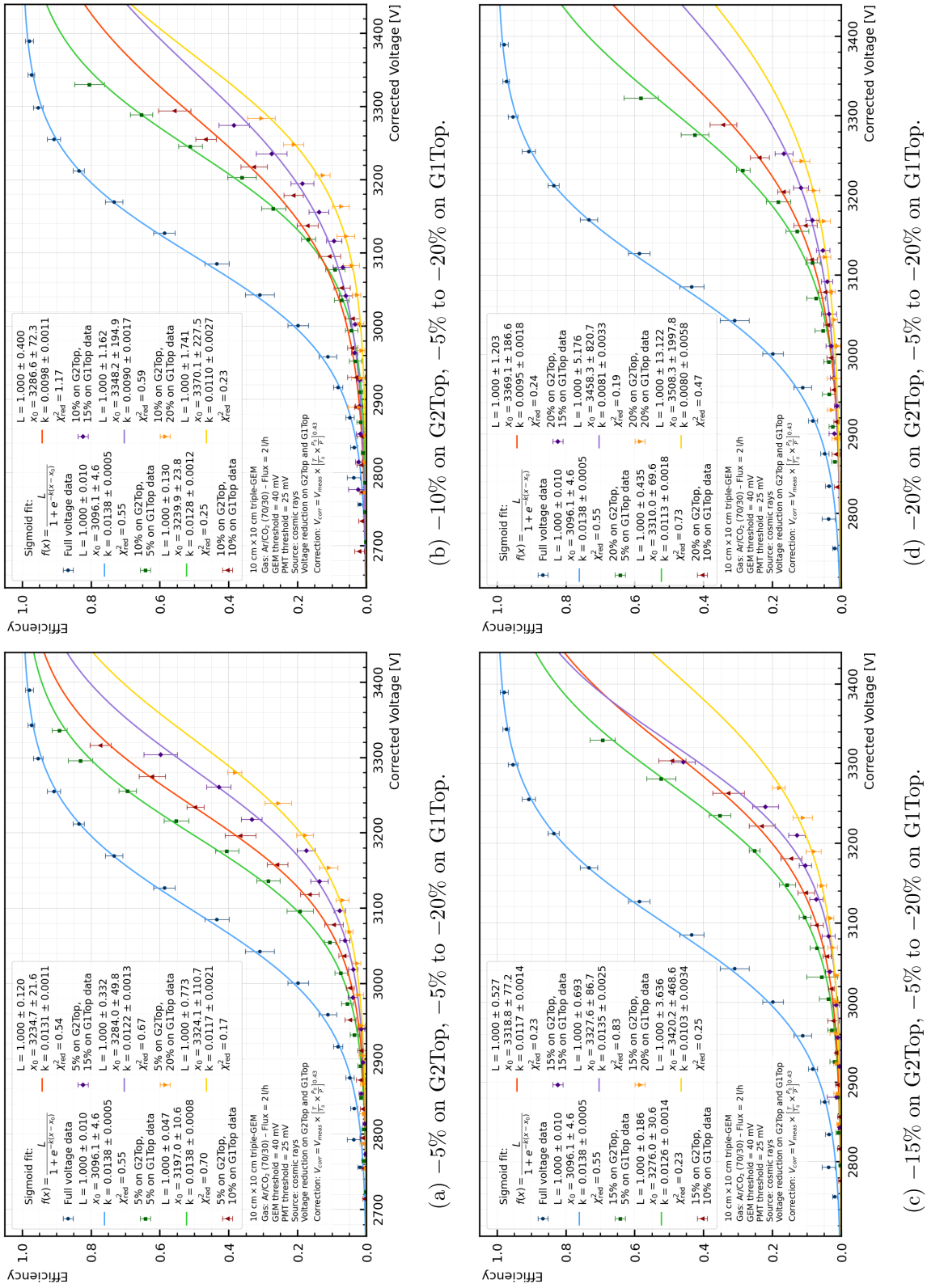
G1Top	**G2Top**	**G3Top**
5%, 10%, 15%, 20%	5%	
5%, 10%, 15%, 20%	10%	
5%, 10%, 15%, 20%	15%	
5%, 10%, 15%, 20%	20%	
	5%	5%, 10%, 15%, 20%
	10%	5%, 10%, 15%, 20%
	15%	5%, 10%, 15%, 20%
	20%	5%, 10%, 15%, 20%
5%		5%, 10%, 15%, 20%
10%		5%, 10%, 15%, 20%
15%		5%, 10%, 15%, 20%
20%		5%, 10%, 15%, 20%

The same procedure was adopted for all combinations of top channels, denoted as GiTop and GjTop, with $i \neq j$ and $i, j \in \{1, 2, 3\}$. The number of points and the acquisition time were chosen according to the specific combination of voltage reductions, as summarized below:

- **-5% on GiTop + -5% on GjTop, -5% on GiTop + -10% on GjTop**: 16 HV points of 1 h each.
- **-5% on GiTop + -15% on GjTop, -5% on GiTop + -20% on GjTop**: 14 HV points of 1.5 h each.
- **-10% on GiTop + -5% on GjTop, -10% on GiTop + -10% on GjTop**: 16 HV points of 1.5 h each.

- **-10% on GiTop + -15% on GjTop, -10% on GiTop + -20% on GjTop**: 14 HV points of 2 h each.
- **-15% on GiTop + -5% on GjTop, -15% on GiTop + -10% on GjTop**: 14 HV points of 2 h each.
- **-15% on GiTop + -15% on GjTop, -15% on GiTop + -20% on GjTop**: 12 HV points of 2.5 h each.
- **-20% on GiTop + -5% on GjTop, -20% on GiTop + -10% on GjTop**: 12 HV points of 2.5 h each.
- **-20% on GiTop + -15% on GjTop, -20% on GiTop + -20% on GjTop**: 10 HV points of 3 h each.

The curves obtained are shown in Fig. 3.11 for G1Top-G2Top combinations, Fig. 3.12 G2Top-G3Top combinations, and Fig. 3.13 G1Top-G3Top combinations.
Starting from the G1Top-G2Top combinations case, Fig. 3.11 panels show a consistent overall behaviour. In all cases, increasing the reduction applied to G1Top results in a progressive decrease of the efficiency, with the curves generally ordered according to the combined magnitude of the two voltage reductions. The separation between the curves is not always uniform; for example, the configurations with 10% and 15% reduction on G1Top in the scan with a fixed 15% reduction on G2Top (Fig. 3.11c) produce very similar efficiency curves. This could indicate that the effect of the two simultaneous reductions may not be simply reflected by an equal spacing of the curves as their nominal voltage reductions are increased. Nevertheless, no anomalous behaviour is observed in this set of measurements.
For the G2Top-G3Top combinations the plots in Fig. 3.12 show the same general trend, with increasing voltage reductions resulting in progressively lower efficiency curves. Two features, however, deserve mention. For the configuration with a fixed 10% reduction on G2Top (Fig. 3.12b), the curve corresponding to an additional 10% reduction on G3Top shows an apparent offset at the lower-voltage end with respect to the other curves. At higher voltages, the curve follows the expected behaviour more closely. The origin of this deviation cannot be established from the present measurements and it is therefore not interpreted as a systematic effect. For the configuration with a 20% reduction on G2Top (Fig. 3.12d), the curve obtained with an additional 20% reduction on G3Top does not reach the nominal



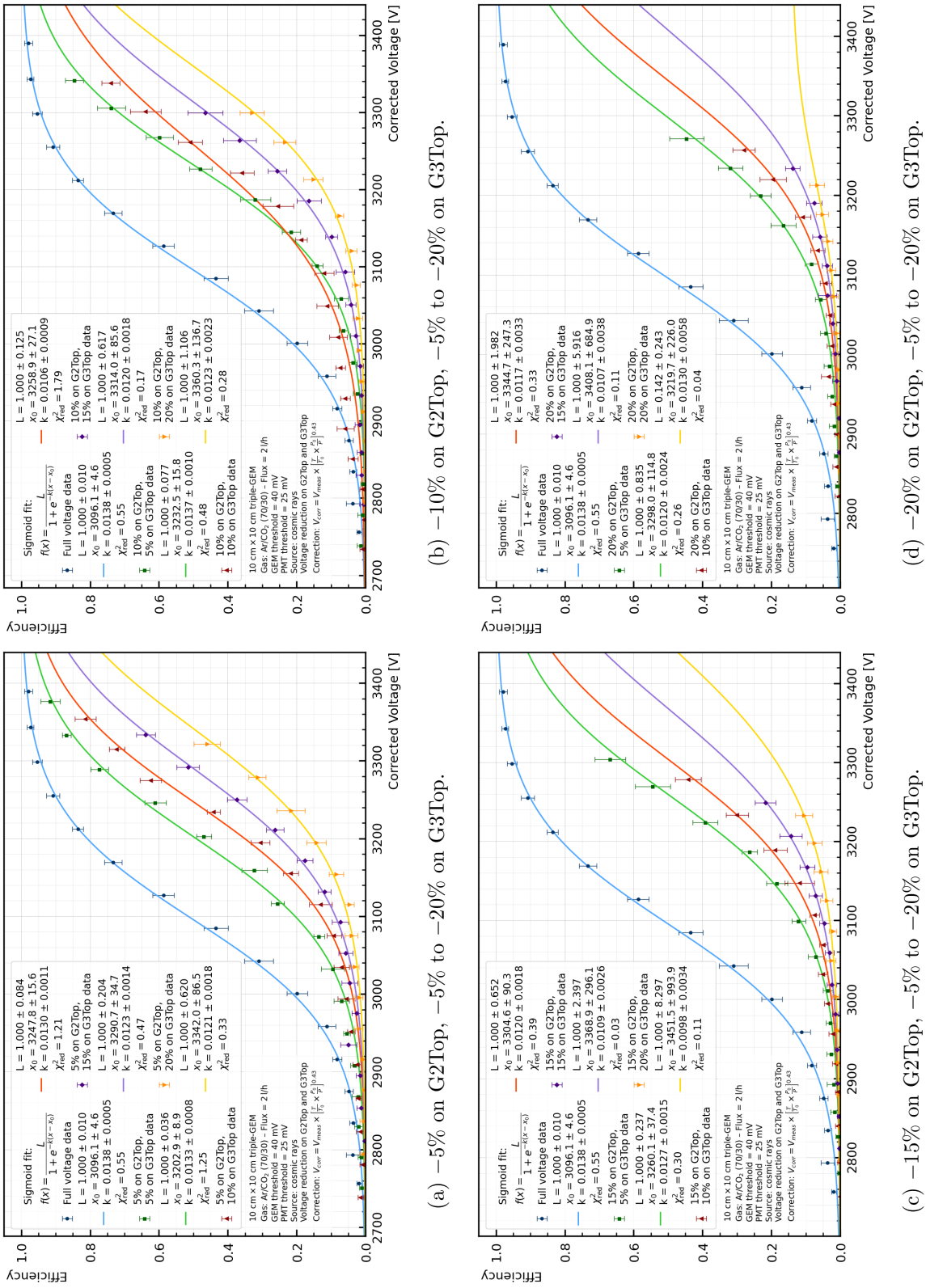
(a) -5% on G2Top, -5% to -20% on G1Top.

(b) -10% on G2Top, -5% to -20% on G1Top.

(c) -15% on G2Top, -5% to -20% on G1Top.

(d) -20% on G2Top, -5% to -20% on G1Top.

FIGURE 3.11: Efficiency curves for combined voltage reductions on the G1Top and G2Top channels. In each panel, the reduction on G2Top is kept fixed while the reduction on G1Top is varied, as indicated in the corresponding subcaption.



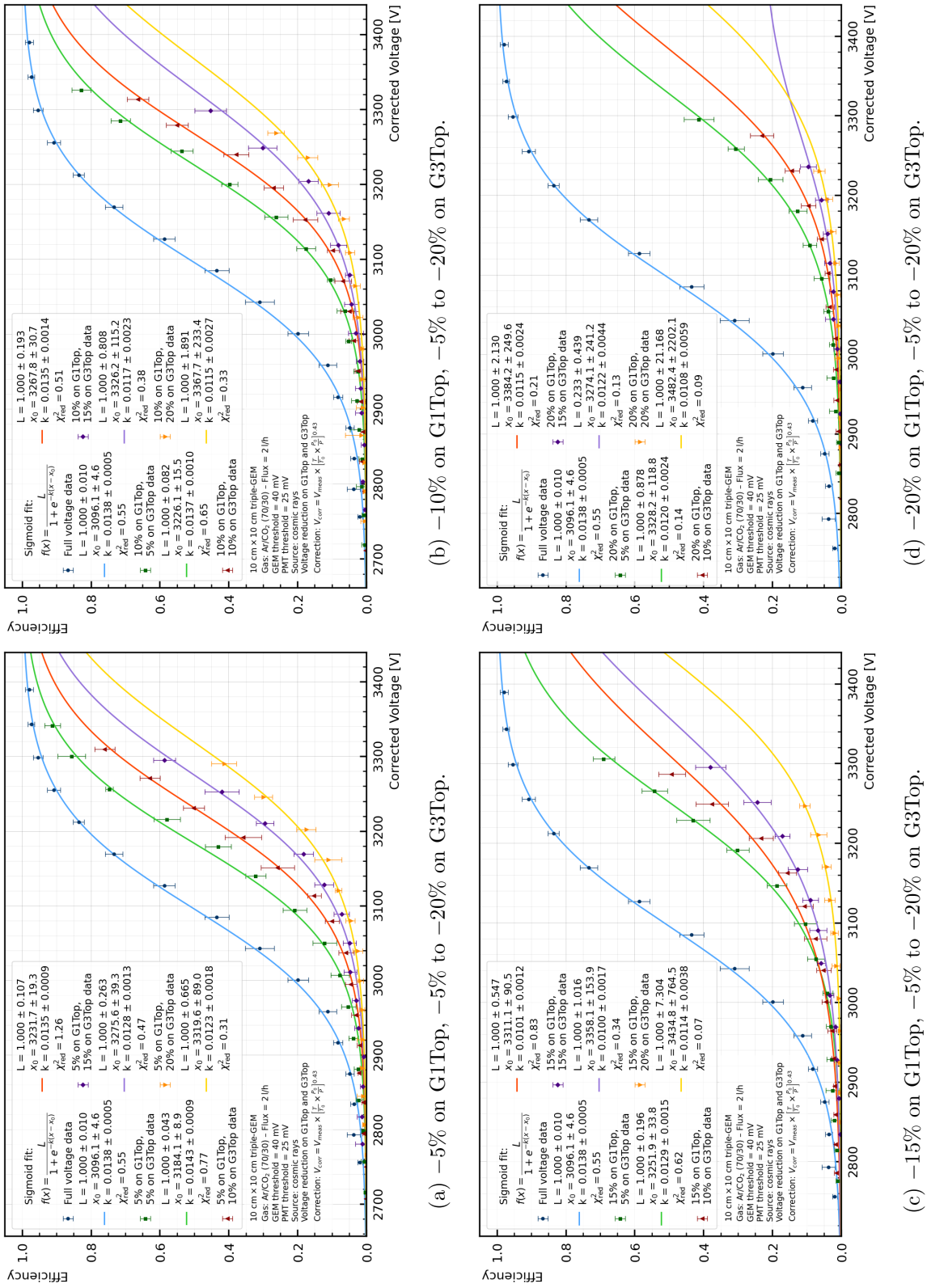
(a) −5% on G2Top, −5% to −20% on G3Top.

(b) −10% on G2Top, −5% to −20% on G3Top.

(c) −15% on G2Top, −5% to −20% on G3Top.

(d) −20% on G2Top, −5% to −20% on G3Top.

FIGURE 3.12: Efficiency curves for combined voltage reductions on the G2Top and G3Top channels. In each panel, the reduction on G2Top is kept fixed while the reduction on G3Top is varied, as indicated in the corresponding subcaption.



(a) −5% on G1Top, −5% to −20% on G3Top.

(b) −10% on G1Top, −5% to −20% on G3Top.

(c) −15% on G1Top, −5% to −20% on G3Top.

(d) −20% on G1Top, −5% to −20% on G3Top.

FIGURE 3.13: Efficiency curves for combined voltage reductions on the G1Top and G3Top channels. In each panel, the reduction on G1Top is kept fixed while the reduction on G3Top is varied, as indicated in the corresponding subcaption.

efficiency plateau within the investigated voltage range. The corresponding fit converges to a plateau value of $L = 0.142$. As discussed for the single-foil measurements, this value should be interpreted with caution when the plateau is poorly constrained by the measured data, since the fitted result can be strongly affected by the extrapolation beyond the investigated range.
Finally, the plots in Fig. 3.13, obtained with the G1Top-G3Top combinations, also show a consistent decrease in efficiency as the magnitude of the reductions is increased. No significant deviations from this behaviour are observed in the first three panels. In the last panel (Fig. 3.13d), corresponding to a fixed 20% reduction on G1Top, the curve obtained with a 15% reduction on G3Top gives a fitted plateau of $L = 0.233$, while the 20%–20% configuration gives a plateau compatible with the upper limit of the fit, $L = 1$, but with a very large uncertainty of approximately 21. The latter result is therefore essentially unconstrained and does not provide evidence for a higher plateau efficiency in the 20%–20% configuration.
Overall, the measurements show that simultaneous voltage reductions on two GEM foils lead to a progressive degradation of the detector efficiency as the magnitude of the reductions is increased. The observed behaviour is qualitatively consistent with the results obtained when the foils were studied individually. However, the present measurements do not show a simple linear relation between the efficiency loss and the sum of the two applied voltage reductions, as the separation between the curves is not uniform in all configurations.
The comparison of the three possible foil pairs does not reveal a clear additional hierarchy among the combinations investigated. In particular, the irregularities observed in a few configurations are either limited to part of the voltage range or associated with poorly constrained plateau fits. Therefore, within the precision of the present measurements, the main result of this study is the overall degradation of the detector efficiency produced by the simultaneous reduction of the voltage across two GEM foils, rather than a distinct sensitivity associated with a specific pair of foils.

3.6.1 Comparison of voltage reductions

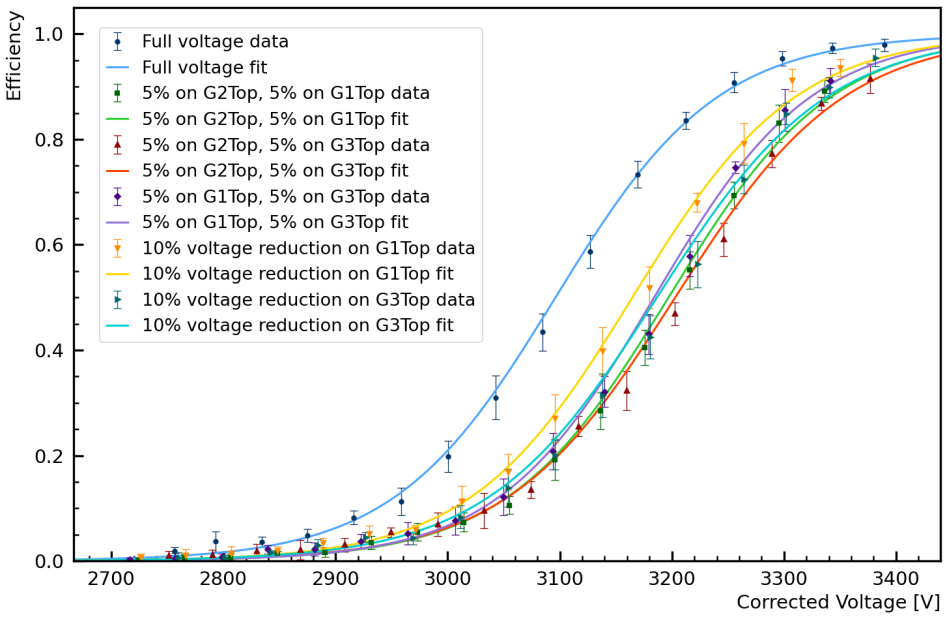
The measurements presented in the previous sections allow a further comparison between the efficiency curves obtained with single and double voltage reductions. In particular, it is interesting to investigate whether, for a given total percentage

reduction, the detector response depends significantly on how the reduction is distributed among different GEM foils. This analysis does not involve any additional measurements, but consists of an alternative visualization and comparison of efficiency curves already presented in the previous sections.

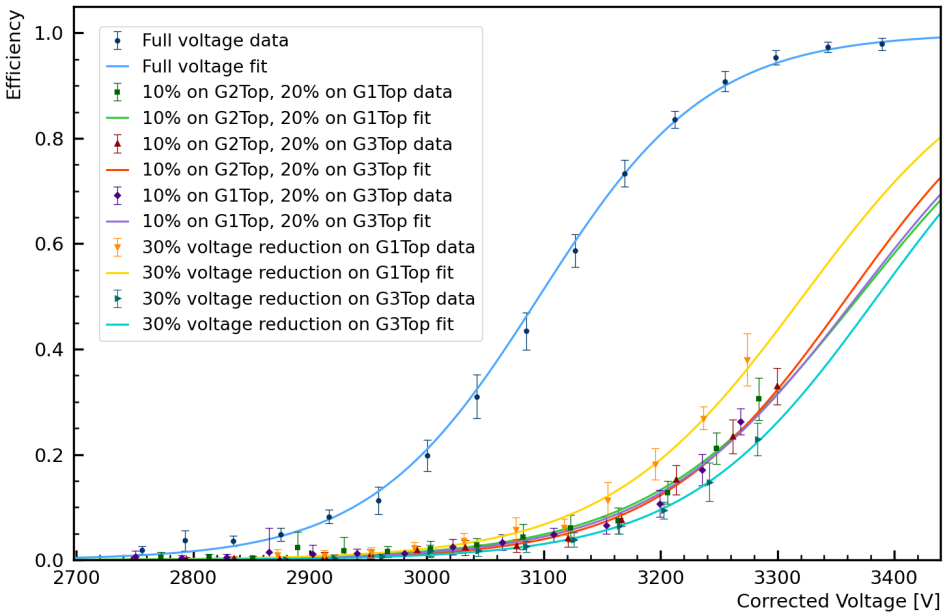
The comparison, shown in Fig. 3.14, was performed by considering two representative values of the summed percentage reduction. It should be noted that equal percentage reductions do not correspond to equal voltage losses on the three foils, since the nominal voltages of the top channels differ (Table 2.1). For instance, at I_{eq} =700 µA, a 5% reduction corresponds to about 19.6 V on G1Top, 19.3 V on G2Top and 18.4 V on G3Top. The same percentage reduction therefore removes a slightly larger absolute voltage from G1Top and G2Top than from G3Top, and the sum of the percentage reductions is not strictly equivalent to the total voltage lost. For this analysis, the smallest possible value corresponds to a 5%+5% reduction on two different foils, while the largest corresponds to a 30% reduction on a single foil. For each case, the curves obtained with different distributions of the same summed percentage reduction were compared with the corresponding single-foil reductions. The term "total reduction" in the following discussion refers to the sum of the percentage reductions applied to the individual foils.

The first comparison is shown in Fig. 3.14a, for a summed reduction of 10%. The full-voltage curve is included as a reference, together with the three possible combinations of a 5%+5% reduction on two different foils. The curves obtained with a 10% reduction on G1Top and G3Top are also shown. The corresponding G2Top curve is not included in the figure, since the comparison between the three individual foils presented in Section 3.4.3 showed that the G1Top and G2Top curves exhibit very similar behaviour over the investigated range.

The three curves obtained with a 5%+5% reduction are very close to each other over the measured range. They are also close to the curve obtained with a 10% reduction on G3Top, which, as observed in Section 3.4.3, gives the lowest efficiency among the three foils for the same voltage reduction. The G1Top −10% curve lies slightly above the other curves, corresponding to a somewhat higher efficiency, although the difference remains small and compatible with the experimental uncertainties over most of the measured range. Overall, the different configurations provide very similar efficiency curves, indicating that no significant difference can be observed between applying the 10% reduction to a single foil and distributing it as two 5% reductions over two foils.



(a) Comparison for a summed percentage reduction of 10%.



(b) Comparison for a summed percentage reduction of 30%. The double-reduction curves shown correspond to the 10%+20% configurations.

FIGURE 3.14: Comparison of efficiency curves obtained with different distributions of the same summed percentage voltage reduction. In both panels, the full-voltage curve is shown as a reference. The single-foil reductions on G1Top and G3Top and three representative double-foil configurations are also shown.

A similar comparison was performed for a summed reduction of 30%, as shown in Fig. 3.14b. In this case, the single-foil configurations with a 30% reduction on G1Top and G3Top are shown together with the three double-foil configurations obtained by applying a 10%+20% reduction to the three possible pairs of foils. The G2Top −30% curve is again omitted because of its close similarity to the G1Top curve observed in the previous foil comparison. For the same reason, the three double-foil curves are sufficient to represent the behaviour of the different foil combinations in the figure. The remaining double-reduction configurations corresponding to the same summed reduction, namely 15%+15% and 20%+10%, were also measured and showed the same overall behaviour, but are not included in the plot to avoid excessive overlap and loss of readability.
As in the 10% comparison, the three double-reduction curves are very close to each other. They are contained within the region between the G1Top −30% and G3Top −30% curves, which represent the higher- and lower-efficiency behaviours, respectively, observed for the individual foils. Despite the different distributions of the reduction between the two foils, no significant separation between the double-reduction configurations is observed.
These comparisons therefore show that, within the precision of the present measurements, efficiency curves obtained by distributing a given summed percentage reduction over two GEM foils are compatible with those obtained by applying the same percentage reduction to a single foil. This behaviour is observed both for the smallest and the largest summed reductions considered here. The result suggests that, over the range investigated, the efficiency is affected mainly by the overall magnitude of the applied voltage reductions, while no clear additional effect associated with their distribution among two foils can be identified. This conclusion should nevertheless be understood within the limited set of reduction values considered in this comparison and does not imply that the individual foils have identical responses, as demonstrated by the different sensitivities observed in the foil comparison.

3.7 HV compensation

As discussed in Sections 1.4.2, 3.4, and 3.5, a short circuit across a GEM foil modifies the voltage configuration of the detector in two ways. The voltage effectively applied across the affected foil is reduced, while the voltage across the gas gap immediately

below is increased. The former effect is quantified by Eq. (3.9), while the latter is given by Eq. (3.20).

HV compensation is a procedure used for GEM chambers affected by a short circuit to partially or fully restore the nominal operating conditions. It consists of adjusting the voltages supplied by the HV system to counteract the effects of the short circuit. In particular, the top channel voltage can be increased to compensate for the drop across the affected foil, while the bottom channel voltage can be adjusted to correct for the corresponding increase across the gas gap.

Starting from the top channel, if one or more short circuits are present, the voltage provided by the power supply to the top channel, $V_{\text{top}}^{\text{PS,no comp}}$, remains unchanged. Here, *no comp* denotes the configuration before the compensation is applied. What changes is the voltage physically present across the GEM foil affected by the short circuit, $V_{\text{top}}^{\text{foil}}$. During a short circuit, the current flowing through the short-circuit path, I_{short}, can be obtained from the current monitored by the power supply, I_{mon}, such that

$$I_{\text{short}} = I_{\text{mon}}. \tag{3.21}$$

The total resistance crossed by the short-circuit current, R_{short}, can therefore be obtained as

$$R_{\text{short}} = \frac{V_{\text{top}}^{\text{PS,no comp}}}{I_{\text{mon}}}. \tag{3.22}$$

The voltage across the short-affected foil can be obtained as the difference between the voltage provided by the power supply and the voltage drop due to the current flowing through the filter resistors connected to the top and bottom electrodes of the foil (Fig. 1.12b):

$$V_{\text{top}}^{\text{foil}} = V_{\text{top}}^{\text{PS,no comp}} - I_{\text{short}} \left(R_f^{\text{top}} + R_f^{\text{bot}} \right). \tag{3.23}$$

Substituting I_{short} from Eq. (3.22), we obtain

$$\begin{aligned} V_{\text{top}}^{\text{foil}} &= V_{\text{top}}^{\text{PS,no comp}} - V_{\text{top}}^{\text{PS,no comp}} \, \frac{R_f^{\text{top}} + R_f^{\text{bot}}}{R_{\text{short}}} \\ &= V_{\text{top}}^{\text{PS,no comp}} \left(1 - \frac{R_f^{\text{top}} + R_f^{\text{bot}}}{R_{\text{short}}} \right). \end{aligned} \tag{3.24}$$

If the voltage across the affected foil is restored to the nominal value, the compensation condition is

$$V_{\text{top}}^{\text{foil}} = V_{\text{top}}^{\text{nominal}} = V_{\text{top}}^{\text{PS,no comp}}. \tag{3.25}$$

When the compensation is applied, the voltage set at the power supply is instead $V_{\text{top}}^{\text{PS,comp}}$. Therefore, substituting this value into Eq. (3.24), the compensation condition becomes

$$V_{\text{top}}^{\text{PS,no comp}} = V_{\text{top}}^{\text{PS,comp}} \left(1 - \frac{R_f^{\text{top}} + R_f^{\text{bot}}}{R_{\text{short}}}\right). \tag{3.26}$$

The voltage value that the power supply has to provide to the top channel in order to compensate for the voltage drop across the affected foil is therefore

$$V_{\text{top}}^{\text{PS,comp}} = V_{\text{top}}^{\text{PS,no comp}} \frac{R_{\text{short}}}{R_{\text{short}} - \left(R_f^{\text{top}} + R_f^{\text{bot}}\right)}. \tag{3.27}$$

An analogous correction can be applied to the bottom channel in order to restore the nominal voltage across the gas gap below the affected foil. From Eq. (3.18), the increase in the gas-gap voltage induced by the short circuit is given by

$$\Delta V_{\text{bot}} = I_{\text{short}}\, R_f^{\text{bot}}, \tag{3.28}$$

where R_f^{bot} is the resistance of the HV filter connected to the bottom electrode of the affected foil and $I_{\text{short}} = I_{\text{mon}}$ is the current seen by the power supply on the top channel. Its value depends on whether the top channel has already been compensated.

If the compensation of the corresponding top channel has already been applied, the short-circuit current is determined by the compensated voltage set by the power supply:

$$I_{\text{short}}^{\text{comp}} = I_{\text{mon}}^{\text{comp}} = \frac{V_{\text{top}}^{\text{PS,comp}}}{R_{\text{short}}}. \tag{3.29}$$

The voltage applied to the bottom channel is then reduced by the same amount by which the gas-gap voltage is increased:

$$V_{\text{bot}}^{\text{PS,comp}} = V_{\text{bot}}^{\text{PS,no comp}} - \left(\frac{V_{\text{top}}^{\text{PS,comp}}}{R_{\text{short}}}\, R_f^{\text{bot}}\right). \tag{3.30}$$

The bottom channel can also be compensated independently, without applying

the compensation to the top channel. In this case, the short-circuit current is the current $I_{\text{short}}^{\text{no comp}} = I_{\text{mon}}^{\text{no comp}}$ monitored on the top channel before any compensation is applied, so that

$$V_{\text{bot}}^{\text{PS,comp}} = V_{\text{bot}}^{\text{PS,no comp}} - \left(I_{\text{mon}}^{\text{no comp}}\, R_f^{\text{bot}}\right). \tag{3.31}$$

Since $V_{\text{top}}^{\text{PS,comp}} > V_{\text{top}}^{\text{PS,no comp}}$, the current in the first case is larger, and so is the correction applied to the bottom channel [55].

The different form of Eqs. (3.27) and (3.30) may appear as an asymmetry between the two channels: the bottom voltage is lowered by the amount by which the gas-gap voltage increases, whereas the top voltage is not simply raised by the amount by which the foil voltage drops. The reason is that the two shifts depend on different quantities. The increase ΔV_{bot} of Eq. (3.28) is determined by I_{short}, which is set by the voltage supplied to the top channel and does not depend on the voltage supplied to the bottom one. Lowering the bottom power-supply voltage therefore leaves the increase unchanged, and the two contributions cancel exactly. Conversely, the voltage drop in Eq. (3.23) is proportional to I_{short}, which, assuming a constant R_{short}, is itself proportional to the voltage supplied to the top channel, as follows from Eqs. (3.21) and (3.22). Raising $V_{\text{top}}^{\text{PS}}$ increases the short-circuit current and, with it, the drop across the filter resistors, so that adding back the drop measured before the correction would not restore the nominal voltage across the foil. The compensated voltage must instead be determined self-consistently, as done in Eq. (3.27). For the same reason, when both channels are compensated the top channel must be corrected first: its compensated voltage fixes I_{short}, which is then used to correct the bottom channel. Note that this refers to the order of the calculation only, and not to the order in which the voltages are applied at the power supply.

The measurements presented in this chapter can be interpreted in terms of the different compensation configurations. In particular, the laboratory conditions investigated in Sections 3.4 and 3.5 reproduce the individual voltage effects that HV compensation is intended to correct. The correspondence can be summarized as follows:

- full compensation corresponds to the nominal configuration, with no voltage reduction across the GEM foils;

- bottom-only compensation, in which the voltage across the gas gap is restored while the voltage reduction across the affected foil remains, corresponds to the configuration with a reduction of the top voltage only;
- no compensation corresponds to the simultaneous presence of the voltage reduction across the affected foil and the increase of the voltage across the following gas gap.

Therefore, the measurements performed in this work do not constitute a direct study of the compensation procedure itself. Rather, they provide an experimental characterization of the individual effects that have to be compensated in the presence of a short circuit. In this sense, the results obtained in the previous sections provide the basis for assessing the impact of the different voltage configurations on the detector efficiency and for interpreting the corresponding compensation strategies.

3.8 From the laboratory study to GE1/1 operation

The different high-voltage configurations investigated in this laboratory study can be related to those adopted during the operation of GE1/1 chambers at P5, the CMS experimental site at the LHC. The available P5 measurements can be divided into two categories, depending on whether the chambers were operating under nominal conditions or were affected by short circuits.
For healthy GE1/1 chambers, the measurements performed at P5 follow the same approach as the laboratory measurements, namely the characterization of detector efficiency as a function of the voltage applied to the GEM foils. However, the measurements performed on healthy chambers cover only voltage reductions applied to individual GEM foils, as investigated in Section 3.4. The effects of increasing the voltage across the gas gap, discussed in Section 3.5, and of applying simultaneous voltage reductions to multiple GEM foils, described in Section 3.6, were investigated in the laboratory study but were not measured on healthy GE1/1 chambers.
For GE1/1 chambers affected by short circuits, several high-voltage configurations were tested at P5, both with and without compensation. Table 3.4 summarises the correspondence between these configurations and those reproduced in the laboratory with the 10×10 detector.

TABLE 3.4: Correspondence between the high-voltage configurations used at P5 for GE1/1 chambers affected by short circuits and the configurations investigated in the laboratory study.

P5 configuration	**Laboratory counterpart**
Top not compensated, bottom not compensated	Top voltage reduction and bottom gas-gap voltage increase (Section 3.5)
Top not compensated, bottom compensated	Top voltage reduction only (Section 3.4)
Top compensated, bottom compensated	Nominal-voltage reference (Section 2.5.3)
Top compensated, bottom not compensated	Not investigated in the present study

The last configuration listed in Table 3.4 was not investigated in the present study. As discussed in Section 3.5, increasing the voltage across a gas gap while simultaneously restoring the affected GEM foil to its nominal voltage would introduce an over-voltage condition with respect to the nominal operating point. This configuration was therefore not considered appropriate for the laboratory measurements.

The possibility of applying HV compensation to GE1/1 chambers has been investigated during Run 3 operation. Tests of the compensation procedure with both top and bottom channels compensated started in 2025 on six GE1/1 chambers affected by short circuits. In 2026, the procedure was implemented on 34 out of 39 chambers with short circuits, corresponding to approximately 87% of the affected chambers [56]. This demonstrates that HV compensation is not only a possible electrical correction, but has also become an operational strategy for maintaining the performance of chambers affected by short circuits.

The results obtained in the present laboratory study therefore provide a controlled characterization of the individual effects that are relevant to this operational procedure. In particular, the measurements of the efficiency as a function of the voltage applied to the GEM foils and to the gas gaps provide a reference for interpreting the effect of the different voltage configurations adopted in GE1/1 operation.

A direct comparison with data collected at P5 would constitute a natural extension of the present study. The available P5 data include measurements performed with

healthy chambers as well as with chambers affected by short circuits, both with and without HV compensation. Such a comparison would allow the efficiency variations observed in the controlled laboratory measurements to be confronted with the behaviour of full-size GE1/1 chambers under experimental operating conditions. In particular, it would be possible to investigate whether the trends observed for the individual voltage modifications in the laboratory are reproduced when the same configurations are applied to operating GE1/1 chambers.

Conclusions and outlook

The occurrence of permanent short circuits represents an important operational challenge for the GEM detectors installed in the muon system of the CMS experiment. By modifying the effective voltage distribution across the detector, these defects can affect its performance and compromise its detection efficiency. This thesis investigated the effects of short circuits through a systematic experimental study performed with a small-scale triple-GEM detector operated under controlled laboratory conditions.

The experimental apparatus was developed and characterized to reproduce the main operating conditions of the CMS GE1/1 chambers, including the gas mixture, gap dimensions and nominal electric fields. After measuring the detector response under nominal conditions, the electrical consequences of short circuits were reproduced through controlled modifications of the applied high voltages, without introducing permanent defects in the GEM foils. Detection efficiency was chosen as the main observable to quantify the resulting performance degradation. Different configurations were investigated, including voltage reductions across individual GEM foils, modifications of the electric fields in the gas gaps and simultaneous voltage reductions across multiple foils.

One of the main results of this study is the dependence of the efficiency degradation on the position of the affected GEM foil. For comparable voltage reductions, the three foils exhibit different effects on the detector response, with the largest efficiency loss observed when the voltage across the third GEM foil (GEM3) is reduced. This result indicates that the impact of a short circuit cannot be characterized solely by the fraction of the voltage dropped, but must also account for the position of the damaged foil within the amplification structure. The measurements involving simultaneous voltage reductions across multiple foils further extend this characterization to more complex fault configurations.

Another significant result concerns the redistribution of the electric fields following a short circuit. In addition to reducing the voltage across the affected foil, the presence of a short circuit increases the voltage across the subsequent gas gap.

The measurements show that this additional voltage variation can contribute to a further reduction in detection efficiency, emphasizing the importance of reproducing the complete electrical consequences of a short circuit rather than considering the voltage drop across the GEM foil alone. This observation is particularly relevant to the interpretation of the high-voltage compensation procedure currently adopted for the GE1/1 chambers, which accounts for both effects.

I shared part of the work presented in this thesis with the CMS GEM community during its development through two presentations at CMS GEM detector production meetings. I also presented the study in the form of a poster at the 2026 edition of *Incontri di Fisica delle Alte Energie* (IFAE), an Italian conference on high energy physics, held in Bologna.

A natural continuation of this work is the analysis of the operational data collected by the GE1/1 chambers during the LHC Run 3 and their comparison with the laboratory measurements presented here. In particular, the efficiency of chambers operating under nominal conditions and of chambers affected by short circuits could be compared with the corresponding configurations reproduced in the laboratory. Such a comparison would allow the consistency between the response of the small-scale GEM detector and that of the full-size GE1/1 chambers to be assessed, while also providing an opportunity to investigate the effectiveness of the high-voltage compensation currently applied in CMS.

An important objective of these future studies would be to establish a reliable hierarchy of the GEM foils according to the impact of short circuits on detector performance. The laboratory results already indicate a greater sensitivity to voltage reductions affecting GEM3, but validation using operational data would be essential before translating this observation into maintenance priorities. Such a hierarchy could help prioritize repair interventions on damaged GEM foils during the upcoming GE1/1 refurbishment campaign, given the limited time available and the constraints on repair feasibility.

Looking further ahead, the extension of this type of investigation to the GEM detectors of the new ME0 station, which will complement the CMS muon system for the High-Luminosity LHC, would be particularly valuable. Studying the effects of short circuits under the specific operating conditions of these detectors could help establish a more comprehensive understanding of the reliability of GEM technology across the different CMS stations. Ultimately, this research direction could contribute to maintaining the performance and long-term reliability of the

CMS GEM system under the increasingly demanding operating conditions expected during the HL-LHC era.

Appendix A

Alternative representations of the efficiency curves

This appendix presents alternative representations of the efficiency measurements discussed in Section 3.4.3. The same experimental data are used, but different quantities are chosen for the horizontal axis to provide complementary views of the detector response to voltage reductions. In particular, the efficiency curves are first represented as a function of the nominal equivalent current and then as a function of the sum of the voltages applied to the three top channels. These representations do not introduce new measurements, but offer alternative ways of examining the trends already discussed in the main text.

A.1 Efficiency as a function of equivalent current

In Section 3.4.3, the efficiency curves were compared as a function of the sum of the voltages applied to the seven HV channels. With this representation, reducing the voltage of one of the top channels produces a horizontal shift towards lower values of the summed voltage. At the same time, the efficiency decreases as the voltage reduction increases. Consequently, the horizontal displacement and the vertical decrease in efficiency appear simultaneously, making it less straightforward to distinguish their respective contributions to the observed differences between curves.

To provide a complementary view of the results, the efficiency curves can instead be plotted as a function of the equivalent current associated with the nominal operating configuration. In this representation, each measurement point is assigned the equivalent-current value corresponding to the nominal configuration, independently of whether a voltage reduction was applied to one of the top channels. This choice

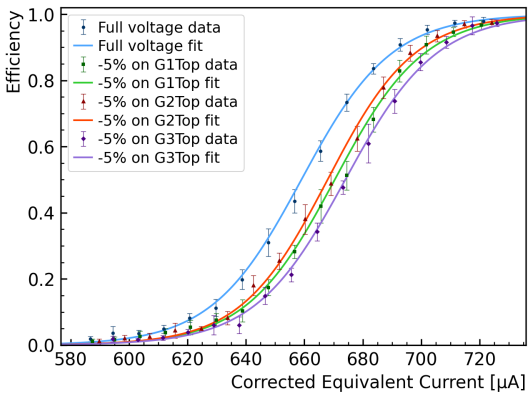
is deliberate: the equivalent current is not recalculated from the actual voltages applied during the reduced-voltage measurements. Rather, the nominal value is retained to reduce the horizontal displacement associated with the voltage reduction and thereby highlight the corresponding changes in efficiency.
The pressure and temperature correction described by Eq. (3.5) is then applied to the nominal equivalent-current values, according to

$$I_{\mathrm{eq}}^{\mathrm{corr}} = I_{\mathrm{eq}}^{\mathrm{nom}} \left[\left(\frac{P_0}{P} \right) \left(\frac{T}{T_0} \right) \right]^{0.43}, \tag{A.1}$$

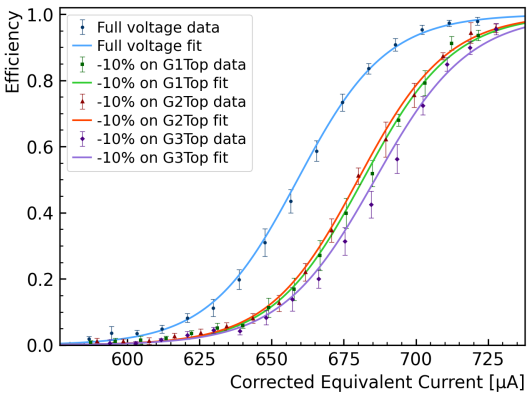
where $I_{\mathrm{eq}}^{\mathrm{nom}}$ is the equivalent current associated with the nominal voltage configuration, before any reduction is applied. For each measurement point, the correction is calculated using the mean pressure and temperature recorded during the corresponding acquisition. The resulting corrected value is then used as the horizontal coordinate of the point.
The results are shown in Fig. A.1.
The resulting curves exhibit trends consistent with those observed in Section 3.4.3. As the applied voltage reduction increases, the efficiency decreases, regardless of which top channel is affected. The curves obtained by reducing G1Top and G2Top remain close to each other and show similar behaviour throughout the investigated range. In contrast, the G3Top curve lies below the other two, with the difference becoming more pronounced at larger voltage reductions.
Thus, representing the efficiency as a function of the nominal equivalent current provides a complementary view of the same measurements while preserving the main conclusions drawn from the voltage-based comparison. In particular, the distinct response observed when reducing G3Top remains evident in this representation.

A.2 Efficiency as a function of top-channel voltage sum

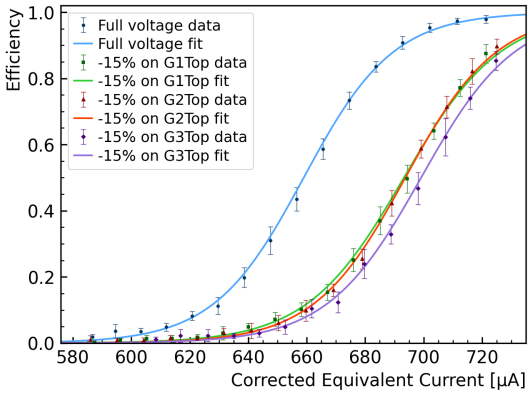
A second alternative representation is obtained by plotting the efficiency curves as a function of the sum of the voltages applied to the three top channels, G1Top, G2Top, and G3Top, rather than the sum of all seven HV channels.
As discussed in Section 3.3, the top channels contribute to establishing the potential differences across the GEM foils, which generate the electric fields responsible for charge multiplication. Therefore, considering only the voltages applied to these



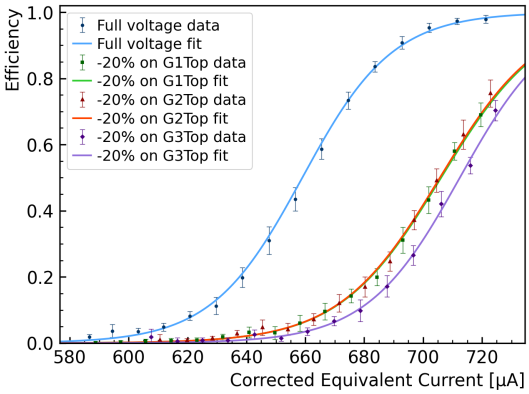
(a) 5% voltage reduction.



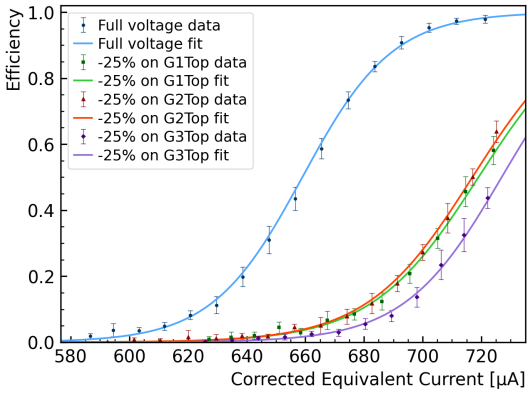
(b) 10% voltage reduction.



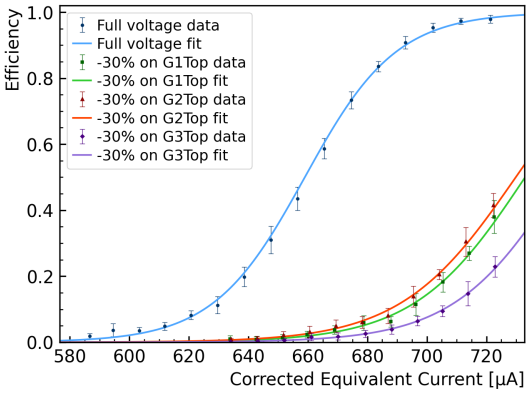
(c) 15% voltage reduction.



(d) 20% voltage reduction.



(e) 25% voltage reduction.



(f) 30% voltage reduction.

FIGURE A.1: Comparison of the efficiency curves as a function of the pressure- and temperature-corrected nominal equivalent current for voltage reductions ranging from 5% to 30%. Each panel corresponds to a fixed reduction and shows the reference curve at nominal voltage together with the curves obtained by applying the same reduction to G1Top, G2Top, and G3Top. The nominal equivalent-current values are retained for the reduced-voltage configurations.

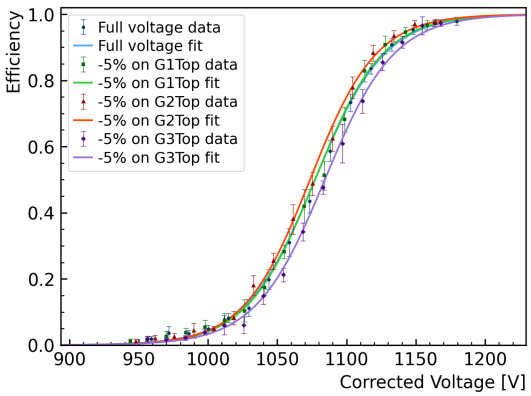
channels provides a representation more directly related to the detector amplification process.

Figure A.2 shows the efficiency curves obtained with this choice of horizontal axis, for the same voltage reductions considered in the previous comparisons.

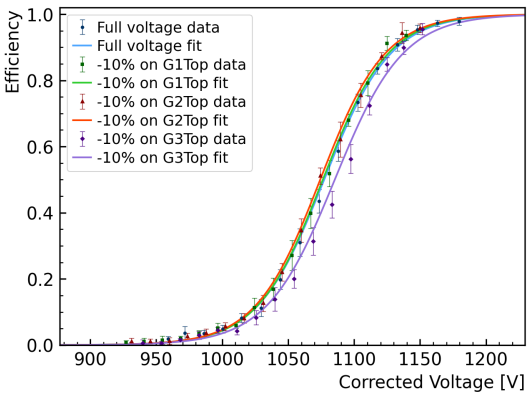
The resulting curves confirm the general trends observed in the previous representations. The efficiency curves corresponding to voltage reductions applied to G1Top and G2Top exhibit very similar behaviour and are almost completely overlapping throughout the investigated range. The G3Top curve consistently shows the lowest efficiency, with its separation from the other two curves becoming more pronounced as the voltage reduction increases.

However, a difference emerges when comparing this representation with those presented previously. The curves corresponding to reductions applied to G1Top and G2Top remain nearly superimposed on the reference curve, even at the largest voltage reductions. Although the G3Top curve still exhibits a visible deviation, it also appears considerably closer to the reference curve, including at the 30% reduction.

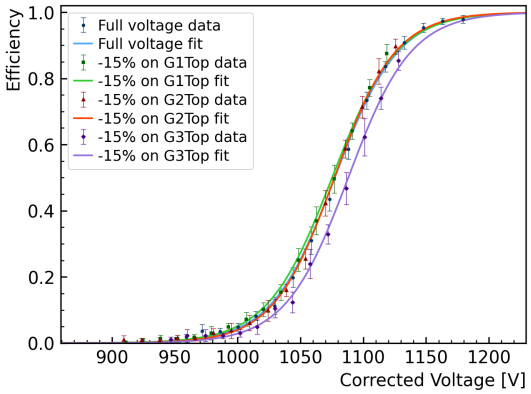
It is important to note that these differences arise from the choice of the quantity represented on the horizontal axis, rather than from changes in the measured efficiencies. Indeed, the efficiency values are identical to those presented in the previous comparisons. The apparent proximity of the curves should therefore be interpreted in the context of this alternative voltage representation and does not indicate a smaller loss of efficiency caused by the applied voltage reductions.



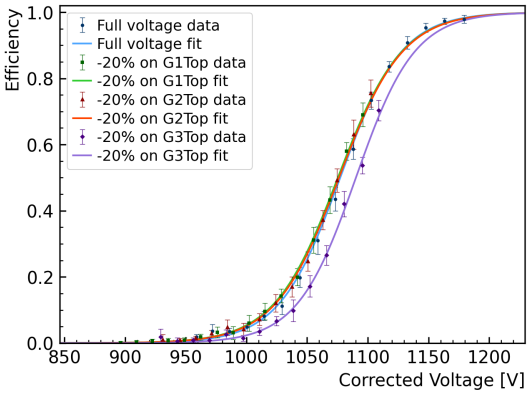
(a) 5% voltage reduction.



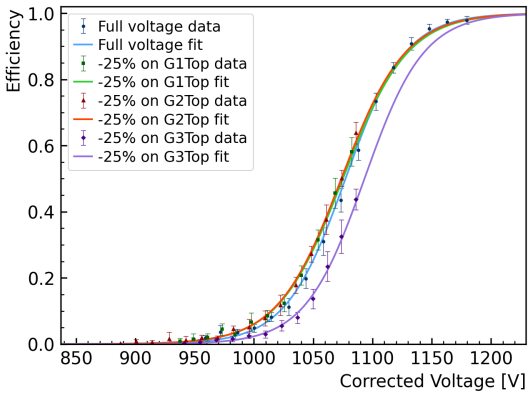
(b) 10% voltage reduction.



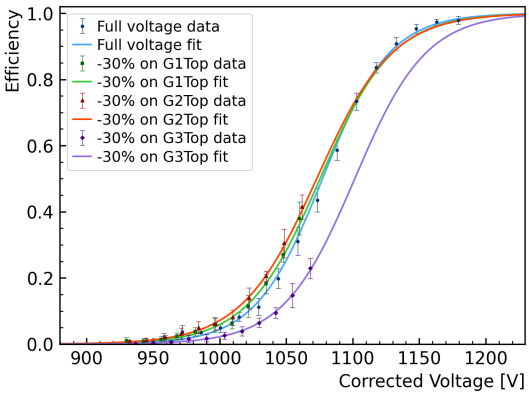
(c) 15% voltage reduction.



(d) 20% voltage reduction.



(e) 25% voltage reduction.



(f) 30% voltage reduction.

FIGURE A.2: Comparison of the efficiency curves as a function of the sum of the voltages applied to G1Top, G2Top, and G3Top, for voltage reductions ranging from 5% to 30%. Each panel corresponds to a fixed reduction and shows the reference curve at nominal voltage together with the curves obtained by applying the same reduction to G1Top, G2Top, and G3Top. The voltage values are corrected for pressure and temperature variations according to Eq. (3.6).

Bibliography

[1] CERN. *CERN – The European Laboratory for Particle Physics*. 2026. URL: https://home.cern/ (visited on 07/01/2026).

[2] Gargamelle Collaboration. "Observation of neutrino-like interactions without muon or electron in the Gargamelle neutrino experiment". In: *Physics Letters B* 46.1 (1973), pp. 138–140. DOI: 10.1016/0370-2693(73)90499-1.

[3] Gargamelle Collaboration. "Search for elastic muon-neutrino electron scattering". In: *Physics Letters B* 46.1 (1973), pp. 121–124. DOI: 10.1016/0370-2693(73)90494-2.

[4] G. Arnison et al. "Experimental Observation of Isolated Large Transverse Energy Electrons with Associated Missing Energy at $\sqrt{s} = 540$ GeV". In: *Physics Letters B* 122.1 (1983), pp. 103–116. DOI: 10.1016/0370-2693(83)91177-2.

[5] M. Banner et al. "Observation of Single Isolated Electrons of High Transverse Momentum in Events with Missing Transverse Energy at the CERN $p\bar{p}$ Collider". In: *Physics Letters B* 122.5–6 (1983), pp. 476–485. DOI: 10.1016/0370-2693(83)91605-2.

[6] G. Arnison et al. "Experimental Observation of Lepton Pairs of Invariant Mass Around 95 GeV/c^2 at the CERN SPS Collider". In: *Physics Letters B* 126.5 (1983), pp. 398–410. DOI: 10.1016/0370-2693(83)90188-0.

[7] P. Bagnaia et al. "Evidence for $Z^0 \to e^+e^-$ at the CERN $p\bar{p}$ Collider". In: *Physics Letters B* 129.1–2 (1983), pp. 130–140. DOI: 10.1016/0370-2693(83)90744-X.

[8] ATLAS Collaboration. "Observation of a New Particle in the Search for the Standard Model Higgs Boson with the ATLAS Detector at the LHC". In: *Physics Letters B* 716.1 (2012), pp. 1–29. DOI: 10.1016/j.physletb.2012.08.020.

[9] CMS Collaboration. "Observation of a New Boson at a Mass of 125 GeV with the CMS Experiment at the LHC". In: *Physics Letters B* 716.1 (2012), pp. 30–61. DOI: 10.1016/j.physletb.2012.08.021.

[10] O. S. Brüning and L. Rossi, eds. *The High Luminosity Large Hadron Collider*. Vol. 24. Advanced Series on Directions in High Energy Physics. World Scientific, 2015. DOI: 10.1142/9581.

[11] CMS Collaboration. *It Takes a Village — projecting future studies at the High-Luminosity LHC*. 2019. URL: https://cms.cern/news/it-takes-village-future-studies-high-luminosity-lhc (visited on 07/01/2026).

[12] CERN. *LHC delivers record number of particle collisions in 2025*. Dec. 2025. URL: https://home.cern/lhc-delivers-record-number-particle-collisions-2025/ (visited on 08/08/2026).

[13] CMS Collaboration. *The End of Run 3*. 2026. URL: https://cms.cern/news/end-run-3 (visited on 07/09/2026).

[14] *High-Luminosity LHC*. CERN. URL: https://home.cern/science/accelerators/hilumi-lhc/ (visited on 07/09/2026).

[15] O. Brüning and M. Zerlauth. *LHC Operation and the High-Luminosity LHC Upgrade Project*. Contribution to the CAS – CERN Accelerator School: Advanced Accelerator Physics, 10–22 November 2024, Spa, Belgium. 2025. DOI: 10.48550/arXiv.2505.03535.

[16] R. Maria and R. Tomás. "HL-LHC Status and Operational Scenarios". In: 2022, p. 049. DOI: 10.22323/1.414.0049.

[17] CMS Collaboration. *The Phase-2 Upgrade of the CMS Muon Detectors*. Vol. 2017-012. CERN-LHCC. Geneva: CERN, 2017. DOI: 10.17181/CERN.5T9S.VPMI.

[18] CMS Collaboration. *The CMS Detector*. 2026. URL: https://cms.cern/detector (visited on 07/02/2026).

[19] D. Haitz. "Precision Studies of Proton Structure and Jet Energy Scale with the CMS Detector at the LHC". Report number: IEKP-KA/2016-04. Doctoral Thesis. Karlsruhe Institute of Technology (KIT), 2016.

[20] CMS Collaboration, ed. *CMS Physics: Technical Design Report, Volume I: Detector Performance and Software*. Vol. 2006-001. CERN-LHCC. Geneva: CERN, 2006.

[21] CMS Collaboration. "The CMS experiment at the CERN LHC". In: *Journal of Instrumentation* 3 (2008), S08004. DOI: 10.1088/1748-0221/3/08/S08004.

[22] CMS Collaboration. *The CMS Muon Project: Technical Design Report*. Vol. 97-32. CERN-LHCC. Geneva: CERN, 1997.

[23] CMS Collaboration. "Performance of the CMS muon detector and muon reconstruction with proton-proton collisions at $\sqrt{s} = 13$ TeV". In: *Journal of Instrumentation* 13 (2018), P06015. DOI: 10.1088/1748-0221/13/06/P06015.

[24] CMS Collaboration. *CMS Technical Design Report for the Muon Endcap GEM Upgrade*. Technical Design Report CERN-LHCC-2015-012, CMS-TDR-013. Geneva: CERN, 2015.

[25] G. Charpak et al. "The Use of Multiwire Proportional Counters to Select and Localize Charged Particles". In: *Nuclear Instruments and Methods* 62.3 (1968), pp. 262–268. DOI: 10.1016/0029-554X(68)90371-6.

[26] A. Oed. "Position-sensitive detector with microstrip anode for electron multiplication with gases". In: *Nuclear Instruments and Methods in Physics Research Section A* 263.2–3 (1988), pp. 351–359. DOI: 10.1016/0168-9002(88)90970-9.

[27] F. Sauli and A. Sharma. "Micropattern Gaseous Detectors". In: *Annual Review of Nuclear and Particle Science* 49 (1999), pp. 341–388. DOI: 10.1146/annurev.nucl.49.1.341.

[28] F. Sauli. "The Gas Electron Multiplier (GEM): Operating Principles and Applications". In: *Nuclear Instruments and Methods in Physics Research Section A* 805 (2016), pp. 2–24. DOI: 10.1016/j.nima.2015.07.060.

[29] G. Barr et al. *Particle Physics in the LHC Era*. Oxford University Press, Jan. 2016. DOI: 10.1093/acprof:oso/9780198748557.001.0001.

[30] S. Bachmann et al. "Development and applications of the gas electron multiplier". In: *Nuclear Instruments and Methods in Physics Research Section A: Accelerators, Spectrometers, Detectors and Associated Equipment* 471.1 (2001). Imaging 2000, pp. 115–119. DOI: https://doi.org/10.1016/S0168-9002(01)00968-8.

[31] A. Velasquez and H. Castro. "Radiation dosimetry with a Triple-GEM detector". In: *MOMENTO* 66 (2023), pp. 70–89. DOI: 10.15446/mo.n66.104505.

[32] F. Sauli. "GEM: A new concept for electron amplification in gas detectors". In: *Nuclear Instruments and Methods in Physics Research Section A* 386.2–3 (1997), pp. 531–534. DOI: 10.1016/S0168-9002(96)01172-2.

[33] S. Bachmann et al. "Charge amplification and transfer processes in the gas electron multiplier". In: *Nuclear Instruments and Methods in Physics Research Section A* 438.2 (1999), pp. 376–408. DOI: 10.1016/S0168-9002(99)00820-7.

[34] V. Tikhonov and R. Veenhof. "GEM simulation methods development". In: *Nuclear Instruments and Methods in Physics Research Section A* 478.1 (2002). Proceedings of the Ninth International Conference on Instrumentation for Colliding Beam Physics, pp. 452–459. DOI: 10.1016/S0168-9002(01)01801-0.

[35] P. S. Barbeau et al. "Electron transparency, ion transparency and ion feedback of a 3M GEM". In: *Nuclear Instruments and Methods in Physics Research Section A* 525.1 (2004). Proceedings of the International Conference on Imaging Techniques in Subatomic Physics, Astrophysics, Medicine, Biology and Industry, pp. 33–37. DOI: 10.1016/j.nima.2004.03.053.

[36] A. Bressan et al. "High gain operation of GEM in pure argon". In: *Nuclear Instruments and Methods in Physics Research Section A* 423.1 (1999), pp. 119–124. DOI: 10.1016/S0168-9002(98)01197-8.

[37] A. Buzulutskov et al. "The GEM photomultiplier operated with noble gas mixtures". In: *Nuclear Instruments and Methods in Physics Research Section A* 443.1 (2000), pp. 164–180. DOI: 10.1016/S0168-9002(99)01011-6.

[38] B. Ketzer et al. "Performance of triple GEM tracking detectors in the COMPASS experiment". In: *Nuclear Instruments and Methods in Physics Research Section A* 535.1 (2004). Proceedings of the 10th International Vienna Conference on Instrumentation, pp. 314–318. DOI: 10.1016/j.nima.2004.07.146.

[39] M. Alfonsi et al. "High-rate particle triggering with triple-GEM detector". In: *Nuclear Instruments and Methods in Physics Research Section A* 518.1 (2004). Proceedings of the Frontier Detectors for Frontier Physics Conference, pp. 106–112. DOI: 10.1016/j.nima.2003.10.035.

[40] H. Raether. *Electron Avalanches and Breakdown in Gases*. Butterworths, 1964.

[41] CMS Collaboration. "Performance of Prototype GE1/1 Chambers for the CMS Muon Spectrometer Upgrade". In: *Nuclear Instruments and Methods in Physics Research Section A* 972 (2020), p. 164104. DOI: 10.1016/j.nima.2020.164104.

[42] CMS Collaboration. "Study on discharge and short circuit generation in CMS GE1/1 triple-GEM detectors during Run 3". In: *Journal of Instrumentation* 20.05 (May 2025), P05035. DOI: 10.1088/1748-0221/20/05/P05035.

[43] M. Abbas et al. "Impact of magnetic field on the stability of the CMS GE1/1 GEM detector operation". In: *Journal of Instrumentation* 18.11 (Nov. 2023), P11029. DOI: 10.1088/1748-0221/18/11/P11029.

[44] CMS Collaboration. *Quality Control of Mass-Produced GEM Detectors for the CMS GE1/1 Muon Upgrade*. CMS Note CMS-NOTE-2022-004. Geneva: CERN, 2022. DOI: 10.1016/j.nima.2022.166716.

[45] S. Calzaferri. *Study of Discharges in CMS GEM Detectors*. CMS Muon Group. Aug. 31–Sept. 4, 2026. URL: https://indico.cern.ch/event/1473492/contributions/7200210/attachments/3333504/5972787/scalzafe_MPGD_2026_V1.pdf (visited on 09/24/2026).

[46] R. N. Patra et al. "Measurement of basic characteristics and gain uniformity of a triple GEM detector". In: *Nuclear Instruments and Methods in Physics Research Section A* 862 (2017), pp. 25–30. DOI: 10.1016/j.nima.2017.05.011.

[47] Bosch Sensortec GmbH. *BME680: Low Power Gas, Pressure, Temperature & Humidity Sensor — Datasheet*. Document number BST-BME680-DS001-09, Rev. 1.9. Bosch Sensortec GmbH. Feb. 2024. URL: https://www.bosch-sensortec.com/media/boschsensortec/downloads/datasheets/bst-bme680-ds001.pdf (visited on 09/16/2026).

[48] Arduino S.r.l. *Arduino® Mega 2560 Rev3: User Manual*. SKU A000067, Rev. 3. Arduino S.r.l. Apr. 25, 2024. URL: https://docs.arduino.cc/resources/datasheets/A000067-datasheet.pdf (visited on 09/16/2026).

[49] F. Fallavollita. "Triple-Gas Electron Multiplier technology for future upgrades of the CMS experiment: construction and certification of the CMS GE1/1 detectors and longevity studies". Doctoral Thesis. Pavia, Italy: Università degli Studi di Pavia, Jan. 2019.

[50] ORTEC (AMETEK). *Experiment 12: X-Ray Fluorescence*. https://mobydick.mib.infn.it/brofferio/didattica/exp-ortec/ORTEC12-Xray.pdf. Educational Experiments Manual, document no. 101711. 2011.

[51] D. Fiorina. "R&D on Triple-GEM detectors for the optimal and safe operation in the CMS experiment". Doctoral Thesis. Pavia, Italy: Università degli Studi di Pavia, Jan. 2022.

[52] Keithley Instruments, Inc. *Model 6485 Picoammeter / Model 6487 Picoammeter/Voltage Source: User's Manual*. Document number 6487-900-01 Rev. C. Keithley Instruments, Inc. Cleveland, Ohio, U.S.A., Mar. 2011.

[53] F. Simon et al. "Development of Tracking Detectors With Industrially Produced GEM Foils". In: *IEEE Transactions on Nuclear Science* 54.6 (Dec. 2007), pp. 2646–2652. DOI: 10.1109/tns.2007.909912.

[54] CMS Collaboration. *GEM DPG Public*. https://twiki.cern.ch/twiki/bin/view/CMSPublic/GEMDPGPublic. (visited on 09/07/2026).

[55] CMS Collaboration. *GEM operations and performance in Run 3*. 2026. URL: https://cds.cern.ch/record/2968114 (visited on 10/08/2026).

[56] S. Calzaferri. *GEM operations: lessons learned from Run-3*. Access restricted to CERN/CMS members. Sept. 2026. URL: https://indico.cern.ch/event/1717519/contributions/7239351/attachments/3344965/5996315/20260916_GEM_RCLessonLearned_V1.pdf (visited on 10/08/2026).